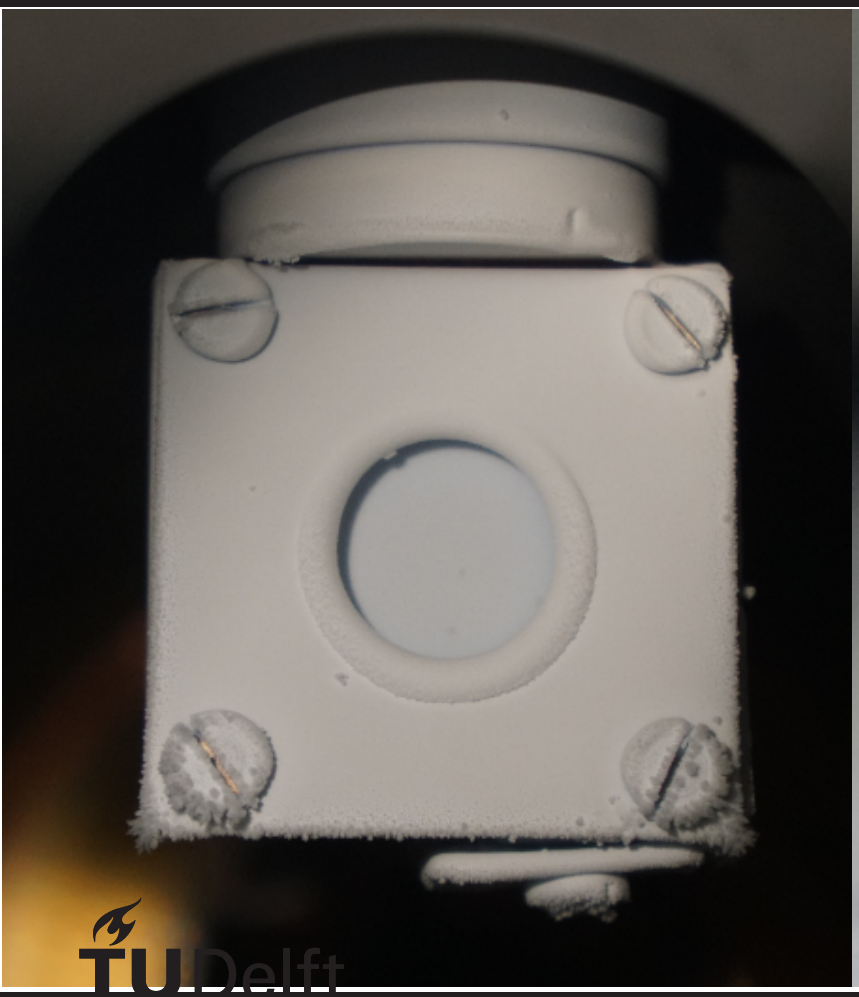
Ultrasonic Propagation in Planetary and Interstellar Ices

An experimental approach

M. P. E. Mendonck

ISBN 000-00-0000-000-0





TU Delft

Ultrasonic Propagation in Planetary and Interstellar Ices

An experimental approach

by

M. P. E. Mendonck

to obtain the degree of Master of Science
at the Delft University of Technology,
to be defended publicly on Thursday April 8, 2021 at 9:00 AM.

Student number:	4294483	
Project duration:	May 18, 2020 – April 8, 2021	
Thesis committee:	Prof. dr. ir. S. Cazaux,	TU Delft, supervisor
	Dr. G. M. Muños Caro,	CAB
	Dr. S. Aparicio Secanellas,	ITEFI

An electronic version of this thesis is available at http://repository.tudelft.nl/.

TU Delft

Acknowledgements

Throughout this thesis, I received a great deal of guidance and support that has helped me deliver this work as a result despite of global pandemic.

Most of all, I want to thank my internship supervisor Sofía and my thesis supervisor Guillermo whose expertise in ultrasound and astrophysics has been paramount to my understanding of the setup and the outcome of the experiments. You also offered help with the language since I didn't master Spanish and advice concerning general things that are of importance when moving abroad. You made me familiar with Madrid, Spain and its culture which is an experience I will never forget. Next I want to thank Stéphanie, the thesis supervisor from the faculty Aerospace Engineering in Delft that has been supporting me from the start of my literature study. I think I got infected by your enthusiasm about this study before I even went to Madrid, which kept me going when Madrid went trough tough times (virus related). Next, I want to acknowledge my colleagues, Margha, José Javier and Cristóbal that contributed to this thesis by creating simulations that are relevant for the experiments I performed (Margha) and experiments that were done when I couldn't physically be at the lab (Cristóbal). You also helped me by making phone calls in my name in Spanish concerning the Vespa I drove. José Javier provided most of the technical expertise concerning ultrasonic measurements and has advised me with how to process the ultrasonic data and explained to me how to see ice signatures by implementing deconvolution in the processing of the data. Furthermore, I want to thank my family for always supporting me from Belgium and occasionally had an E-péritief with me once the confinement started in Madrid. Last but not least I want to thank my girlfriend Stella, for the moral support. Your calls were often the highlight in my days of confinement that made me feel connected to you and optimistic in life.

M. P. E. Mendonck
Delft, April 2021

Abstract

Comets are celestial objects that are thought to have formed at the outer edges of our solar system . The ices they contain is thought to be preserved since their formation in the molecular cloud phase, before the formation of the sun. The formation of ices in the molecular cloud occur via the ice mantle accretion process, by condensation of molecules onto the cold dust surfaces. Because of the very cold temperatures, the water molecules accreting onto dust are expected to form highly porous ice, as it occurs in the laboratory simulations. The icy grains encountering each other will form larger bodies, such as comets, and the porous ices plus the coagulation of icy grains leads to a fluffy cometary ice structure. This study explores the feasibility of porosity measurements by means of ultrasonic measurements in these ices. A new, small liquid N_2 cooled vacuum chamber was used to perform the experiments with different type of ices. Astrophysical ices were grown on a methacrylate substrate on which an ultrasonic transducer was mounted that sent and received ultrasonic signals. Experiments with H_2O (water) and CH_3OH (methanol) were done by deposition from a gas phase while also H_2O (water) and C_2H_5OH (ethanol) were frozen on top of the methacrylate from their liquid phase. These two type of experiments required an adapted version of the setup that allowed for experiments that can freeze ice from its liquid state at atmospheric pressure after which the rest of the experiment could take place in the vacuum chamber. From this experiment, the speed of sound in water ice could be determined as a function of temperature. A linear trend for a decreasing temperature in water ice was found with slope $\frac{dc_{(T)}}{dT} = -2.5494 m/(s°C)$ and an offset at $0°C$ of $c_{(T=0°C)} = 3616.86 m/s$ for a temperature range from $0°C$ to $-100°C$. Results show that propagation of ultrasonic waves in vacuum chamber-grown ice encounters too much attenuation that prevented a distinct signal to be detectable by the transducer.

Contents

1 Introduction 1
1.1 The Interstellar Medium (ISM) . . . 1
1.2 Evolutionary Background of Ices in the solar system . . . 2
1.2.1 Ice growth in Molecular Clouds . . . 3
1.2.2 Ice after collapse of Molecular Cloud . . . 4
1.3 Ices in the solar system . . . 5
1.3.1 Late Heavy Bombardment (LHB) . . . 5
1.3.2 Comets . . . 5
1.3.3 Moons and icy bodies . . . 6
1.3.4 Other places . . . 6
1.4 Ice Characterization . . . 7
1.4.1 Ice Composition . . . 7
1.4.2 Porosity in ice . . . 10
1.5 The ISAC . . . 12
1.5.1 Lay-out . . . 12
1.5.2 Description of ISAC . . . 12
1.5.3 Component description of ISAC . . . 13
1.6 Ultrasound . . . 15
1.6.1 Principle . . . 15
1.6.2 Types of applications . . . 16
1.6.3 Visualization . . . 16
1.7 This Thesis . . . 18

2 Experimental setup 19
2.1 Ice drop experiments . . . 19
2.2 Mobile vacuum chamber . . . 20
2.2.1 Lay-out . . . 20
2.2.2 Description of the mobile vacuum chamber . . . 22
2.2.3 Component description of the mobile vacuum chamber . . . 22

3 Approach 25
3.1 Research & Simulation . . . 25
3.2 Ice Deposition Experiments . . . 26
3.2.1 Experiments without Vacuum . . . 26
3.2.2 Vacuum Experiments . . . 28
3.3 Porous Ice Experiments . . . 28
3.3.1 With Mobile Vacuum Chamber . . . 29
3.3.2 With ISAC . . . 30
3.4 Concluding all results . . . 30

4 Numerical simulations of the experimental conditions and experimental results 31
4.1 Thermal Conductivity Sample Holder with polymethylmethacrylate (PMMA) Substrate . . . 31
4.2 Ultrasonic Propagation . . . 34
4.2.1 In Ice Drop . . . 35
4.2.2 In porous ice drop . . . 37
4.2.3 In "Seta" + aluminium dish + ice . . . 38

5 Ice Drop Experiments and Results 43
5.1 Compact Ice Drops . . . 43
5.2 Porous Ice Drops . . . 46
5.3 Compact vs porous ice drop experiments . . . 50
5.4 Alternative Ice Drops . . . 51
5.4.1 Bubble-free sparkling water . . . 51
5.4.2 Beer . . . 52
5.4.3 Ethanol (96%) . . . 53
5.5 Irregularities . . . 54
5.5.1 Ultrasonic signal during phase transition (Freezing & Melting) . . . 54
5.5.2 Cracks in Ice . . . 56
5.5.3 Feature at $\pm 1\mu s$ ToF in ice drops . . . 57
5.5.4 Room Temperature variations . . . 58

6 Vacuum Chamber Experiments and Results 59
6.1 Vacuum Chamber Experiments . . . 59
6.1.1 Without ice deposition . . . 59
6.1.2 H_2O deposition without refill of the deposition tube . . . 61
6.1.3 H_2O deposition with multiple refills of the deposition tube . . . 64
6.1.4 CH_3OH deposition . . . 66
6.1.5 Deposition type comparison . . . 68
6.2 Improved Vacuum chamber Experiments . . . 69
6.2.1 Aerograph Experiments . . . 69
6.2.2 Improvements to Vacuum Chamber . . . 70
6.2.3 New Obstacles and Fixing Attempts . . . 71
6.2.4 Successful experiments . . . 73

7 Concluding remarks and applications 77
7.1 Concluding remarks . . . 77
7.2 Possible applications derived from this thesis . . . 78
7.3 General applications . . . 78

Bibliography 79

A Complete Roadmap of the Project 83

B Data from drop experiments 85
B.1 Compact Ice drop experiments . . . 86
B.2 Porous Ice drop experiments . . . 87
B.3 Alternative Ice drop experiments . . . 87

C Vacuumchamber experiments 89
C.1 03/07: H_2O Deposition experiment . . . 89
C.2 09/07: H_2O Deposition experiment . . . 90
C.3 15/07: No Deposition experiment . . . 91
C.4 20/07: No Deposition experiment . . . 92
C.5 22/07: H_2O Deposition experiment . . . 93
C.6 24/07: H_2O Deposition experiment . . . 95
C.7 28/07: H_2O Deposition experiment . . . 96
C.8 29/07: CH_3OH Deposition experiment . . . 98
C.9 30/07: CH_3OH Deposition experiment . . . 99

1 Introduction

The aim of this thesis is to develop a means to characterize ices with ultrasound that has the potential to be embedded on future space missions to comets or other celestial objects in the outer solar system. In this introduction, Section 1.1 emphasizes on a brief version of the background information and context about the formation of the solar system in the Interstellar Medium (ISM). Section 1.2 will reveal the importance of studying these ices from that point on in more detail followed by Section 1.3 that contains most known places where ices are found in our solar system. More characteristics about the ices are provided in Section 1.4. Section 1.6 stresses on the principles of ultrasound, the benefits of using ultrasonic measurements and touches on a number of relevant applications as well as visualization with ultrasound. The scope of the remaining thesis chapters will be laid out in Section 1.7.



Figure 1.1: The Eagle Nebula's Pillars of Creation as seen in visible light. This is an iconic molecular cloud in the ISM. Credit NASA, ESA/Hubble

1.1. The Interstellar Medium (ISM)

The formation of interstellar ice finds its origin in the vast emptiness of space between stars in galaxies such as our Milky Way. This space is referred to as the Interstellar Medium in which big and complex shapes comprise gas, dust particles and Cosmic Radiation (CR). About 89% of the composition of the ISM is Hydrogen, while about 9% is comprised by Helium [15].



Figure 1.2: The Horsehead Nebula shown in infrared light which makes it possible for light in the background to be noticed by the camera. Credit NASA, ESA

Only about 2% of the mass of the ISM contains heavier elements that are predominantly O,C and N (4.9, 2.7 and $0.7 \cdot 10^{-4}$ times the abundance of H respectively) [3]. Interstellar Clouds and nebula's, such as the Pillars of Creation (Figure 1.1) or the Horsehead Nebula (Figure 1.2), are the densest objects in the ISM and can range in size from radii of $\sim 5-200pc$ and in mass from $\sim 10^2 - 10^6 M_\odot$ [3]. Mostly, the internal gas pressure and magnetic pressure counteract the gravitational forces which makes molecular clouds stable environments in the ISM. But Interstellar Clouds tend to block a certain amount of radiation towards its center, which can decrease its temperature. Some Interstellar Clouds become so dense that they obscure the visible light and therefore appear dark for observers [2]. The decrease of radiation in these Dark Clouds will cause its core to cool down to $\sim 10K$. The decrease in temperature initiates a decrease in pressure which makes gravity attract and move the particles of the core more inward. This motion can start a collapse of the Molecular Cloud that will lead to the formation of a protostar.

1.2. Evolutionary Background of Ices in the solar system

This section explains how ice grows in vacuum in space. Figure 1.3 is a graphical representation of the different phases during the formation of planetary constellations such as our solar system. When obscured molecular clouds in the ISM collapse, as described in the previous section, heat starts building up in its core. During the collapse, the particles gain kinetic energy. When they approach its center, the increased density increases the pressure which will decelerate particles. This will transfer most of the kinetic energy into heat.

Eventually, the pressure and temperature in the center of the collapsing cloud will be sufficient for nuclear fusion of hydrogen. At this stage, the illuminating core becomes a protostar. The kinetic energy of the inward movement of particles eventually causes the collapsing cloud to rotate [21] [35]. While the protostar is still growing by the inward movement of particles, the rotation of the cloud initiates the formation of a disk, the "Accretion Disk". At some point, the particles will stop falling in the protostar and the accretion disk. Now the star is completely formed and has a rotating disk of dust and gasses around it. Some of the gasses condense and form small grains in the disk. The grains in the disk tend to move vertically towards the midplane because of its gravity. Here grains will come together and start to grow bigger grains, which is called sedimentation [18]. When the grains start to have a length of more than a centimeter, the rate of growth will increase further. When the diameter becomes in the order of a kilometer, planetesimals are created which are necessary for the formation of the planetary embryo's [16].

The last stage in the formation of the solar system is the formation of the planets themselves. For rocky terrestrial planets, this happens by numerous energetic collisions of planetary embryo's in highly elliptic orbits. Most of the kinetic energy in these collisions is converted into thermal energy that increases the temperature of the growing planet. Eventually the temperature of the entire planet can heat up that much that the interior starts to melt [18]. This heat will vaporize any water or volatile gasses that were present and might form an atmosphere. Gas giants start forming similar to the terrestrial planets, but when they are big enough they start accreting a lot of gas. After planets freed up the space in their track, their orbits remain reasonably stable.

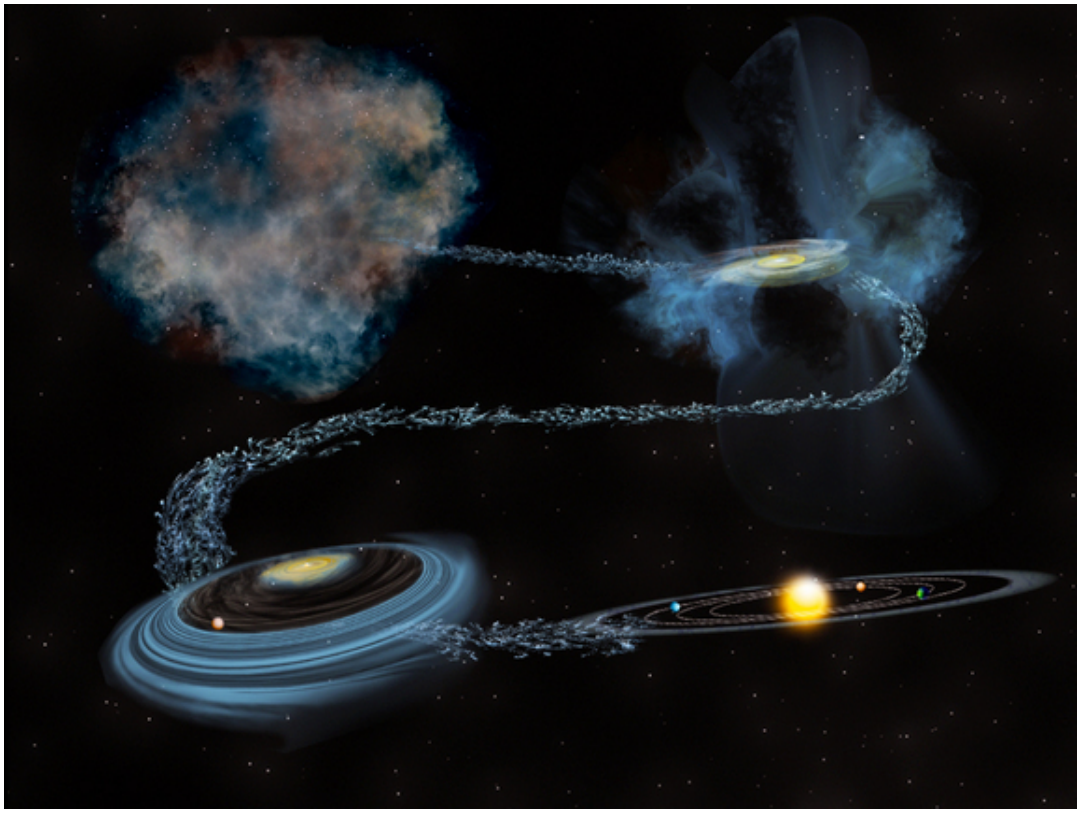


Figure 1.3: The evolution of the solar system. From a molecular dense cloud in the top left to a protostar on the top right and a protoplanetary disk left under. On the bottom right the solar system has completely formed with stable planetary orbits. Credit: NASA

1.2.1. Ice growth in Molecular Clouds

At the end of its lifecycle, a star is not able to sustain nuclear fusion. The star will grow bigger and starts to fuse heavier elements than hydrogen. A low-mass star becomes a red giant and a high-mass star will become a red supergiant. At the end of their lives, they will expel the matter they are made of and enrich the ISM with newly formed elements. The red giants become a nebula and the red supergiants turn into a supernova. This is a highly energetic explosion that increases the brightness of the star significantly. The lifecycle of heavy stars is therefore responsible for the existence of heavier elements than Beryllium in the ISM. The combination of C, O and Si allows for the formation of grains [1], the most important solid particles for chemistry in molecular clouds.

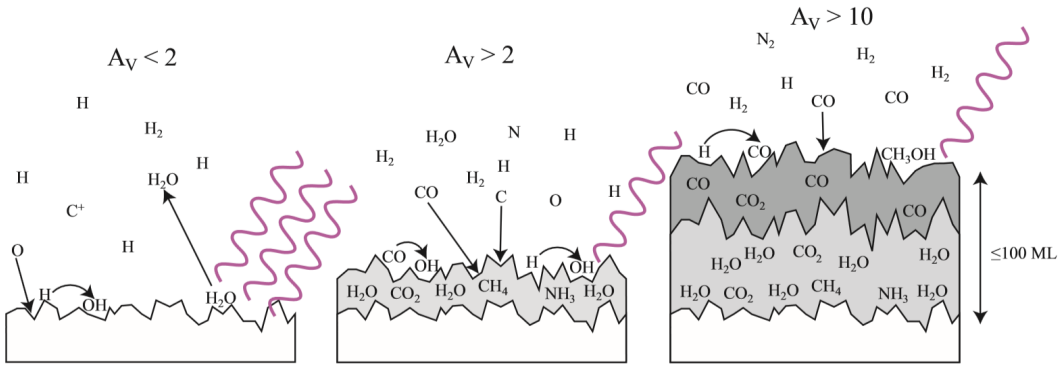


Figure 1.4: Ice formation on dust grains prior to star formation. The condition in an early dense molecular cloud can form H_2O by hydrogenation of oxygen (atomic) on the surface of the grains as shown on the left. The middle figure resembles the grain surface of a dense dark cloud. Here the temperature is sufficiently cold for the H_2O molecules to freeze onto the surface together with other compounds with fewer abundances. The figure on the right entails the fast growth of a CO-rich ice layer on top of the H_2O-rich layer since the temperature is now extremely low ($\sim 10K$). Credit K. Öberg et al (2009)

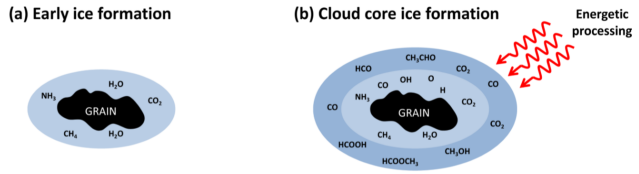


Figure 1.5: During the early cloud formation, H_2O-rich ice forms on the grain (a). When the cloud continues to cool down, CO-rich ice starts to freeze (b). The addition of the CO-rich ice in combination with energetic processes induced by UV-photolysis and cosmic ray (CR) irradiation allows for the formation of more complex species like CH_3OH, H_2CO, $HCOOH$, $HCOOCH_3$, HCO and CH_3CHO [3]. Credit Öberg et al (2010).

As the temperature in interstellar clouds can become very low, atoms and molecules exert a "sticking" force on the surface of the grains [14]. This allows for atoms and molecules to meet and form new molecules. When the radiation levels are still higher than $A_v < 2$, this will cause the newly formed molecules to desorb [36] [12]. But as the molecular cloud will collapse, its optical thickness will increase and consequently the radiation inside the cloud will decrease to levels of $A_v > 2$. This will allow for the formation of ice on the surface of the grains because the molecules will not desorb anymore. At this stage predominantly water molecules will freeze on the solid grains and a minor amount of other molecules. This process is visualized in Figure 1.4. The right most situation in this figure resembles the condition in a further developed collapsing molecular cloud. Because of the absence of radiation ($A_v > 10$) and the extremely low temperatures ($\sim 10K$), CO-ice can be formed on top of the water ice layer [15]. The UV-radiation that can still reach the icy grains, allows for the formation of more complex molecules by energetic processing [4] [29] [3] [31], which is represented by the sketches in Figure 1.5.

1.2.2. Ice after collapse of Molecular Cloud

Starting from its center, a collapsing molecular cloud will encounter an increase in pressure and temperature. When the temperature will reach values of above ~ $20K$, the CO-ice will all sublimate. The remaining ice on the grains continues to have chemical reactions with adjacent molecules which makes the formation of more complex molecules possible [34] [15] [11]. Eventually, when the temperature rises to temperatures above $100K$, all ice on the grain will be sublimated. This phenomena is visualized in Figure 1.6. As the gasses, dust and ice-particles from the outer parts of the molecular cloud fall towards its center, the whole system will start to rotate to conserve the angular momentum. When the pressure and temperature inside the center of the collapsing cloud are sufficiently high for Hydrogen fusion, a protostellar core is formed. The infalling matter from the collapsing molecular cloud will ensure it continues to grow. After the collapse this will result in a flattened disk, referred to as the accretion disk as can be seen in Figure 1.7 [18]. From the cross section of the disk in this figure can be noticed that there is still a significant amount of ices present in the accretion disk. The gasses and dust in the disk close to the star block part of the stellar radiation so that it is possible for ices to be present at a distance much closer to the star than without this blocking effect. The distance at which the first ice can be found from the star is called the "snowline".

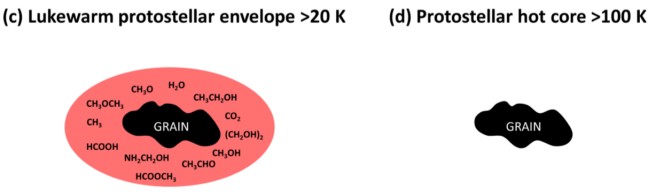


Figure 1.6: After Figure 1.4, the collapse of the molecular cloud is initiated, the temperature starts to rise (>20K) as a protostar is forming which causes the CO-ice on the grains to sublimate (c). The complex remainders of the chemical reactions, initiated by the UV-light, are left on the grain. At last, these remainders will sublimate as well and no ice will remain on the grain (d). Credit Öberg et al (2010).

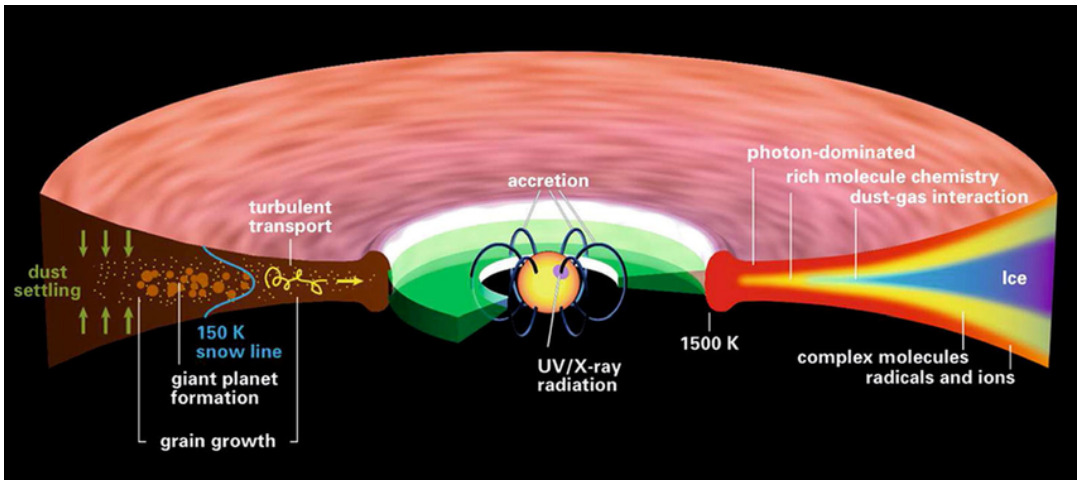


Figure 1.7: Cross section of the accretion disk. This picture visualizes that gasses close to the star and at the upper and lower limit of the accretion disk have a blocking effect on the stellar radiation. This is why the snowline that entails H_2O-ices is closest to the star at the midplane of the disk. Credit Henning and Semenov (2013).

When the star stops accreting dust and gasses, the disk becomes a protoplanetary disk. In this phase, small grains in the disk start to stick together, called sedimentation. This can increase particles from millimeters to centimeters. The relative motion between these particles and the dust in the disk enhances further growth. These particles can start to collide, which increases their growth rate. Larger particles can start to become planetesimals ($> 1km$) that are large enough to have a stable orbit. By collisions with other large planitesimals, they grow bigger until they become planetary embryo's. They accrete by attracting planetesimals and other planetary embyo's with their own gravity. Since their growth rate is proportional to their radius squared (R^2) which is called runaway growth [33], larger planetary embryo's will grow faster than small ones. Runaway growth of a planetary embryo stops when it has accreted all planetesimals within its gravitational reach.

1.3. Ices in the solar system

1.3.1. Late Heavy Bombardment (LHB)

The Late Heavy Bombardment is the hypothetical result of the Nice model. In this model the planetary cores of the planets in our solar system already formed and had circular orbits. At a distance of ~ 30 AU is assumed that there was a massive disk of planetesimals [8]. For a very long time the mass of this massive disk exerted a gravitational force on the outer planets in our solar system (Uranus and Neptune). This caused both of their orbits to become unstable and they were pulled out of their resonance orbit with Saturn [27]. Uranus and Neptune were scattered outward [9] because of this instability and they had close encounters with Saturn and Jupiter. They crossed the massive planetesimal disk which decreased the eccentricity and inclinations of their orbits that caused their orbits to become stable. By doing so, the planets passed by some planetesimals that changed the planetesimals' orbit towards the inner solar system. Lots of icy planetesimals were catapulted into the inner solar system [17], which caused highly energetic collisions on the inner planets. The "bombardment" of the inner planets by the icy planetesimals is called the "Late Heavy Bombardment" and this has been a noticeable source of water for the terrestrial planets including the Earth.

1.3.2. Comets

A well known water ice resourced celestial body everyone has heard of is a comet. They are objects with a high orbital eccentricity and semi-major axis. The ice on comets froze before the birth of our solar system. It formed as ice on the dust grains in the molecular cloud and ever since it went through the entire evolutionary process of the solar system as we know it today.



Figure 1.8: Comet McNaught over the Pacific Ocean. Credit Paranal Obeservatory - European Southern Observatory (ESO).

Comets are known for their beautiful appearance in the sky that could be seen with the naked eye as shown in Figure 1.8. The visible part only takes a short amount of the entire period because of their high eccentricity and consists of a dust tail and a coma. As a comet approaches the sun and crosses the snowline, the ice starts to evaporate on the comet, this forms an optically thick "atmosphere" of sublimated water ice which is called the coma that can become up to $10^5 km$. The dust tail is formed by the evaporating coma and can extend from $10^6 km$ to $10^7 km$. Since the evaporated dust reflects part of the sunlight, this becomes a tail that is visible to the naked eye. Apart from a dust tail, there is also a plasma tail that can exceed $10^7 km$ in length from photoioization of the volatile gasses and charge exchange with solar wind protons. This process ionizes a lot of neutral molecules, radicals or atoms. As solar radiation passes through CO^+, the plasma tail will have a dark blue color but sometimes, when H_2O^+ will be abundant throughout the vaporized gasses, the ion tail will turn red.

There are two distinct types of comets to differentiate: The short period comets ($P < 200 yr$) and the long-period comets ($P > 200 yr$). The big rearrangement in the solar system, caused by the LHB, created the planet-crossing centaurs which feeds the population of short-period comets. These types of periods are again divided into comets with an orbital period below 20 years, called the Jupiter-Family Comets (JFC's) and comets with orbital periods between 20 and 200 years which are called the Halley-type comets. Because the periods of these comets are relatively short, they are predictable with a high accuracy. Long-period comets in general have their aphelion beyond the Kuiper belt which makes their periods to last for at least 200 years which makes predicting these orbits very difficult. Objects residing in the Oort cloud can have several orbits around the Sun, but comets with a semi-major axis larger than 1000 AU are believed to make their first entry in the solar system after which the comet is catapulted into interstellar space.

1.3.3. Moons and icy bodies

Behind the snowline, it is cold enough so that ices do not sublimate and around the giant planets, some moons are mostly made of ice. The moons and icy bodies in our solar system all have different properties and different compositions. A variety of the most interesting icy moons are presented in Figure 1.9.

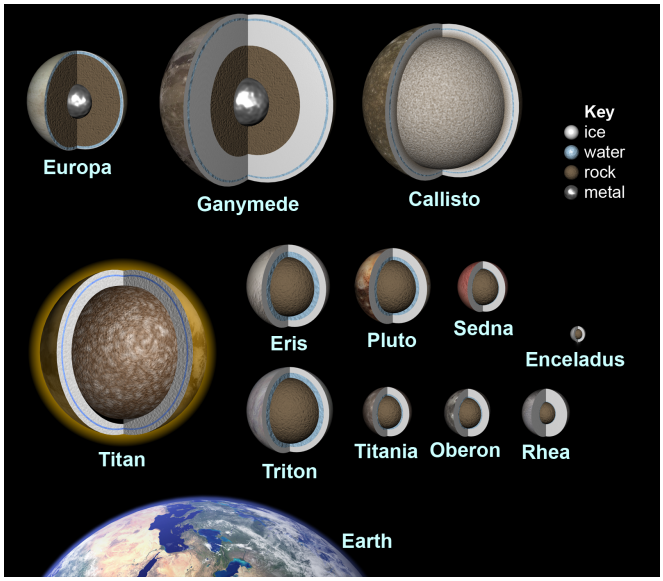


Figure 1.9: Interiors shown of icy bodies in the solar system. Credit Doug Ellison, Emily Lakdawalla, and Bob Pappalardo. Internal models based mostly on Hauke Hussmann, Frank Sohl, and Tilman Spohn, 2006, except for Titan (Giuseppi Mitri et al., 2010) and the Galilean moons (Bob Pappalardo, personal communication).

The closest ice moon to the center of the solar system is Europa which is orbiting Jupiter. Measurements of Europa imply that about 90% of its mass is in the rocky mantle of which the remaining 10% is from an H_2O layer. This layer is covered with ice on the exterior which might extend from $\sim 100-150km$ thick. Underneath the ice layer, it is possible to have H_2O in a liquid phase, such sub-surface oceans are now thought to be promising places for the search of extraterrestrial life. Europa, Ganymede and Callisto contain salt water. The salinity in these moons tend to increase with depth. More distant icy moons, like Enceladus and icy dwarf planets are likely to have colder, ammonia-water based oceans.

1.3.4. Other places

Other than on comets and icy moons, H_2O-ice can also be found in special regions on the other rocky planets in our solar system, with the exception of Venus. On Mars, H_2O-ice has been observed near the North- and South-polar regions due to seasonal variations in temperature. Viking observations indicate that there may be surface H_2O ice near the southern perennial CO_2-ice cap (Figure 1.10.

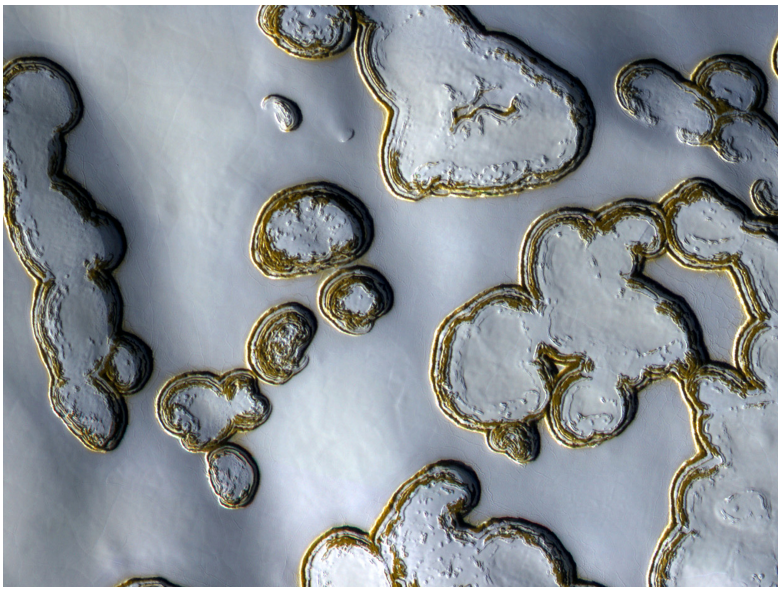


Figure 1.10: Picture of the Mars Reconnaissance Orbiter (MRO) showing the perennial southern CO_2 ice-cap. The cap is ~ 3 meters thick and is penetrated by flat pits as shown. Credits NASA/JPL-Caltech/University of Arizona

Furthermore, even on Mercury, the planet closest to the sun, water ice can be found. Even though the surface can become as hot as 430°C at its equator, the temperature near the poles is cooler. Here you can also find so-called "permanently shaded" craters. Because these craters are located near the poles, sunlight will never reach the bottom of these craters. This is where water ice can remain intact because of the constant low temperature. Evidence of this ice is presented in Figure 1.11. Our Moon also has permanently dark places near the poles where water ice can be found similar to this example.

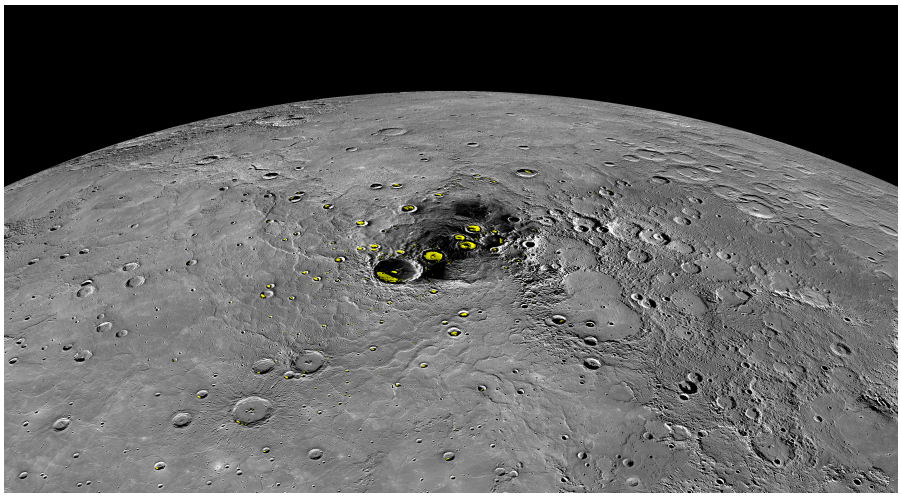


Figure 1.11: Picture by the Mercury Dual Imaging System (MDIS) of the MESSENGER spacecraft showing Mercury's north polar region. The yellow-marked areas in the picture show evidence of water-ice inside permanently shaded craters. Credits NASA/Johns Hopkins University Applied Physics Laboratory/Carnegie Institution of Washington

1.4. Ice Characterization

The characterization of ices in space is made possible by the collaboration between observations in space, laboratory experiments and computational simulations. The observations provide us with spectral information that can be used to estimate compositions of ices and gasses. Laboratory experiments aim to simulate events from space to get a better understanding of the physical and chemical processes that are going on during certain events. Finally, computational simulations are meant to prove theories with physical and chemical models. The main benefit of this method is that it doesn't require the same level of hardware as for experiments or observations which can be expensive.

1.4.1. Ice Composition

The composition of ices in space is estimated by means of spectroscopy. Stars emit light with a distinct electromagnetic spectrum. Therefore it can reveal the presence of inter-laying matter such as ices and silicate dust grains.

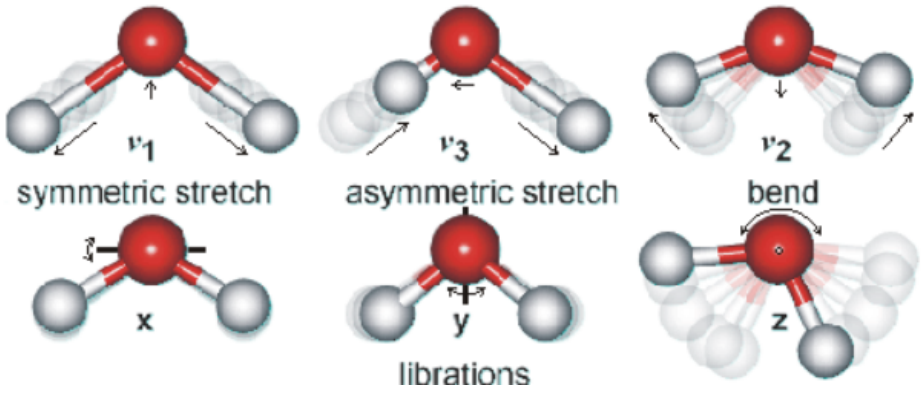


Figure 1.12: Molecular vibrational modes for H_2O [7]. Credit Martin Chaplin.

Because molecules absorb light at different frequencies, one could estimate the amounts of several molecules in between the background star and the observer by comparing the undisturbed spectrum of the background star with the observed one. The presence of absorption peaks at certain wavelengths can indicate the presence of different molecules.

When molecules absorb radiation, this energy is converted into vibrations. The vibrational modes of H_2O are graphically presented in Figure 1.12. Every type of vibrational mode has a different absorption wavelength that you can find back in the observed spectrum (see Figure 1.13). For H_2O, the wavelength ranges for its different vibrational modes are displayed in Table 1.1.

Wavelength	**Molecular Vibrational Transitions**
1-3 μm	Combination and overtone modes
3-6 μm	Stretch vibrations
6-30 μm	Bend and libration vibrations
25-300 μm	Torsional and inter-molecular (lattice) modes

Table 1.1: Molecular vibrational transition of interstellar ices in the near- to far- infrared [5].

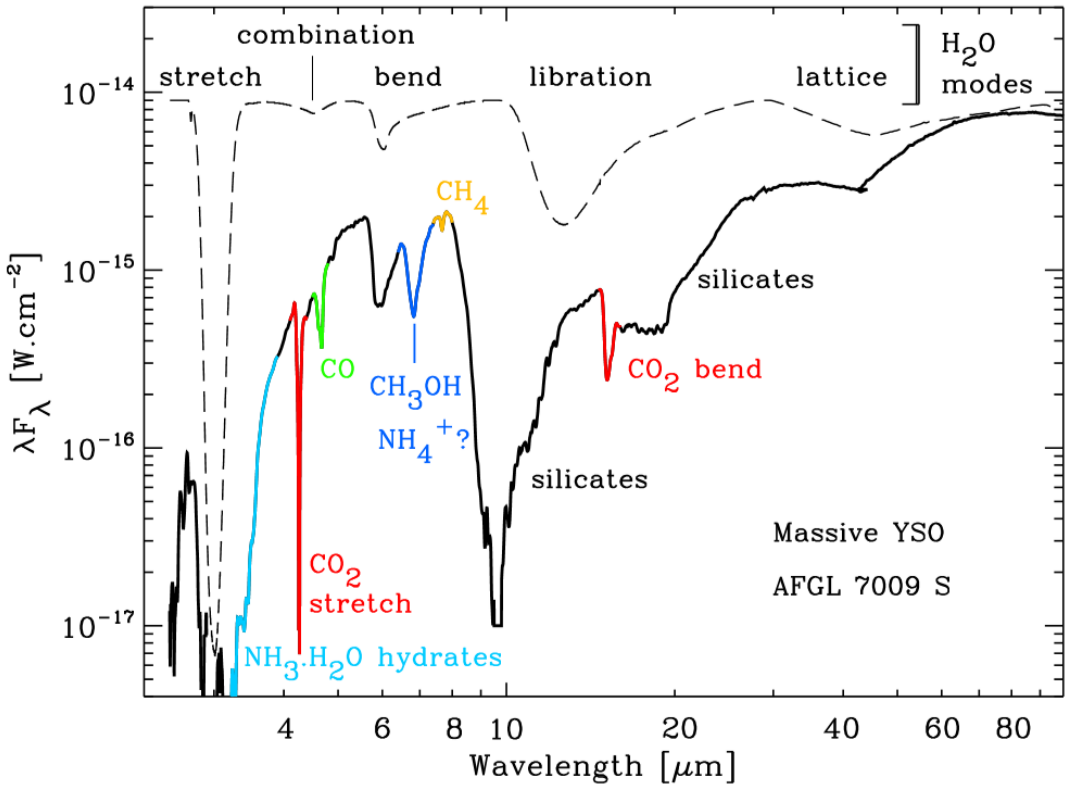


Figure 1.13: Spectral bandwith of Massive Young Stellar Object (YSO) AFGL 7009 S. Detected species are marked in the graph. Species that are not positively identified are indicated with question marks. The dashed line represents the calculated spectrum of ice spheres at 10K. In this spectrum, the bands, caused by the molecular vibrational transitions are indicated. Credit Boogert et al (2015).

In laboratory experiments, one tries to replicate the conditions in space to verify the spectral contribution of various compounds. Also the effect of a number of mixtures on the EM-spectrum is an interesting field of laboratory research. Fraser investigated the spectral signatures of CO and layers and mixtures of it with CH_3OH, CH_4, CO_2 and $HCOOH$. In Figure 1.14 can be seen how the presence of other compounds influence the spectral signature of the CO-stretching mode during Temperature Programmed Desorption (TPD) experiments. These results can help with identifying the subtle presence of certain compounds, mixed or layered with CO-ice, from spectral observations.

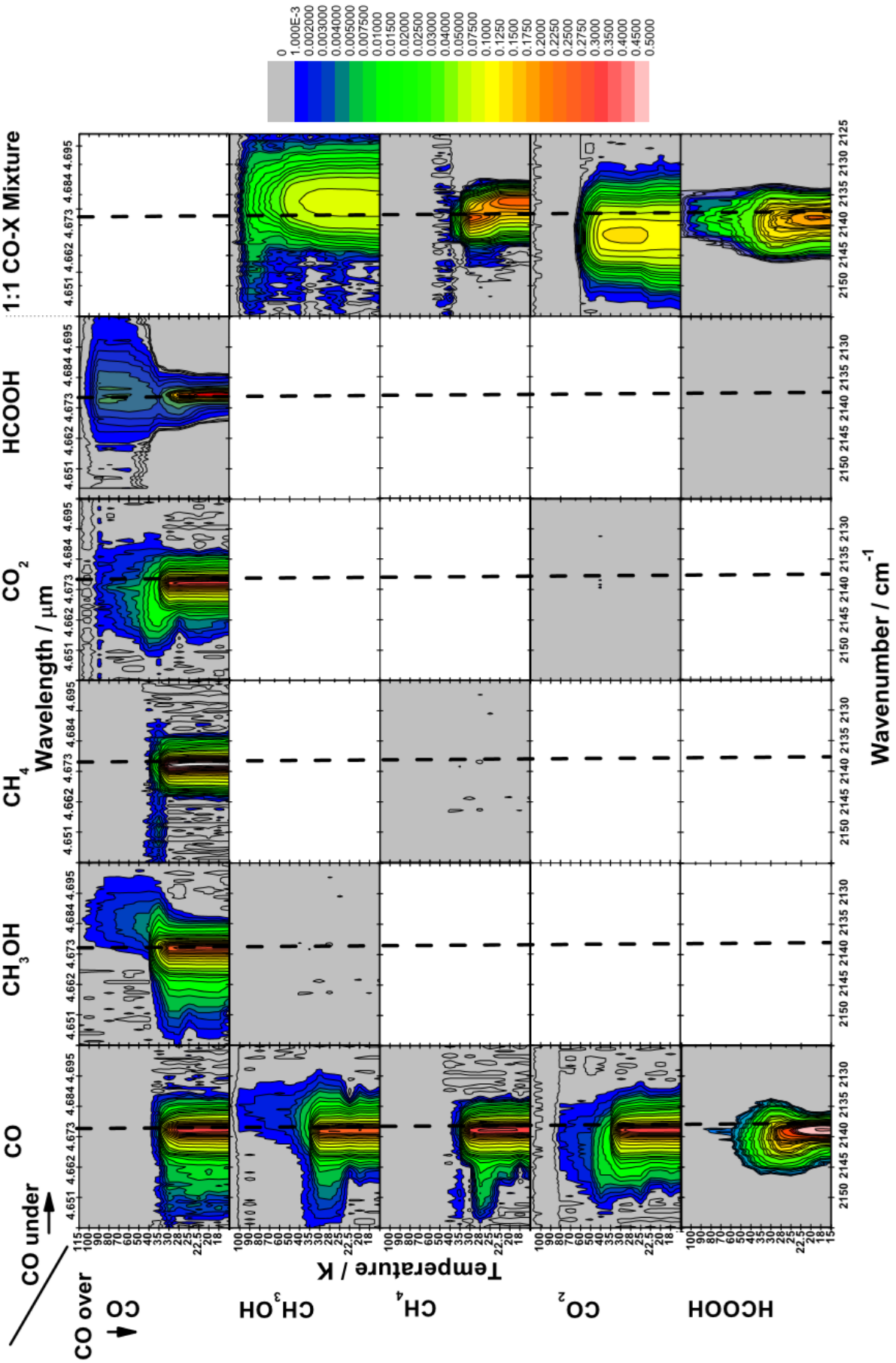


Figure 1.14: This image shows the evolutionary spectra of *CO*-layered and *CO*-mixed ices in the region of the *CO*-stretching mode with wavenumber range 2155 – 2121$cm^{-}1$. Credit Fraser.

Martín-Doménech [24] performed experiments using Temperature Programmed Desorption (TPD) of precometary ices that consist predominately out of water. The experiments are done using a KBr substrate and they are labelled from E1 to E11 and have an individual ice composition as presented in Table 1.2 E1 to E5 are experiments with pure ices, while E10 and E11 are ice mixtures with compositions that have been found in pre-cometary icy environments. E6 to E9 are additional experiments with different compositions to study particular effects. The superscripts $^{(a)}$ and $^{(b)}$ are used to show that the heating rate is 1K/min and 2K/min respectively.

Exp	H_2O [%]	CO [%]	CO_2 [%]	CH_3OH [%]	NH_3 [%]	$N/10^{15}$ $[mol/cm^2]$
$E1^a$	100.0	0.0	0.0	0.0	0.0	1554.61
$E2^a$	0.0	100.0	0.0	0.0	0.0	104.97
$E3^a$	0.0	0.0	100.0	0.0	0.0	134.88
$E4^a$	0.0	0.0	0.0	100.0	0.0	190.81
$E5^a$	0.0	0.0	0.0	0.0	100.0	154.60
$E6^b$	100.0	7.8	6.8	1.6	0.0	308.69
	86.1	6.7	5.8	1.3	0.0	
$E7^b$	100.0	6.6	27.9	3.0	3.4	1395.54
	70.9	4.7	19.8	2.2	2.4	
$E8^b$	100.0	0.0	0.0	9.3	0.0	109.52
	91.5	0.0	0.0	8.5	0.0	
$E9^b$	100.0	0.0	0.0	68.6	0.0	385.58
	59.3	0.0	0.0	40.7	0.0	
$E10^b$	100.0	8.7	20.0	5.7	5.7	749.50
	71.2	6.2	14.4	4.1	4.1	
$E11^a$	100.0	15.0	10.3	7.2	8.0	912.43
	71.2	10.7	7.3	5.7	5.1	

Table 1.2: Experiments E1-E11 are performed to investigate the thermal desorption features of H_2O-rich ice analogs. For experiments with two rows, the first one shows the composition relative to the abundance of ice while the second row resembles the absolute composition. $^{(a)}$ Heating rate = 1 K/min $^{(b)}$ Heating rate = 2 K/min Credit Martín-Doménech et al. (2014)

1.4.2. Porosity in ice

When water ice accretes at very low temperatures ($T < 100K$) it will be Amorphous Solid Water (ASW). Water in this form cannot be found in nature because of its harsh conditions. Comets, however, contain ice from the time before our solar system started to shape itself. Therefore, their ice was amorphous when it started to grow. With the formation of the solar system, the increase in heat turned some of the water ice from an amorphous structure to a crystalline one. Because the molecules resettle in a more organized, less random, crystalline structure, the pores inside these ices become larger. This process makes comets more porous which allows for other molecules to meet and possibly react inside these pores. The formation of a crystalline lattice structure from amorphous ice by increasing the ice temperature was simulated [6] and presented in Figure 1.15. In this figure the colour represents the number of neighbours every water molecule has. As can be seen, this number increases with increasing temperature (until 100K in this simulation). Figure 1.16 can be seen as a negative of Figure 1.15 because this is related to the number of empty cells. Here the number of adjacent empty cells around a cell is given by the distinct colours. In Figure 1.16 it is clear that the pore sizes in the ice grow remarkably when heat is applied.

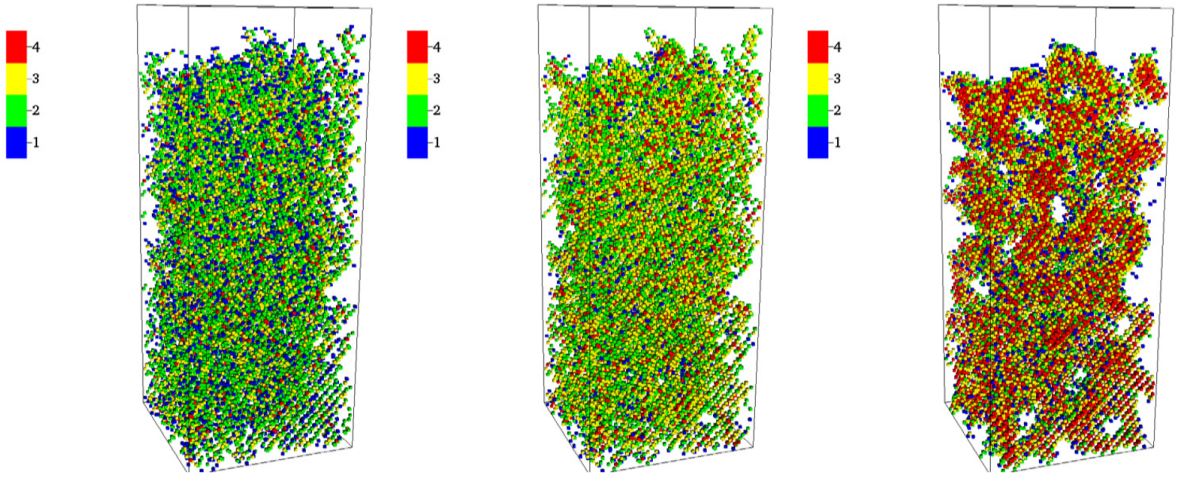


Figure 1.15: Ice structure in a 60x60x150 grid. The temperature increased from 10K to 100K with a heating rate of 2K/min. The colours represent the number of neighbours of each water molecule. The grids shown are snapshots from the simulation. Condition from left to right: 10K; 60K and 100K. Credit Cazaux et al. (2015)

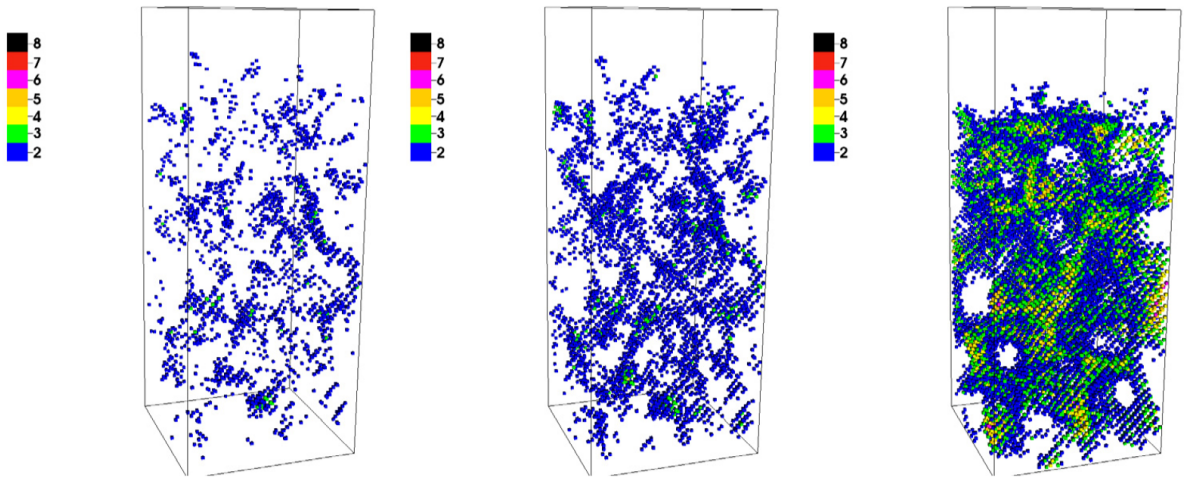


Figure 1.16: Pore distribution in a 60x60x150 grid. The temperature increased from 10K to 100K with a heating rate of 2K/min. The colours represent the number of empty cells around a cell. The grids shown are snapshots from the simulation. Condition from left to right: 10K; 60K and 100K. Credit Cazaux et al. (2015)

With laser measurements, an estimation of the size and its gravity potential, it is possible to estimate the porosity in comets. The result gives a ratio of pores and the total volume of the comet, or a ratio of ice with the total volume of the comet. Unfortunately, this technique doesn't allow for pore distributions in comets to be detected. On a laboratory scale, porous ices are created by directing the inlet tube of the deposition gasses away from the substrate on which the ice will be deposited. By doing so, the molecules are allowed to have random movements to enhance random freezing positions on the substrate. For pure ice depositions, the inlet tube is directed towards the substrate so that compact ices can be made by front deposition. The thickness of the ice is measured by a polarized Helium-Neon laser beam (632.8nm) that reflects on the ice and the substrate at an angle of 45°. A photodiode will observe the refracted laser beam in order for the morphological ice properties to be detected.

1.5. The ISAC

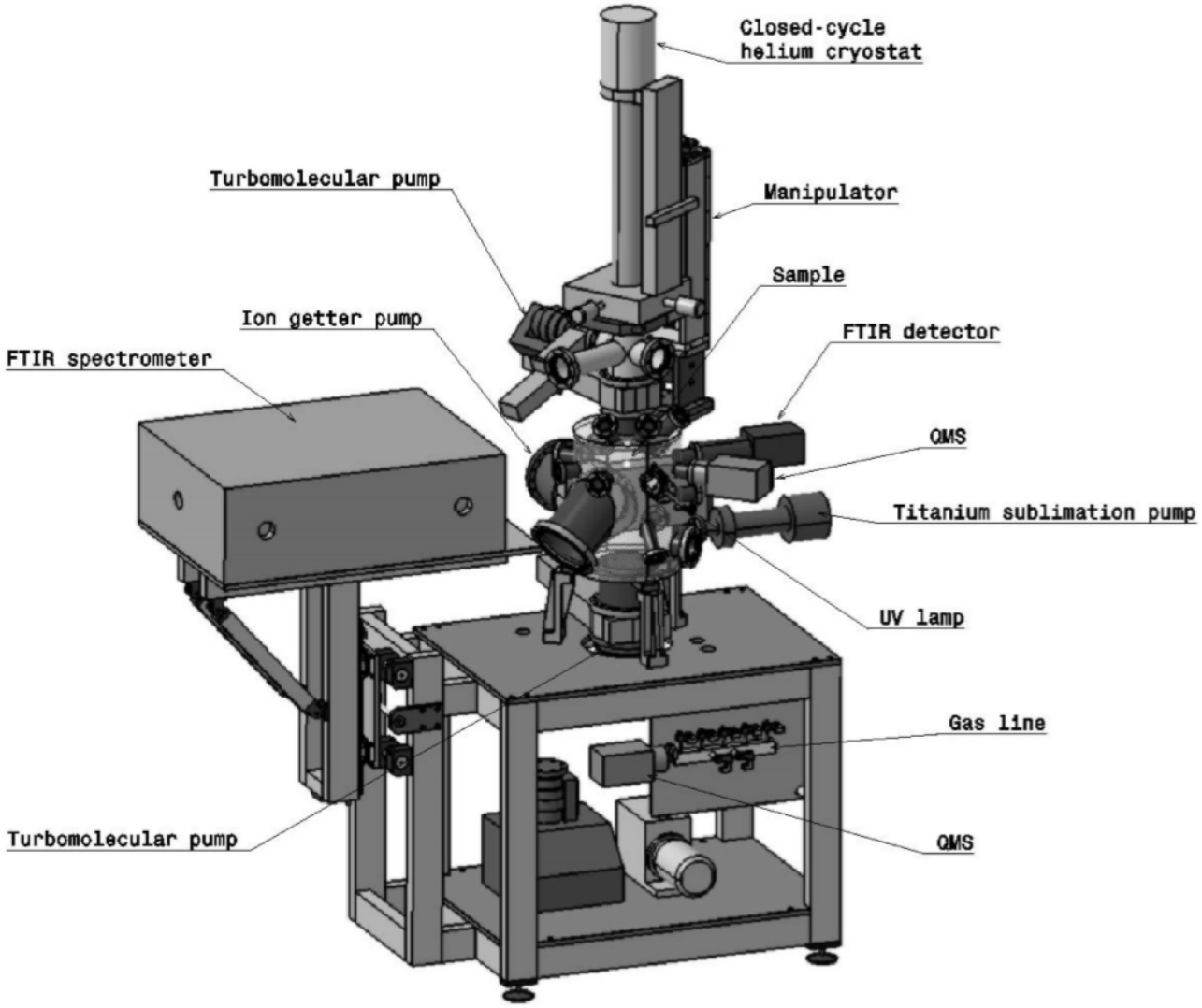


Figure 1.17: Lay-out of the experimental setup of the Interstellar Astrochemistry Chamber (ISAC). Credit Muños Caro et al. (2010)

1.5.1. Lay-out

Experiments to determine the porosity of interstellar and circumstellar ices are done using the Interstellar Astrochemistry Chamber (ISAC) at the Centro de Astrobiología (CAB) in Madrid (Spain). The lay-out of the experimental setup is shown in Figure 1.17. The figure shows how the setup is built up and points out the location of several important components around the vacuum chamber. Section 1.5.2 provides a brief description of the measurements that can be made with ISAC and Section 1.5.3 emphasizes more into the functionality of every component individually.

1.5.2. Description of ISAC

The ISAC is a system that aims to replicate the interstellar and circumstellar conditions in an Ultra-High-Vacuum (UHV) chamber in order to grow ice mixtures onto a substrate. The prechamber of the system allows for gas mixtures to form and for their introduction into a vacuum environment. After the mixtures in the prechamber have the desired composition and pressure, they can flow to the main UHV-chamber in which pressures of $2.5 - 4 \cdot 10^{-11} mbar$ [22] can be reached by means of a series of UHV pumps. The substrate is mounted on a cryostat (*cold finger*) which can cool down the ice samples down to 10K. After the ice is formed, the sample can be warmed up to simulate the conditions during stellar formation which helps to understand

the processing of the ices.

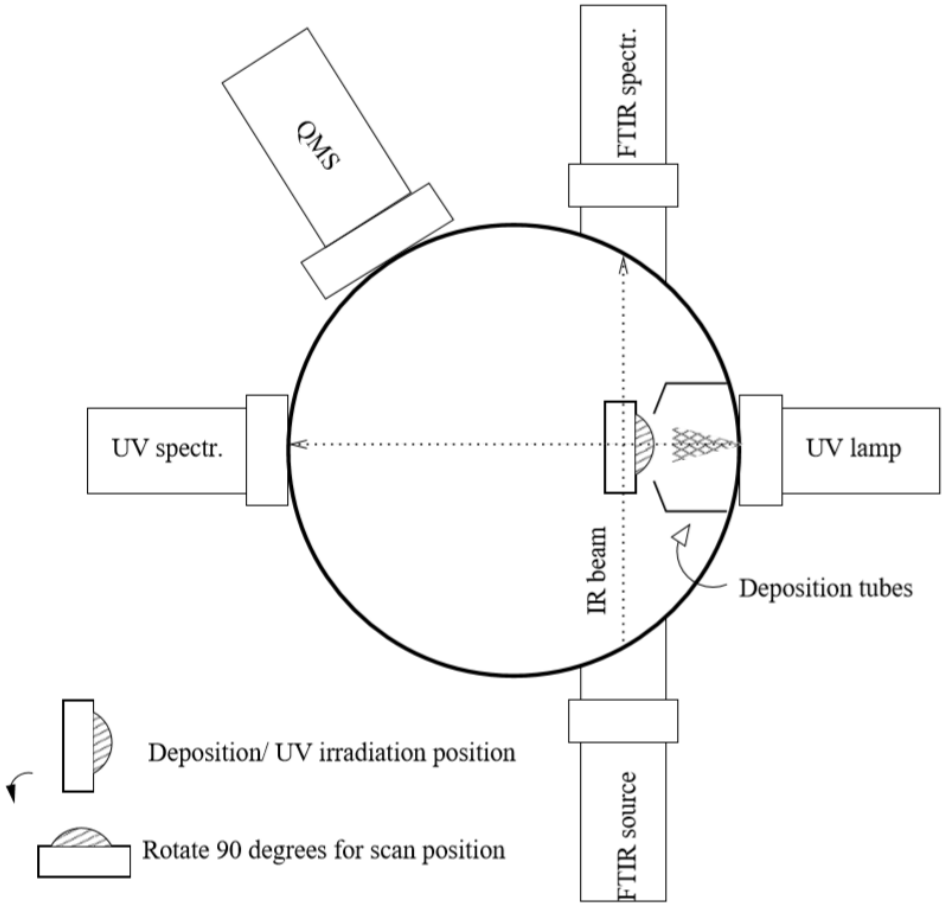


Figure 1.18: Sketch of the geometrical lay-out of the main Ultra-High-Vacuum (UHV) chamber. An ice sample is grown on a transparent substrate while a UV-lamp controls the non-thermal desorption and the decomposition of species. For a spectral snapshot, the substrate has to rotate 90°for geometrical purposes that can be seen in the figure. The Quadrupole Mass Spectrometer (QMS) monitors the volatile gasses throughout an experiment. Credit Muños Caro et al. (2010)

The substrate is a transparent window at infrared wavelengths at which the sample grows, located at the intersection of the UV-lamp and the Fourier-Transform-Infrared (FTIR) spectrometer. The positioning of the instruments around the substrate is sketched in Figure 1.18. The UV-lamp provides the desired amount of UV-radiation: High UV-radiation leads to desorption and decomposition of species; Low UV-radiation allows for fast adsorption of species at low temperatures. Spectral data can be obtained by the FTIR spectrometer, but to enable spectral measurements in the infrared spectrum, the substrate has to be rotated at an angle of 90°for geometrical purposes that can be seen in Figure 1.18. Furthermore, a Quadrupole Mass Spectrometer (QMS) is added to monitor the volatiles of the system [22].

1.5.3. Component description of ISAC

This section entails a brief description of the functions of each individual component of the ISAC. Most of these functional components are pointed in Figure 1.18.

Closed-Cycle Helium Cryostat + Substrate

The closed-cycle Helium cryostat is a device that is capable of cooling down a substrate to 10 K. It uses helium to cool the substrate down because helium is one of the only gasses that remains in a gaseous state at a temperature of 10K. The substrate, attached to the so called "cold finger", at which the ice sample will grow which is attached to the tip of the cryostat. In order to be able to perform FTIR spectroscopy on this sample, the substrate is an infrared transparent window made of CsI or KBr. At certain moments throughout the experiment, the cryostat has to be rotated 90° in order to perform spectral measurements.

Prechamber
A small prechamber is mounted on top of the main UHV chamber. This is the chamber in which the gas samples are introduced to a vacuum of about $10^{-9} mbar$. From the prechamber, the gasses are injected or extracted from the system by a vertical translational motion of the cold finger. The prechamber itself is equipped with a fast entry lock, a pumping system independent of the one from the main UHV chamber consisting of a turbomolecular pump (TMP), a rotary pump, and a titanium sublimation pump (TSP). Furthermore it encompasses a cold finger with a sample holder which is mounted on a tube to be able to rotate it.

Main Chamber
The main chamber is the place where the sample ice is created by deposition of the gasses. The inside of the main chamber is covered with Mu-metal to prevent magnetic fields to interfere with the experiments. An optical guide (cylindrical quartz tube) is mounted between the UV-lamp and the sample holder to maximize the flux at the sample position.

UHV Pumping System
The pumping system consists out of a series of pumps in order to obtain a pressure of $\sim 2 \cdot 10^{-11} mbar$. The system entails 2 turbomolecular pumps, a rotary pump, a titanium sublimation pump and a non-evaporable ion getter pump.

UV Lamp/Uv spectrophotometer
The UV lamp is inserted to simulate the spectral conditions in the ISM. The lamp is a microwave stimulated hydrogen flow discharge lamp which is attached outside of the main chamber in front of a MgF2 window. The hydrogen is excited by a $100W$ microwave generator. Furthermore, the opposite side of the main chamber is equipped with a UV spectrophotometer to monitor the UV flux during the experiments.

Fourier Transform Infrared (FTIR) System
The FTIR system consists out of an FTIR source and an FTIR detector. They are positioned on the opposite side on the exterior of the main chamber behind ZnSe windows and are operational in the spectral range between $1.3 - 27 \mu m$ (~wavenumber $7500 - 370 cm^{-1}$).

Quadrupole Mass Spectrometer (QMS)
The QMS detects volatile gasses that are ejected from the ice and the QMS is able to measure the gas composition in the main UHV chamber as it is equipped with a Pfeiffer prisma with a spectral range from 1 to 200 amu. Consequently, it can also measure the deposition of the gasses.

Gas Line
To create a mixture of gasses to be frozen onto the substrate, the mixture has to be made in the gas line. The gas line allows for making gas mixture of up to 5 species. The most abundant species in interstellar ices are H_2O and CH_3OH, in fewer abundances CO, CO_2 and CH_4 are present. The gas line allows for making mixtures up to this complexity. A QMS is used in the gas line to measure the composition of the mixture in order to obtain a desired mixture.

Ultrasonic System
This system was not originally part of the ISAC, but as the thesis studies the development of an ultrasonic device for the measurement of porosity in interstellar ices, this might be implemented. The design, testing, and first measurements with this ultrasonic device were performed in a simpler vacuum chamber constructed for this purpose.

1.6. Ultrasound

Acoustic pressure waves that travel through a certain medium with a frequency beyond the hearing of humans ($\sim 20kHz$) are used in ultrasonic measurement techniques to reveal discrepancies that are not externally visible without any risk of damaging the measured medium. There is a wide range of practical applications for ultrasound on Earth, but using this in space is not straightforward since there is no medium for the acoustic waves to travel through. Most extraterrestrial applications of acoustic measurements are in the form of seismometers. Seismic experiments have been used to reveal interior properties of the Moon and Mars by measuring the vibrations on the surface when small meteorites crash by means of accelerometers. Although there are a lot of similarities between these seismic experiments and the applications that would be possible to perform on comets, a major difference is that frequency of seismic waves is below the frequency limit of the human hearing ($\sim 20Hz$) and therefore in the infrasonic regime instead of the ultrasonic one. This is why this section will be provided with applications on Earth after explaining the basic principle.

1.6.1. Principle

Transducers are piezoelectric devices that are used to send and receive ultrasonic vibrations. The transducer used for the experiments that were performed during this thesis is shown in Figure 1.19. When an ultrasonic pulse is emitted by a transducer, it travels through a certain material to be inspected or looked within with the ultrasonic speed of sound of that medium. Any surface that the ultrasonic wave encounters induces an echoing response. This is a reflected ultrasonic signal that can be captured by the same or another transducer. The Time of Flight (ToF) is the time difference between the sent pulse and the retrieved signal. From the properties of the material, the phase velocity v of an ultrasonic signal is known which makes it easy to determine the difference in distance to the transducer $\Delta z \approx \Delta t \cdot \frac{c}{2}$ [37]. In case the same transducer is used for emitting and receiving ultrasonic waves, the distance of the reflection surface can be calculated by multiplying half of the ToF with the ultrasonic velocity. Figure 1.20 shows how reflected surfaces are spotted during an inspection measurement with a moving transducer. Because the ultrasonic velocity is much faster than the speed of the transducer moving from left to right, it doesn't influence the calculation of the depth in the material. Therefore instantaneous radial (z-direction) readouts can be obtained and ultrasonic scanning measurements can be transformed into a map. Different types of these scans will be entailed on in Section 1.6.3.



Figure 1.19: Picture of the V317-SU immersion transducer ($20MHz$) used in the experiments during this thesis. Credits Olympus Corporation

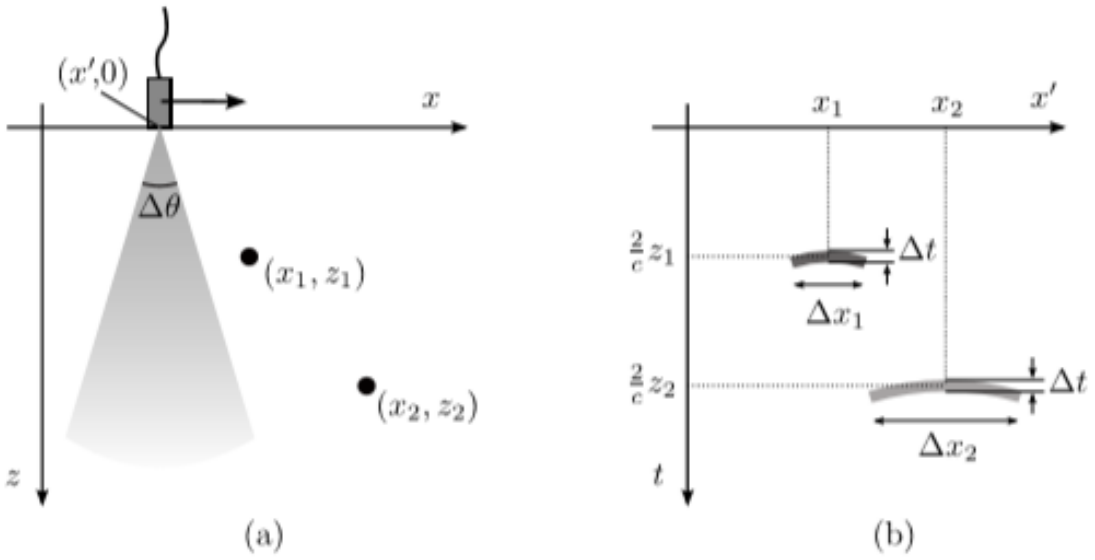


Figure 1.20: Pulse-Echo response from one moving transmitting/receiving transducer. a) Set-up of the measurement b) Mapped response of the measurement. Credit Skjelvareid (2012).

1.6.2. Types of applications

Because ultrasonic signals reflect on physical boundaries within a medium it wants to pass through, a number of interesting applications were developed and listed below.

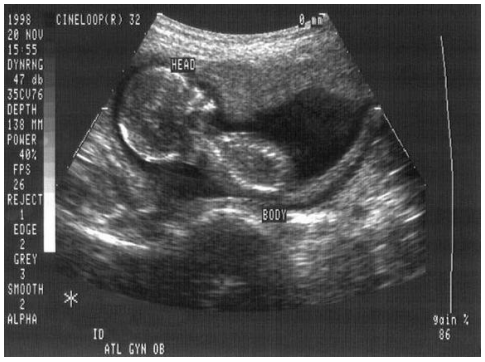


Figure 1.21: Ultrasound is used in echography for imaging this 4 month old fetus. Credit Tanya Lewis (livescience.com).

Medical ultrasound
Ultrasonic visualization is commonly used in medical applications: For visualizing body structures such as tendons, joints, blood vessels and muscles but also a fetus in a womb (Figure 1.21) and tracing tumors or other irregularities in organs or veins. Ultrasonic scanning of the human body can serve as a safer alternative for scans with harmful radiation.

Non-Destructive Testing (NDT)
NDT is a favoured way to perform maintenance inspections for Quality Assurance (QA) and Quality Control (QC). Ultrasonic measurements can obtain the thickness of basins filled with chemicals or pipes with running liquids without the need to empty it first. This allows for maintenance during operation which can potentially reduce a significant amount of costs on maintenance. Furthermore, cracks in materials that are under mechanical strain can be spotted so that weak spots can be identified before they cause malfunction or complete failure.

Short-distance measurements
Ultrasonic transducers, optimized to propagate through air are mostly used as an alternative method to measure distance remotely. This type of transducer is widely used by the drone and automotive industry to measure distance between a drone or a car and obstacles. Recently, more and more car manufacturers add these transducers to enhance their automated adaptive cruise control-, self driving- and collision avoidance systems.

Aerospace
In the aerospace industry ultrasonic scans are used to check the manufacturing quality of carbon fiber based composites. Misalignments of the fibers or small discrepancies such as bubbles in between two plies can reduce the failure strength of carbon fiber composites significantly. Since a composite part might not show this to the naked eye after manufacturing, it is recommended to frequently check the build quality of the batches that are produced. For maintenance it is also important to perform similar ultrasonic scans to make sure the plies are not starting to detach at some places or cracks start to form that need to be treated.

1.6.3. Visualization

To be able to draw meaningful conclusions, ultrasonic measurements are often presented in ways that are more straightforward to interpret. In this section, a number of types of ultrasonic scans are presented and discussed. Depending on the application used, a different scan can be preferred to present the measured data.

A-Scan
Ultrasonic A-scans normalise the intensity of the amplitude of the retrieved signal. The result is that the envelope of the amplitude is made visible in this scan. An example [37] of an A-scan is shown in Figure 1.22 which is a scan on an aluminium plate. Note that the smaller peaks after the first one are attributed to internal reflections in the plate.

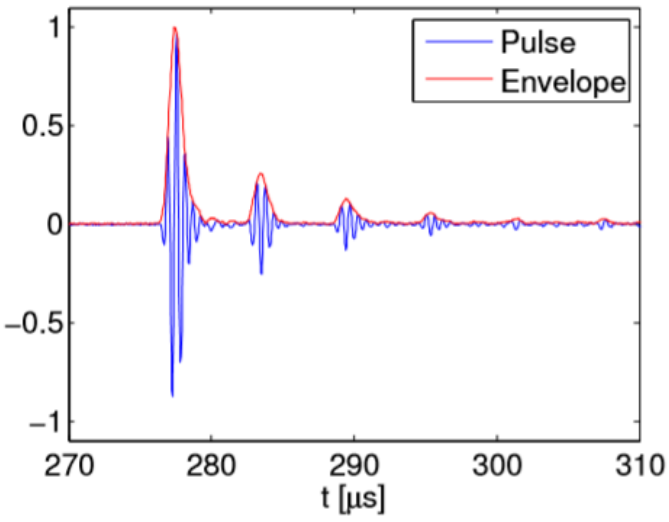


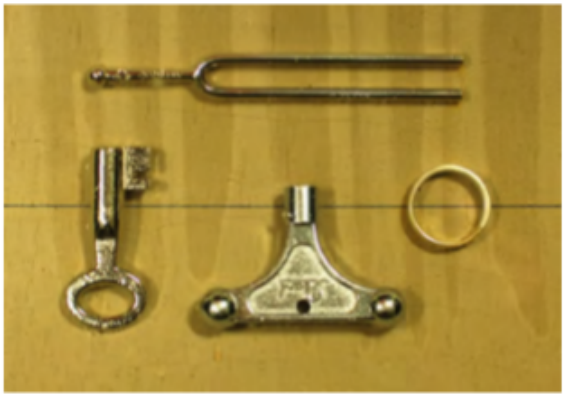
Figure 1.22: Example of an A-scan observed by pulse-echo measurement. Credit Skjelvareid (2012).

B-Scan

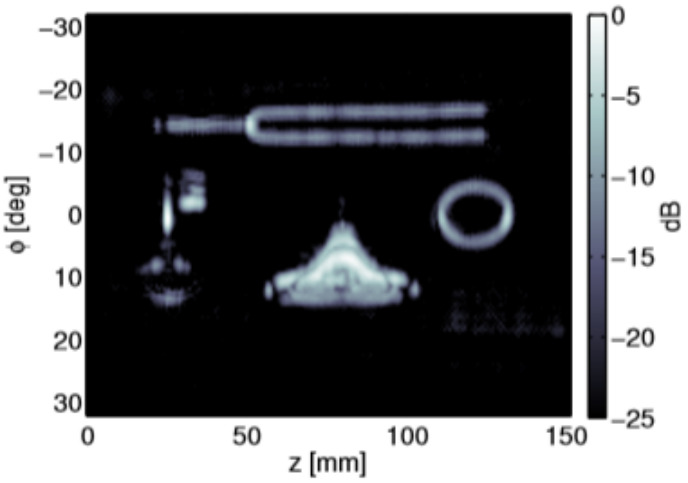
A B-scan gives an extra dimension to the ultrasonic measurements. This type of scan shows multiple measurements at once. A set of measurements can be obtained by an array of transducers (to get an instantaneous measurement) or by a single transducer over time. If a measuring single transducer has a controlled motion in a certain direction, the same results can be retrieved as for an array of transducers. Usually the delay time of the reflected signal is present on the Y-axis and the X-axis can be the time between single measurements, or distance as shown in Figure 1.24. This figure shows the measurements of a piece of acrylic with 4 holes drilled in it. As can be seen, the intensity of the returning signal drops significantly with increasing distance in the material.

C-Scan

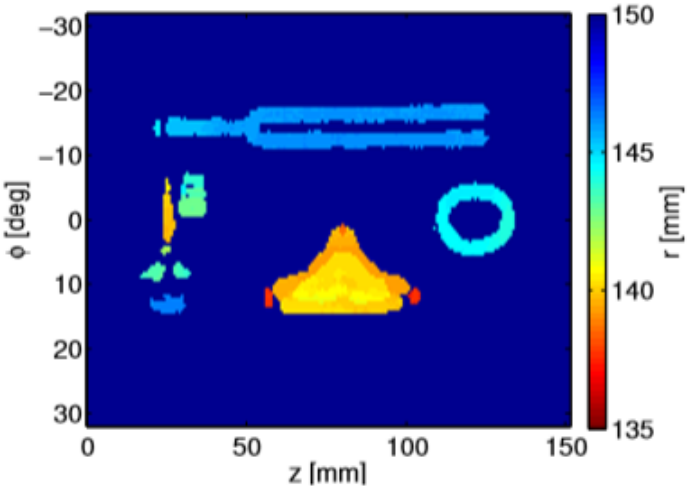
In a C-scan, measurements are taken from a measuring 2D plane. The measurements can be taken with a single transducer, that has a controlled linear movement along an X-, or y-axis or angular movement of one or both of these axis. To reduce the time necessary to take this type of scan, an array of transducers can be used so that more scanning area can be covered at once. Figure 1.23 on the right shows an example of a C-scan. The 4 objects that are shown (a) were placed inside a pipe. They were detected with ultrasound and an image was created of their amplitudes (b) as well as the distance from the transducer (c). The amplitude picture shows that the objects can be identified from the scan. The distance image gives additional information that is not even present in the original picture at (a). Here the distance to the observing transducer is visualized on the colour scale which reveals how deep the objects are in the picture. Here it becomes clear that they are laying inside a pipe (because the lower objects are closer to the observing transducer(s) than the upper ones).



(a) Photography



(b) Amplitude C-scan



(c) Distance C-scan

Figure 1.23: This figure shows (a) a picture of four metal objects that are put in a pipe. Nonetheless the C-scan was able to scan for their amplitude (b) and distance (c) Credit Skjelvareid (2012).

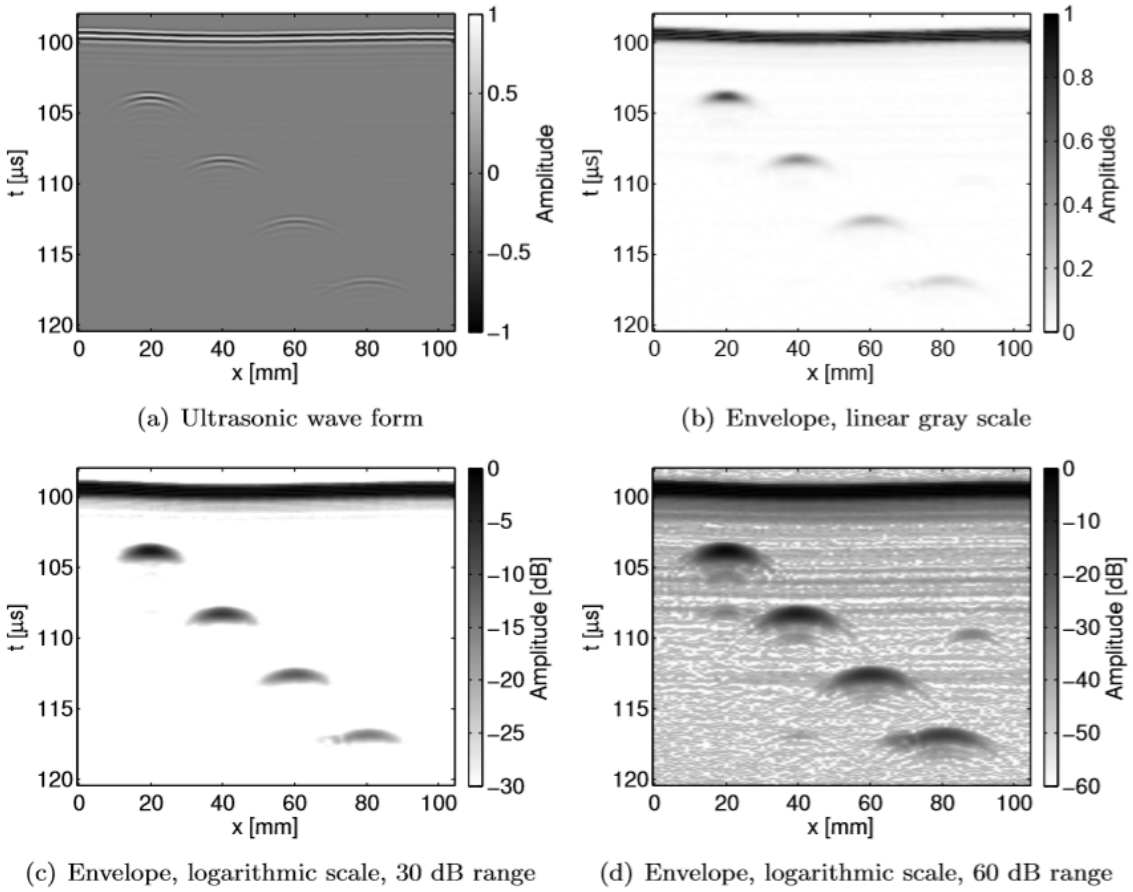


Figure 1.24: B-scans of block acrylic with four drilled holes in it. (a) shows the amplitude of the raw wave and (b) is the B-scan plotted with a linear scale while (c) and (d) are plotted with a dynamic range of 30 dB and 60 dB respectively Credit Skjelvareid (2012).

1.7. This Thesis

In this thesis, research is performed on ultrasonic propagation in cryogenic ices and the influence on porosity in such a medium. Therefore, the main part of the thesis (except for the conclusion) consists out of 5 Chapters in which Chapter 2 is a descriptive chapter about the setup of the vacuum chamber and the relevant components and equipment that is used during the experiments. After the functionality of the equipment becomes clear Chapter 3 shall emphasize on the experiment methodology that follows a roadmap. The way the experiments are approached and which ones follow other ones up chronologically is explained here in great detail. Chapter 4 shows how simulations helped with the design choices concerning the thermal properties of the "Seta" which is a methacrylate substrate on which the ice is grown in the vacuum chamber. This chapter furthermore focuses on simulations that visualize the propagation of ultrasound and the readings the ultrasonic transducer should get from the receiving signals. The ultrasonic propagation in the "Seta" and in a frozen drop of water are also part of this chapter to be able to know what to expect from such experiments. Chapter 5 shows how a series of drop experiments at atmospheric pressure are kept to determine the speed of sound in the water drop and additionally, how porosity effects ultrasonic propagation. The experiments of the vacuum chamber are summarized in Chapter 6. These consist of the experiments with the initial small vacuum chamber that has been improved during this thesis. This improved design was ultimately adapted in such a way that it can quickly freeze liquids while keeping the transducer measuring the ultrasonic properties. A brief conclusion with results, the outcome of this thesis and possible future applications are summarized in Chapter 7. Lastly, experimental studies generate a lot of information that might be useful to mention but not relevant enough to discuss in the core of the thesis since it could be thought of as redundant. The appendix contains the total roadmap discussed in Chapter 3, the result of every single drop experiment from Chapter 5 and the relevant plots of every experiment done with the vacuum chamber from Chapter 6.

2

Experimental setup

2.1. Ice drop experiments

To save valuable time and to gain insight in the influence of porosity on ultrasound, a number of experiments were performed outside of the vacuumchamber, with ice grown directly on top of a transducer with two piezo-electric elements to act as a transmitter and a receiver. In these experiments, the ice is grown inside a freezer. After the drop is frozen, the transducer will be connected to the pulsar and an oscilloscope to obtain the ultrasonic signals. Figure 2.1 and Figure 2.2 visualizes the setup throughout the experiment. The final experimental configuration has the capability of measuring the water drop when it freezes. This is made possible by maintaining the cable connection between the pulsar and the transducer.



Figure 2.1: Drops of water are created on top of the transducer. The transducer with water drop is put inside a freezer for 20 minutes.

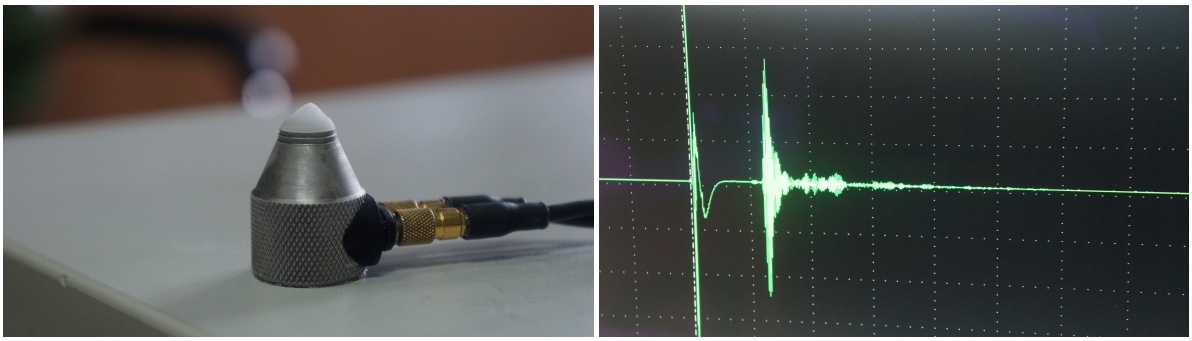


Figure 2.2: Left: Frozen drop on the transducer. Right: Direct reading of the ultrasonic signal.

2.2. Mobile vacuum chamber

Apart from the ISAC vacuum chamber at CAB, a new and smaller vacuum chamber was developed to perform the first experiments with ultrasonic measurements. Since the use of ultrasound is unprecedented in combination with vacuum chamber experiments, the ISAC should be adapted to perform such measurements. However, the implementation of ultrasound would cause a significant downtime for the ISAC vacuum chamber and a small and portable vacuum chamber was developed. Such small chamber allows to perform experiments with ultrasound and to test how this could be implemented in the future in ISAC. When demonstrated experiments, within the limits of its capabilities, have a positive outcome, the addition of an ultrasonic system in the ISAC at the CAB can be justified. The fact that it is small, influences some vacuum chamber parameters. The Ultra-High Vacuum that can be achieved by the ISAC vacuum chamber has an operating pressure range between 10^{-9} and 10^{-12} millibar while this chamber can hardly reach $2 \cdot 10^{-3}$ millibar which can be categorized as a "Medium Vacuum". With the addition of a Turbomolecular Pump (TMP), the vacuum is likely to improve into a "High Vacuum" category ($< 10^{-3}$ millibar), but this has not been realized during this thesis.

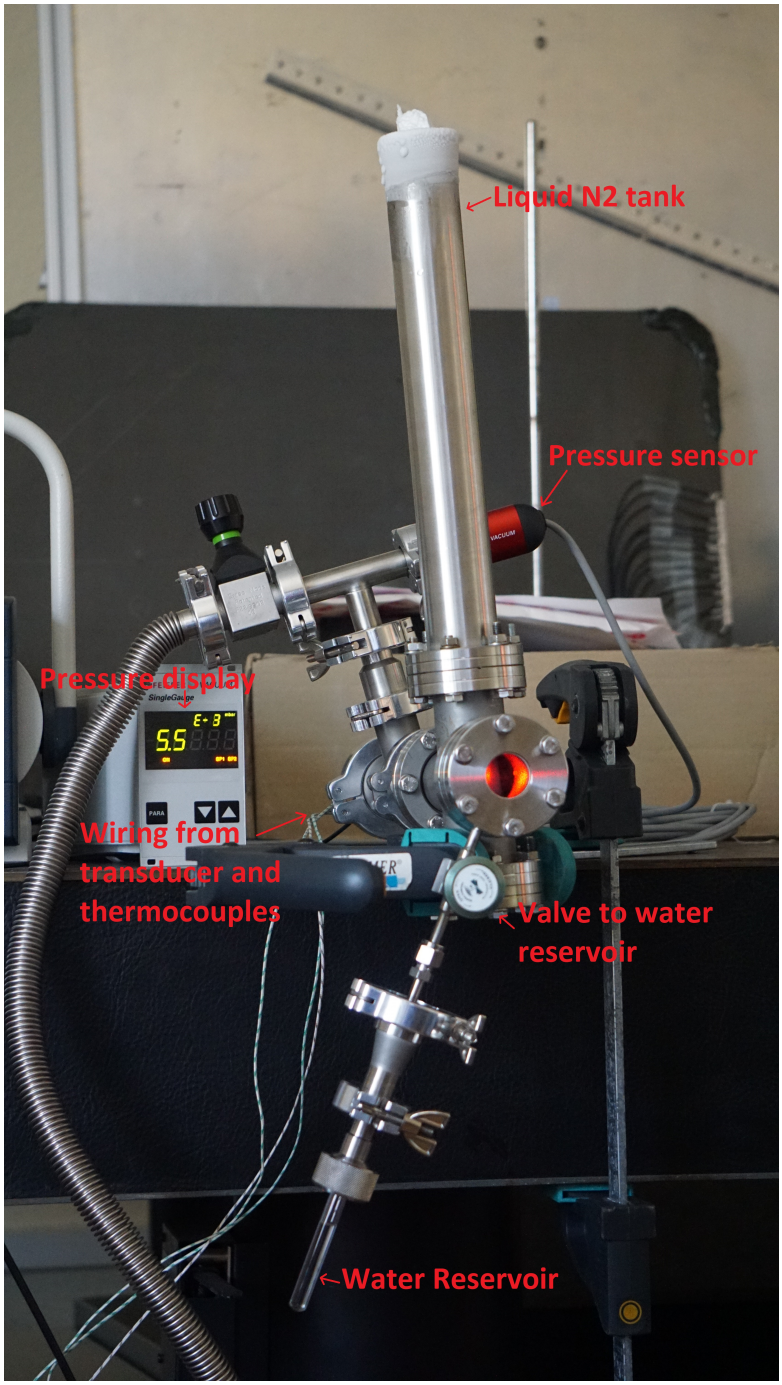


Figure 2.3: Setup of the mobile/small vacuum chamber. Functional components on the picture are labeled.

2.2.1. Lay-out

The mobile or small vacuum chamber is a vacuum chamber that is made in such a way that it is easy to transport by car (from CAB to ITEFI) and easy to assemble. A picture of the lay-out of the mobile vacuum chamber is shown in Figure 2.3 and a sketch of the system can be found in Figure 2.4. Here several important components are labelled.

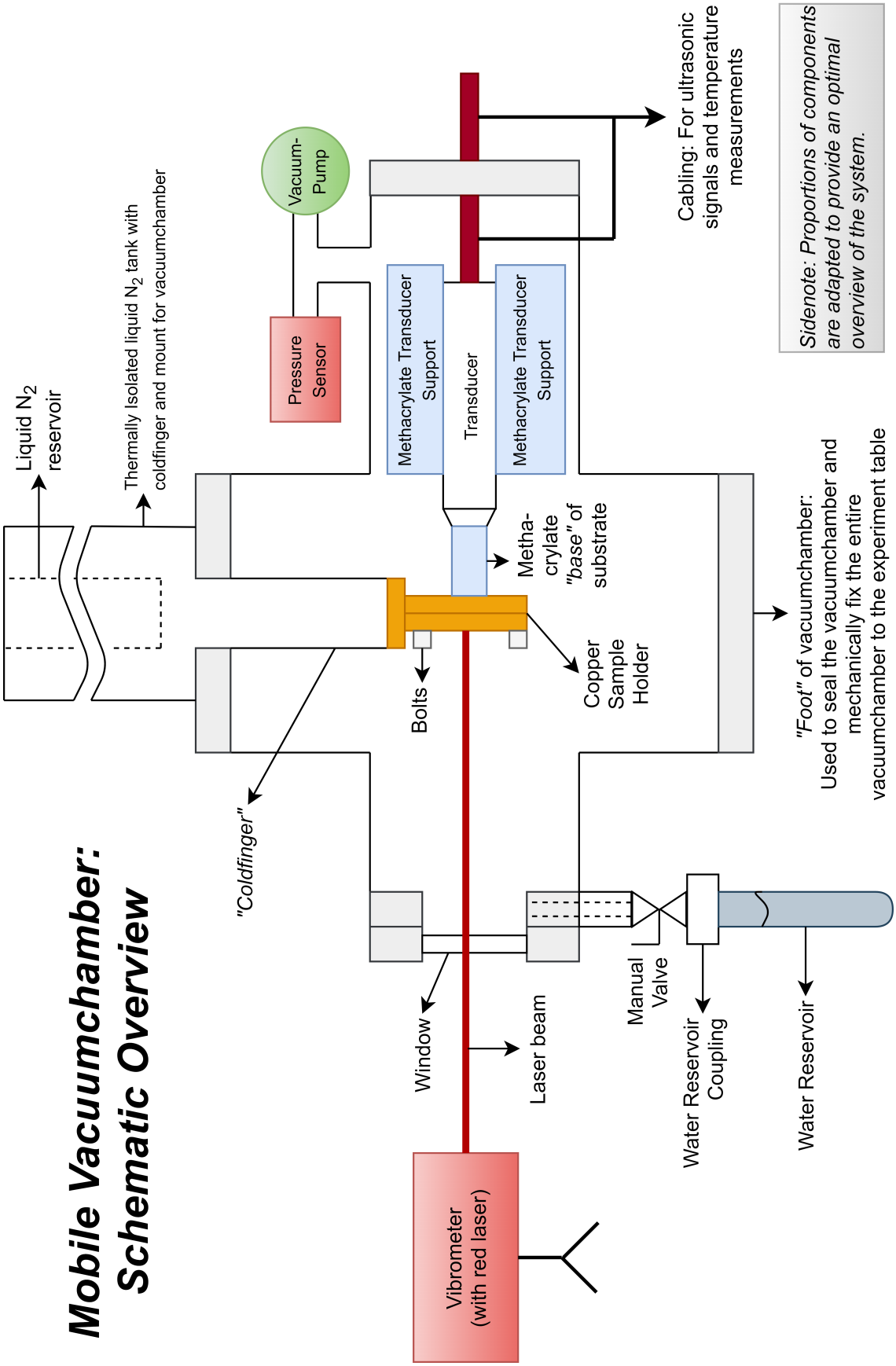


Figure 2.4: A schematic overview of the mobile vacuum chamber, including key-components such as the transducer and vacuumpump, to provide more detail in the way it functions.

2.2.2. Description of the mobile vacuum chamber

The mobile vacuum chamber is specifically designed to be small and portable to be able to demonstrate the use of ultrasonic devices in vacuum with the aim to estimate the ice thickness of ices grown on the methacrylate substrate. Before the start of an experiment, the vacuumpum will create a vacuum inside the chamber. When the pressure inside the vacuum chamber stabilizes, the liquid nitrogen can be poured into its reservoir. This will start the cooling of the coldfinger and the sample holder. The liquid N_2 reservoir needs to be re-filled frequently during experiments to ensure a cold temperature can be maintained. Furthermore, temperature sensors will provide temperatures of the sample holder, the *"mesa"* (the dish shaped part of the methacrylate component where the deposition takes place), the *"base"* near the transducer (the cylindrical methacrylate extention part, mounted on the transducer) and the vacuum chamber structure itself. The pressure sensor makes sure pressure data is displayed during the experiment and saved in a data-file on the computer. The transducer is attached to an oscilloscope that sends ultrasonic pulses and measures the response with a high frequency so that it will provide the ultrasonic measurements. Lastly the vibrometer was positioned in order to measure the ice thickness with high accuracy. Its laser enters the vacuum chamber through a window and then captures its reflection on the ice.

Because its vacuum is poorer than the ISAC at CAB, ice is being deposited at higher pressure levels which speeds up the experiment time significantly. Since this system works with liquid nitrogen instead of liquid helium, the deposition temperature will be higher. But since water ice doesn't require such a low temperature, the use of liquid nitrogen is sufficient (and much cheaper). Another big difference is that this system doesn't have the same level of control as the ISAC. During deposition at higher pressures, more heat is introduced in the vacuum chamber then the sample holder and coldfinger can transmit away which will increase the deposition temperature noticeably with respect to the equilibrium temperature of the system.

2.2.3. Component description of the mobile vacuum chamber

This section describes every functional part of the mobile vacuum chamber in more detail to point at its experimental capabilities and limitations.

Liquid nitrogen (N_2) tank

In the mobile vacuum chamber, cold temperatures can be reached by using liquid N_2. To encapsulate the LN_2 while it is cooling down the system, the LN_2 tank has been developed that can be found at the top of the vacuum chamber in Figure 2.4. This part entails a storage compartment for the LN_2 within a thick (but hollow) isolation layer. They are attached to each other with a thermally low-conducting metal alloy to keep the thermal losses as low as possible. The bottom of the LN_2 tank is provided with a rod made of a thermally high-conducting metal alloy to ensure a good heat transfer between the liquid N_2 and the sample holder. This attached rod, the coldfinger, is the connecting piece between the LN_2 tank and the sample holder. The bottom of the coldfinger has a threaded hole to screw the sample holder into. Lastly, this part is provided with an integrated high vacuum connection so that it can be directly attached to to the chamber.

Liquid N_2 has a temperature of $\pm 78K$, but since the efficiency of the LN_2 tank can not be 100% perfect, the temperature at the end of the coldfinger during experiments would be higher. Simulations and data from performed experiments show that the temperature of the sample holder can be brought down ultimately to values slightly below 100K.

The storage capability of the LN_2 tank is rather low ($\pm 15cl$) to ensure it is sufficiently transportable. As a consequence, frequent LN_2 refills have to take place during the experiments. Depending on how much ice is deposited, more LN_2 might be necessary, but most of the experiments could be performed with 1 liter of LN_2.

Sample holder

The Sample Holder is shown in Figure 2.4 by the orange part in the middle. It is a copper assembly that clamps the Methacrylate Substrate mesa between two gold rings. The use of copper and gold in this assembly is chosen to optimize the thermal conductivity towards the methacrylate. The assembly consists of two copper plates with a hole through them and a pocket hole in the back plate so that the mesa of the methacrylate substrate fits into it. The mesa of the methacrylate substrate is clamped between two gold rings and the copper plates. The plates are mounted together with 4 screws. The copper back plate has a threaded bolt part

on top as well as a circular dish to increase the contact area when this bolt is screwed into the coldfinger. At the bottom of one of the copper plates, a thermocouple is mounted to measure its temperature. The thermal conductivity of the assembly is sufficiently high that the temperature of the sample holder can be considered constant throughout the entire assembly.

Methacrylate substrate (seta)

The substrate is the part, clamped inside the sample holder, on which the ice deposition and measurements take place. In Figure 2.4, the rod of the substrate can be found between the sample holder and the transducer. Usually, the constraints for this material come from the optical properties. But as the experiments with the mobile vacuum chamber are unconventional, the limiting constraints originate from the use of an ultrasonic transducer that requires physical contact with the substrate to measure the deposited ice. Since no commercially available transducer can withstand such extremely low temperatures, a new multifunctional piece was created for this purpose.

This new piece consists out of two parts, the *"mesa"* (table) and the *"base"*. The mesa is the part that replaces the conventional substrate, this will be the place the ice will be deposited on. The base is a rod with a co-circular smaller diameter that will physically connect to the transducer. The length of the base is proportional to the minimum temperature that can be achieved at the transducer. Because of the shape of this piece (mesa + base), it was named *"Seta"* (mushroom) since it is easier to refer to.

The material of preference for the seta became Polymethyl Methacrylate (PMMA), shortly methacrylate. This material provides sufficient thermal resistance to keep a minimum temperature higher than $-20°C$ while the optical properties are still sufficient for infrared (IR) spectroscopy experiments later on (to measure porosity). The ultrasonic wave velocity in methacrylate is close to the one for ice, which is beneficial for the transition of the ultrasonic signals at the boundary of the methacrylate substrate and the deposited ice.

Thermocouples were mounted on the mesa and the base. The thermocouple at the mesa is located close to the diameter of the base, so the actual temperature at the center of the mesa will be higher then the one measured by this thermocouple. The thermocouple at the base is located close to the transducer in order to get an accurate approximation of the minimum transducer temperature. In later sets of experiments, a third thermocouple is added halfway the base to get a better understanding of the thermal gradient inside the methacrylate.

Vacuum chamber

The main structure that is used for the vacuum chamber is a crossing of tubes provided with the necessary high vacuum connections. The intersection is where the ice deposition shall take place. This structure provides four entries towards the intersection, but the bottom one is sealed and is used as a *"foot"* for the system to support on. The top entry is used to mount the LN_2 tank with coldfinger on. The back entry has an elongating tube connected to it to provide a sufficient amount of space to mount the ultrasonic transducer here. The vacuum pumping system is also connected at the elongated part of the back entry of the vacuum chamber. The front entry is provided with a deposition ring and a sealing cap with a window in it. The deposition ring has a threaded hole, to provide the connection of the deposition system. The sealing cap with the window allows for the laser of the vibrometer to measure the deposited ice on the surface of the seta. The window can also be used to visually monitor the sample holder during the experiments. The vacuum chamber itself is drawn as a contour around the orange sample holder with the methacrylate substrate in the sketch of Figure 2.4.

Vacuum pumping system

The vacuum pumping system consists out of a vacuum pump, a pressure meter (represented in green and red in Figure 2.4 respectively) and a display for the measured pressure. The pump can ultimately create a vacuum of about $2 \cdot 10^{-3}$mbar, but when the deposition valve is opened, higher pressures arise. In the future, with the use of an old Turbomolecular Pump (TMP), pressure regions of $\sim 10^{-6}$mbar will become available for the mobile vacuum chamber to experiment with. But the first set of experiments were performed without TMP.

Deposition System
The deposition system, on the bottom left in Figure 2.4, allows for control up to a certain extend over the deposition on the substrate in which the valve can be opened gradually in a manual way. The main elements in this system are, the deposition valve and the deposition tube. When the valve is closed, the deposition tube can be disconnected to refill the tube during the same experiment. The valve has to be opened and closed manually, but after a first set of experiments it became clear that opening and closing the valve interferes with the measurements from the vibrometer. This is why the use of an electronically controlled valve was considered for future experiments.

Ultrasonic system
The unprecedented type of measurements performed under vacuum conditions are the ultrasonic ones. Commercial transducers are not made for the conditions present in this experiment. But after some preliminary tests, the transducer proved to remain functional in a vacuum. Inside the vacuum chamber, the transducer is supported by a cylindrical piece of methacrylate that fits inside the the back entry of the vacuum chamber that can be seen on the right in the sketch of Figure 2.4. The cylindrical piece of methacrylate has a hole in it where the transducer is placed in. The measuring side of the transducer is fixed to the base of the seta with adhesive. The cable of the transducer goes out of the vacuum chamber through a seal cap designed for this purpose.

The transducer used for the experiments is the V317-SU immersion transducer from Olympus. The maximum frequency of the pulses for this transducer can go up to $20MHz$, but the measurements are chosen to be with a frequency of $2MHz$. This is because the software used can only save ultrasonic measurement data with a frequency of $200MHz$. This allows for smoother measurements at lower frequencies such as $2MHz$ instead of $20MHz$.

Laser vibrometer
A Laser Doppler Vibrometer (LDV), shown in red on the left of Figure 2.4, is used in the setup to measure the thickness of the deposited ice on the methacrylate. Instead of relying on the refraction of the laser signal in the ice, this technique uses the time between a sent laser pulse and its reflection. The device has a laser beam splitter internally. One of these beams goes directly to the object you want to measure (the deposited ice), the other one passes through a crystal with a high refraction index inside the device. After the beam comes out of this crystal, its characteristics are compared with the ones from the measurements. Based on their difference, measurements with incredibly high accuracy can take place. This way, the beam going through the internal crystal is used as a reference compared to the reflected beam coming from the measured object.

The use of this device in this setup is a challenge because it is hard to understand what the laser actually is measuring. Also the reflective properties of the window of the vacuum chamber are hard to deal with. On top of that the intensity of the reflected signal changes when ice is being deposited. Because of all the disturbing sources on a measurement that relies on a relative reference position, it requires a lot of knowledge about the device and how to tweak its settings which makes this a challenging instrument.

3

Approach

This chapter encompasses all the work (and future work) that would be necessary to obtain a relation between ultrasonic measurements and the porosity of a deposited ice. As can be seen in Figure A.1 in the appendix, the project is composed out of four main fields of research: Research & Simulation, Ice Deposition Experiments, Porous Ice Experiments and Concluding all results. This chapter will be used to elaborate further into every one of these fields. Note that almost all of the experiments shown in this figure are attributed to the mobile vacuum chamber at ITEFI. The initial plan was to implement the transducer into the ISAC vacuum chamber at the CAB after the detectability of ice growth with the setup of the small vacuum chamber at ITEFI. Unfortunately, no distinct time-of-flight (ToF) could be attributed to the ice analogs grown in the small vacuum chamber which lead to no implementation of the ultrasonic transducer in the ISAC vacuum chamber.

3.1. Research & Simulation

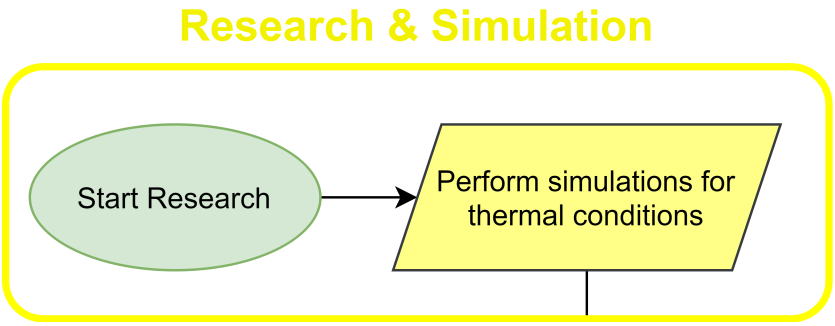


Figure 3.1: Before experiments will take place, sufficient simulations have to confirm the conditions in the vacuum chamber are not harmful for the transducer.

The first field of research in this study is the one before the actual experiments take place (Figure 3.1). This includes the literature study as well as the study of the setup of the ISAC at CAB and the mobile vacuum chamber at ITEFI.

Perform Simulations for Thermal Conditions
After familiarizing with these kind of vacuum chambers, a simulation was performed. Because the minimum operational temperature of the transducer is $-20°C$ as provided by the manufacturer, a substrate of methacrylate was chosen with an extending part towards the transducer so that the transducer is shielded from the very cold temperatures of the sample holder that is close to $100K$ ($= -173.15°C$). To verify whether the dimensions of the methacrylate substrate were appropriate to guarantee a sufficiently large temperature gradient, simulations are performed in Comsol Multiphysics. Firstly an accurate Computer Aided Design (CAD) model was made from the sample holder in Autodesk Inventor which could be easily implemented in Comsol. The simulations proved that the methacrylate substrate had suitable dimensions to shield the transducer from

the cold at the sample holder. The full extend of the simulations performed in detail and their results are presented in Chapter 4.

3.2. Ice Deposition Experiments

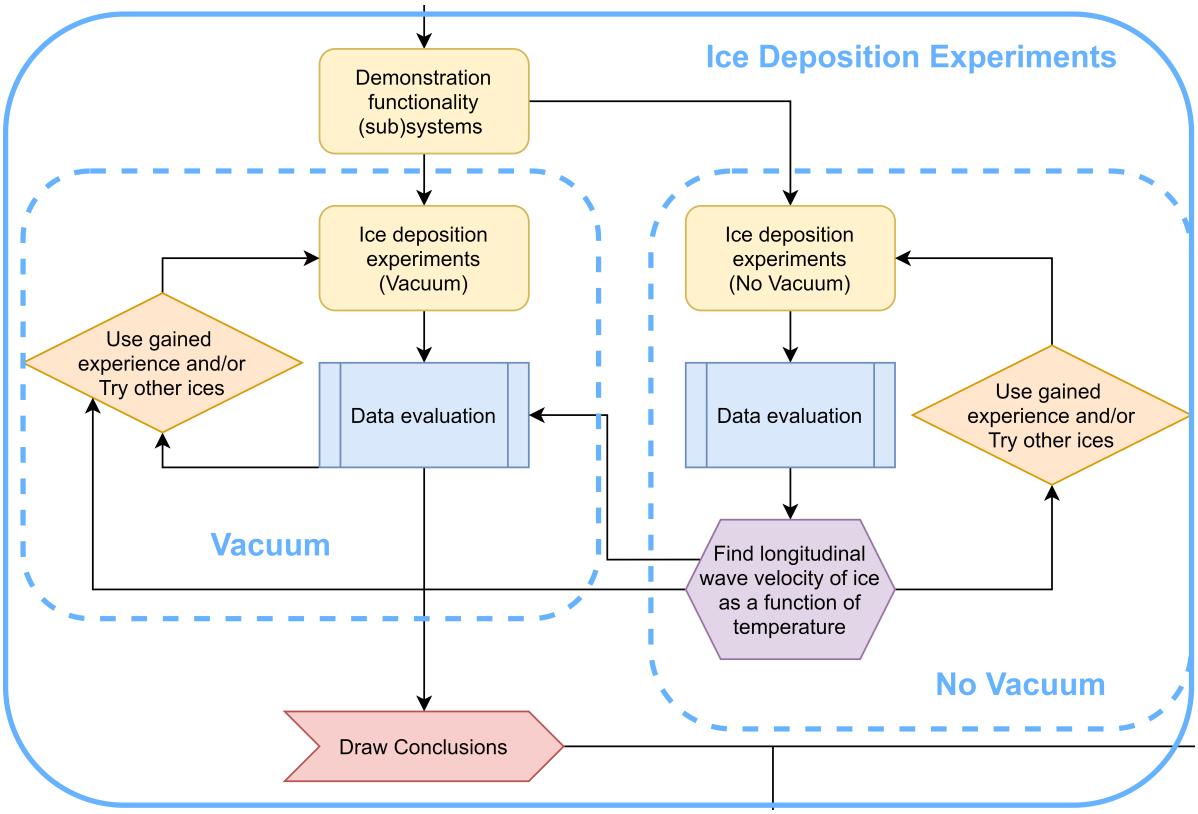


Figure 3.2: The first type of experiments entail the deposition of compact ices and the feasibility to find the acoustic speed of sound in the ices. The speed of sound in an ice as a function of its temperature will be found by experiments without vacuum. This knowledge is then used in the vacuum chamber experiments to compare the speed of sound for the different type of ice made here.

The first type of experimental research is done as described by Figure 3.2. Both, experiments with and without vacuum will be done after their data will be evaluated. The data from the experiments without vacuum will allow for the longitudinal speed of sound to be derived which will be useful to compare these findings to the results from the experiments done in a vacuum. This group of experiments aims to find the thickness of compact ices from ultrasound. From the block diagram in Figure 3.2 can be seen that there are two different sets of experiments: Experiments with vacuum and without a vacuum.

Demonstration Functionality (Sub)systems
The first experiment of its kind is meant to familiarize with the test setup and to test the instruments attached to it. This experiment is used to make sure all the important data is automatically saved and if necessary, some instrument parameters can be tweaked. This step is taken for both, the experiments with and without vacuum.

3.2.1. Experiments without Vacuum

Originally, the laser vibrometer was meant to measure the thickness of the ice in the vacuum chamber during the deposition. But since the laser vibrometer did not give satisfying results towards the measurement of the thickness of the grown analog because of the reflection of the window of the vacuum chamber, the experiments would be done without the front window at atmospheric pressure which eliminates the possibility of reflections from intermediate surfaces such as the window.

Ice Deposition Experiments
In the open chamber, the sample holder will be cooled first by the coldfinger. Meanwhile, the temperature and ultrasound are being recorded and the laser will record a distance difference that can be attributed to the thickness of a deposited layer of compact ice. After the methacrylate substrate cooled down suffiently, the deposition can start. An aerograph is used to spray water vapors on the substrate in a controlled manner in order to make a compact ice. The thickness of the grown ice layer is then measured by the vibrometer and the ice layer will provide a certain change in the ultrasonic signal as well. While depositing, the temperature of the substrate increases because the sprayed liquids (H_2O, CH_3OH, CH_3CH_2OH, ...) are at room temperature. As the ice layer cools down, the ultrasonic signals change because the temperature effects the acoustic velocity inside the materials while the vibrometer should keep on returning the same layer thickness.

Data Evaluation
From the ultrasonic data, the Time of Flight (ToF) of the ice can be isolated by applying a deconvolution technique. The ToF is the time the acoustic wave needs to go through the layer of ice and reflect its signal. Since the thickness of the layer is known from the vibrometer measurements, the speed of sound in this ice can be derived as shown by the equation below. In this equation v_L is the longitudinal wave velocity of the ultrasonic signal and t is the ice layer thickness.

$$v_L = 2\frac{t}{ToF} \tag{3.1}$$

Find Longitudinal Wave Velocity as a Function of Temperature
After the deposition, the temperature cools down until an equilibrium temperature is reached. Throughout this cool-down process, the ToF will decrease which will increase the speed of sound inside the ice layer. Using the recorded data, the longitudinal wave velocity in the ice layer can be plotted over time. In this step, a polynomial has to be found that matches the experimental data. This polynomial can then be used to calculate the thickness of ices from only ultrasonic measurements using vacuum experiments. Having this polynomial allows to calculate wave velocities even when temperatures in vacuum experiments are lower then the temperatures with ambient pressure.

Use Gained Experience and/or Try Other Ices
A number of similar experiments without vacuum are necessary to validate this polynomial. When the experiments are consistent, another ice can be experimented with such as CH_3OH (methanol), CH_3CH_2OH (ethanol) or maybe other.

3.2.2. Vacuum Experiments

Experiments with vacuum were performed at first, but since the vibrometer didn't provide satisfying results, experiments without the front window were performed. With the derived polynomials from the experiments without vacuum, the data of the earlier performed experiments can be used to calculate what thickness the ices were with those experiments.

Ice Deposition Experiments

Regular ice deposition experiments with vacuum start with creating a vacuum in the chamber. When the pressure stabilizes, LN_2 can be poured into the nitrogen tank to cool down the sample holder. Because the interface between the sample holder and the methacrylate substrate has a very small contact surface, the equilibrium temperature will not be much lower then $-90°C$. A first deposition by opening the deposition valve will allow water molecules to freeze anywhere on the sample holder, also in cavities due to surface irregularities between the sample holder and the substrate. This increases the thermal conductivity between them which allows for a much lower temperature of the substrate. After the first deposition, more ice will be deposited on the substrate.

After the depositions, when the LN_2 runs out, the temperature on the substrate rises and the ice starts to desorb. The magnitude of the desorption can be understood by looking at the pressure. The instruments kept on measuring during the desorption phase of the experiment.

Data Evaluation

From the ultrasonic measurements, B-scans can be made to look for the visibility of experiment phases. It can be noticed that the cool down of the substrate has a visual effect and when the deposition valve opens, steep features follow which is attributed to the rise in temperature by the deposition itself. From the polynomial obtained from the experiments without vacuum, the thickness of the grown ice layer can be calculated after deconvolving the ultrasonic signal for every experiment.

Use Gained Experience and/or Try Other Ices

Performed experiments are to be checked on consistency to verify a single result. This is done by comparing the experiments next to each other considering their results with their respective atmospheric conditions (pressure, temperature) with the aim to see patterns in the ultrasound. If results are consistent, the amount of deposited ice can be a factor to play with. This way the minimum thickness to be detected by the ultrasound can be found.

Other ices can be deposited as well such as methanol (CH_3OH). If the pumping system will be upgraded throughout this study, the possibility of depositing ethanol (CH_3CH_2OH) will arise.

Draw Conclusions

When the ice thickness of compact ices is determined by the ultrasonic measurements and validated by consistent results, the experiments with the deposition of compact ices can be concluded and their results will become a reference for future experiments with porous ices.

3.3. Porous Ice Experiments

After the thickness of compact ice layers during an experiment is demonstrated to be able to be derived from the ultrasonic measurements only, experiments with porous ices are next in line. Because of delays during the earlier types of experiments and the difficulty of this project, the experiments with porous ice are not likely to be held during the scope of my thesis. Nonetheless, the (simplified) approach of these experiments is described in this section.

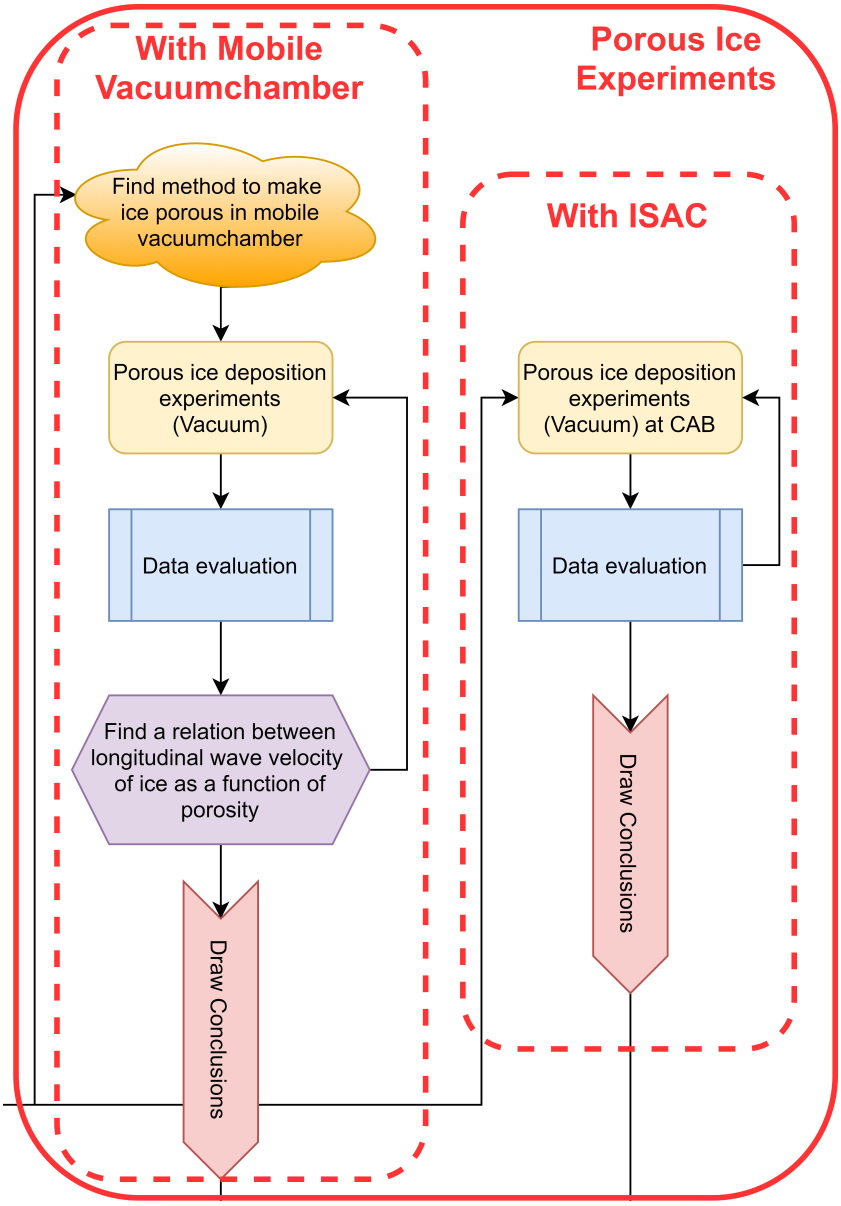


Figure 3.3: In the second type of experiments, porous ices will be deposited in order to find a relation between the ultrasonic measurements and the porosity of the ices.

3.3.1. With Mobile Vacuum Chamber

The difficulty of introducing porosity in ices grown in the mobile vacuum chamber lies in its environmental limitations. Usually amorphous water ice is formed after which it is slowly warmed until the temperature becomes high enough for the ice to become crystalline. This introduces a rearrangement in the positions of the water molecules, increasing the porosity in the ice. But since temperatures in the mobile vacuum chamber cannot become sufficiently low to deposit amorphous ices, another method has to be thought of.

The ISAC is capable of producing amorphous ices with a high accuracy (to resemble cometary ices), but the introduction of an ultrasonic measurement system is a very time consuming operation and any down time of the ISAC is to mitigated to a minimum and clearly justified. Once the technology of ultrasound in conjunction with the ice analogs grown in the small vacuum chamber is proven from which desired results are obtained, the justification for the implementation into the ISAC vacuum chamber is sound.

If porosity can be created in ices with the mobile vacuum chamber, a first impression can be made. Therefore, a porosity with a low accuracy towards cometary ices is considered to be acceptable in this setup. A

current idea is to remove the front window of the vacuum chamber and spray water, enriched with CO_2 (sparkling water) onto the substrate. This might create an ice layer with bubbles in it.

The results of the ultrasonic measurements lead to the longitudinal wave velocity of the ultrasonic signal by applying the procedure described earlier in this chapter. By comparing this velocity with the one from compact ice, a trend might be noticeable that can give an idea about the relation between the difference in speed of sound in porous ices and compact ones compared to their porosity.

3.3.2. With ISAC

The possibility of having ultrasonic experiments with the ISAC will introduce possibilities towards measurements with highly qualitative porous ices with much lower temperatures and more temperature control. Challenging will be the thickness of the ice layer, which is much smaller with ISAC then with the mobile vacuum chamber, to be detectable by the ultrasonic signal. But the porosity can be directly measured with spectroscopy of IR which enables the ultrasonic porosity measurement to be validated. Even though it will be challenging and it can take a while before this kind of experiment can be done, its results will be ground breaking.

3.4. Concluding all results

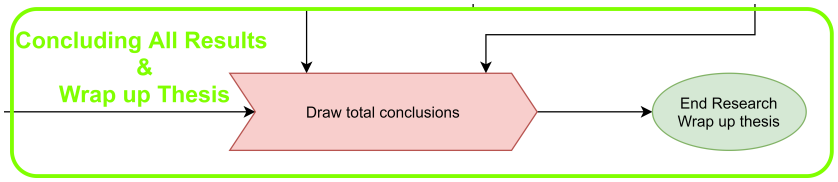


Figure 3.4: All the performed experiments and their findings will provide a conclusion for the project.

Lastly, the results of all experiments and all the work done has to be formulated in a general conclusion. The aim of the project is to estimate porosity with ultrasound, but because of previously mentioned reasons, this is likely to take longer then the extend of my thesis.

4

Numerical simulations of the experimental conditions and experimental results

4.1. Thermal Conductivity Sample Holder with polymethylmethacrylate (PMMA) Substrate

While the sample holder in the vacuum chamber can reach low temperatures close to $\pm 100K$. Since the transducer has an operating minimum temperature of $-20°C$, A methacrylate substrate will be used to provide the thermal separation between the deposition side at the sample holder and the transducer during the experiments in the vacuum chamber because of the low thermal conductivity of the methacrylate. Therefore, simulations should point out what the necessary heat flow would be for the transducer to stay at a temperature higher than $-20°C$ before the start of the experiments. Usually the use of electronic devices poses problems towards cooling when used in a vacuum, but the transducer in this case will be able to use its own heat to stay above the value of minimum operating temperature. Simulations can point out whether the defined length of $20mm$ will be sufficient spacing the methacrylate will provide.

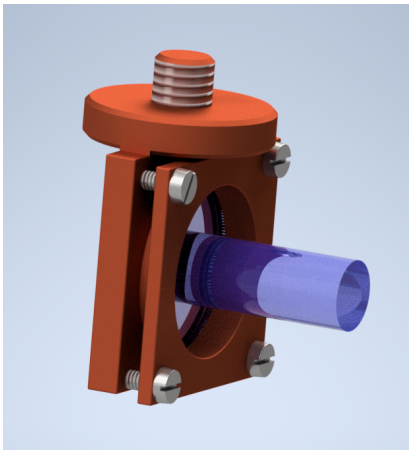


Figure 4.1: Three dimensional assembly of the sample holder.

The simulation software to be used is Comsol Multiphysics 5.4. Since this software allows for assemblies with parts with different materials, the decision was made to make a three dimensional Computer-Aided Design- (CAD-) drawing of the assembly of the sample holder (Figure 4.1) in Autodesk Inventor. To understand how these parts fit together, an exploded view of the sample holder is shown in Figure 4.2.

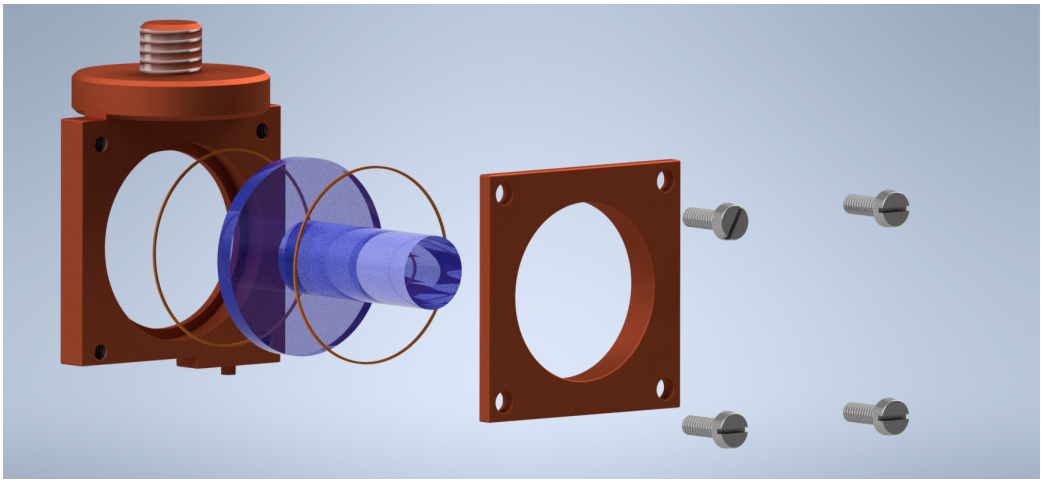


Figure 4.2: Exploded view of the sample holder. The two copper plates can be seen, the methacrylate ("seta") substrate, the two gold rings and the bolts to clamp the methacrylate substrate between the plates.

Once imported into Comsol, the parts are required to have a material. To assign material properties to the parts, the Comsol library was consulted. All materials chosen were generic materials which is assumed to be sufficient for a first order simulation. The generic material properties for PMMA, however, required a specific heat to be inserted manually. This was found to be $1466 J/kgK$ [25].

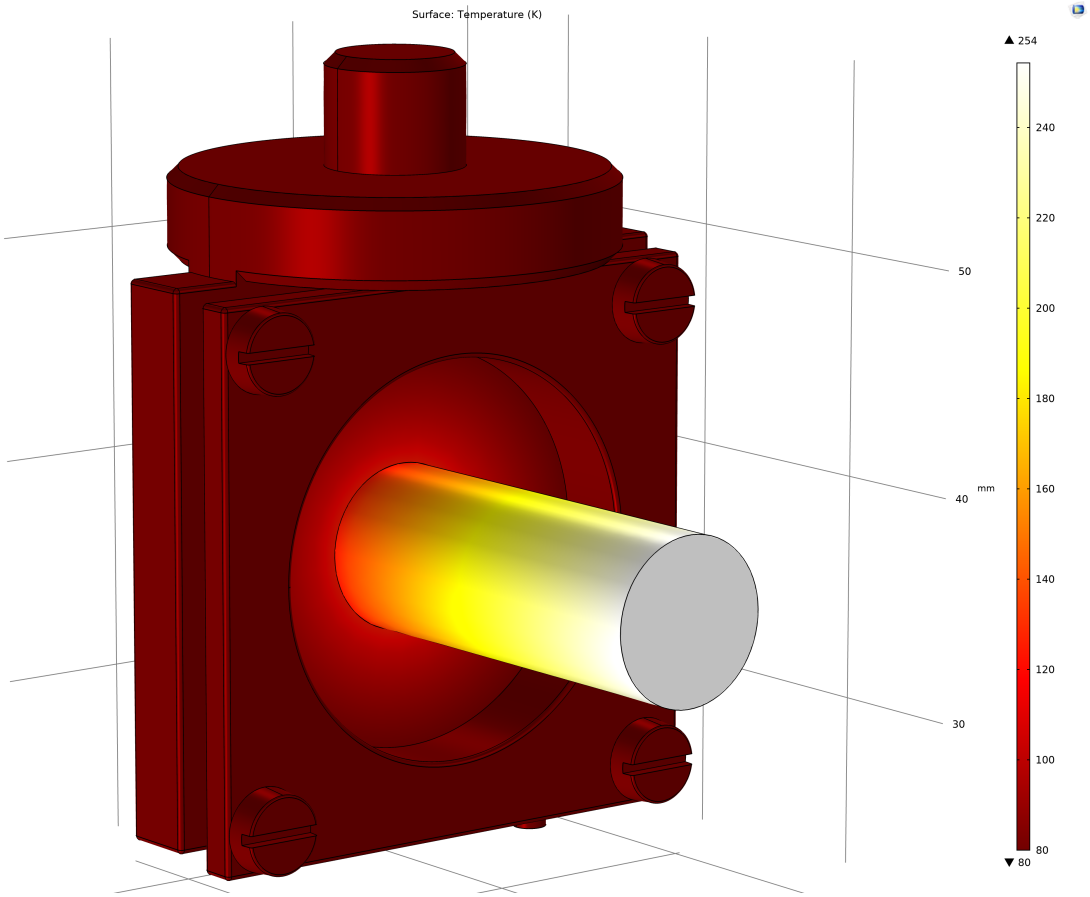


Figure 4.3: Three dimensional view of the thermal distribution when the sample holder with a $1mm$ mesa has reached and equilibrium temperature. When looking at the base, the methacrylate part at the transducer side, it can be seen that the temperature remains high here while the rest of the sample holder has a much lower temperature. The color scale ranges from $80K$ (dark red) to $254K$ (white).

After the material properties were inserted, the type of simulation was chosen. In this case, the most con-

venient type of simulation was one with one reference temperature and a heat flux applied to the *"base"* of the methacrylate substrate. The reference temperature was set to be $80K$ at the surfaces where the coldfinger touches. This includes the top part of the copper cylinder on top of the clamping plates and the surface of the threaded screw on top of it. Values for the heat flow were guessed until the closest temperature near, but stil above, $-20°C$ was measured at the transducer side of the methacrylate.

Initially, there were two different methacrylate substrates. One with a $1mm$ thick *"mesa"* (the flat circular dish) and another one with a $2mm$ thick *"mesa"*. In order to consider both possibilities, separate 3D-drawings, assemblies and simulations were performed. A comparison of their individual performance is presented in Table 4.1. Eventually, the preference went to the methacrylate substrate with a $1mm$ thick *"mesa"* because it has optical advantages towards IR spectroscopy that will be necessary to measure porosity in a later stage of the project.

Figure 4.3 shows a three dimensional view of the temperature distribution of the sample holder with a scale from $80K$ (dark red) to $254K$ (white). The whitest circular surface is where the transducer will be mounted. This is the hottest part of the sample holder as well. From the picture can be concluded that the copper plates of the sample holder conduct the cold very well because their colors are identical. The methacrylate has to encounter the largest thermal gradient. The mesa (the methacrylate disk-part) shows that the methacrylate has almost the same temperature with a large radial distance from its centerline as the copper plates, while the mesa temperature close to the radial distance of the base is significantly higher. This makes the outermost diameters of the mesa want to shrink while the innermost diameters want to expand. Because the mesa's thickness is small, the thermal stresses in this part can become large. The weakest spot is where the mesa and the base come together (at the radial distance of the base).

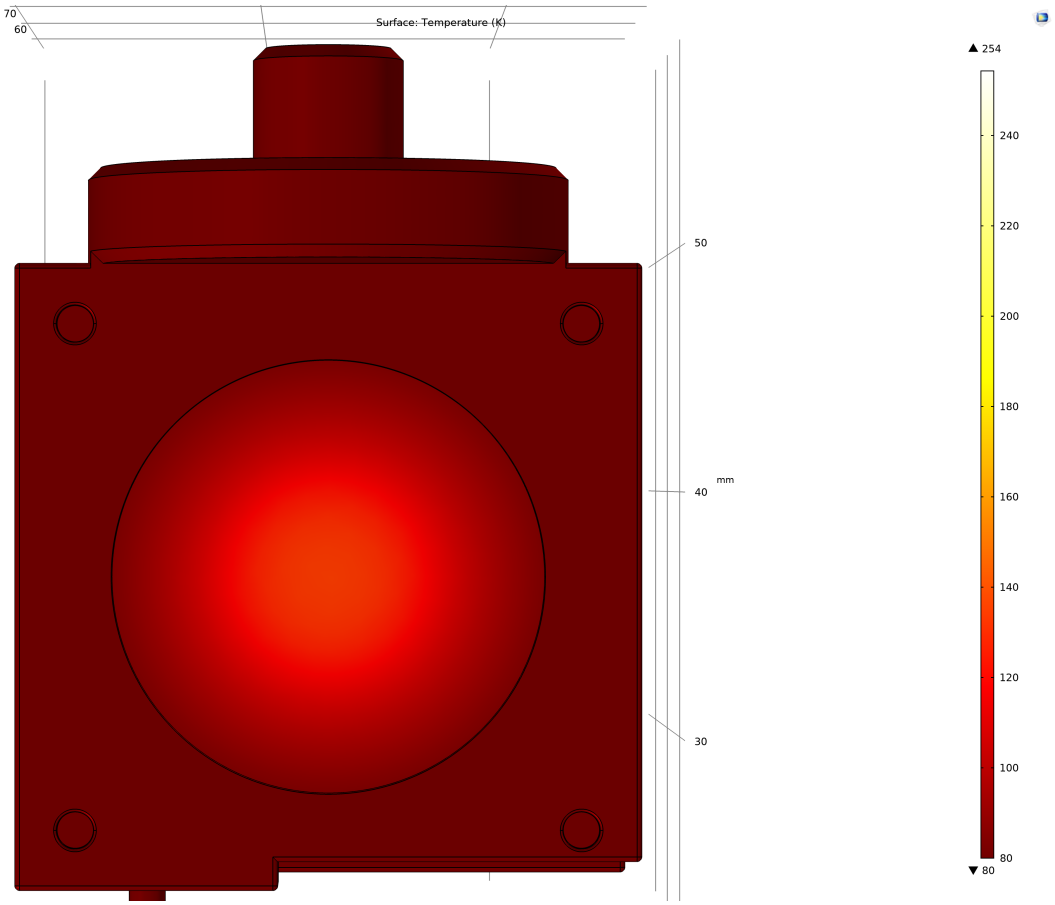


Figure 4.4: Two dimensional view of the deposition side of the methacrylate with a $1mm$ mesa after it has reached an equilibrium temperature.The color scale ranges from $80K$ (dark red) to $254K$ (white).

The temperature gradient in the base itself is also significant, but since the cross-sectional area of this part is much larger, its internal stresses will be significantly lower. Figure 4.4 shows the temperature in the front perspective of the sample holder. Note that the copper plate has a uniform color which means that the temperature of the copper plate is uniformly spreaded throughout the material because of its high thermal conductivity. The methacrylate substrate shows a radial gradient as earlier discussed. The hottest temperature on the mesa lies in its center, which is unfortunate because this is the location of most importance for the ultrasonic measurements since the acoustic waves only measure the in the diameter of the base. Even though the warmest temperature visible in Figure 4.4 is sufficient to freeze water in this vacuum, the colder temperature on the copper will cause most of the ice to grow on the copper plates and at the outer radii of the mesa.

The results produced by the simulations are summarized in Table 4.1. Here the temperature values for the base at the transducer side are presented next to the maximum mesa temperature when a thermal equilibrium is reached. For the condition of thermal equilibrium, the heat flow is listed in milliWatts. Furthermore, the Comsol simulations give more insight by comparing the cool down time. This is the time necessary to cool down the methacrylate mesa. The time at certain moments when the maximum mesa temperatures (located at the center of the mesa) went under certain thresholds (shown in the table) is shown.

With these results can be concluded that the sample holder with a $2mm$ thick mesa can reach lower temperatures at the mesa-side on which will be deposited and despite the fact that it is thicker, so more methacrylate is used, cooling down the methacrylate is more then twice as fast. This is related to a larger contact surface (in the pocket of a copper clamping plate). The thermal gradient also shows to be smoother with a thicker mesa. This is why for the thermal and mechanical properties, the $2mm$ thick mesa is preferred, but the $1mm$ thick mesa is chosen for its superior optical properties during laser porosity measurements.

1mm mesa			**2mm mesa**		
$T_{[transd]}$	254.32	K	$T_{[transd]}$	255.58	K
$Tmax_{[mesa]}$	134.05	K	$Tmax_{[mesa]}$	111.86	K
$P_{[transd]}$	52.00	mW (Thermal Heat)	$P_{[transd]}$	60.00	mW (Thermal Heat)
Time [T<160K]	1230.00	s	Time [T<160K]	520.00	s
	20.50	min		8.67	min
Time [T<150K]	1605.00	s	Time [T<150K]	640.00	s
	26.75	min		10.67	min
Time [T<140K]	2325.00	s	Time [T<140K]	860.00	s
	38.75	min		14.33	min
			Time [T<130K]	1100.00	s
				18.33	min

Table 4.1: The results of the performed simulations are listed in this table for a mesa thickness of 1 & 2 mm. $Tmax_{[mesa]}$ refers to the maximum temperature at the deposition side. Since this is at equilibrium conditions, this will be the lowest temperature at which ultrasonic measurements can take place. Furthermore, the cool down time is calculated. Since this is an exponential curve, it will take very long to reach the equilibrium temperature.

4.2. Ultrasonic Propagation

In order to better understand the wave propagations that are present during the ultrasonic reading in the experiments that will be performed, we will use ultrasonic waves to determine the thickness and characteristics of the ices described in Chapter 6, several simulations were done by dr. Margarita Hernandez. The simulations were made with SimNDT software [26]. This wave propagation simulator performs a parallel implementation via OpenCL of the 2D Elastodynamic Finite Integration Technique (P/SV: 2nd spatial-time order) for Elastic/Viscoelastic media [26]. In this case the inspection setup consists of one transducer (10 mm in diameter) operating in pulse-echo mode and drives a raised cosine signal at 10 MHz. The aim of this set of simulations is to verify and justify the existence and origin of certain features that were observed in the response signal of the ultrasonic pulse.

4.2.1. In Ice Drop

In one type of experiment, a drop of water is placed right on top of a transducer and frozen to check for differences in the ultrasonic response between compact ice and porous ice. From the experimental data can be seen that there is a significant amount of noise at certain timestamps in the echo. The suspicion was that this might be caused by the shape of the drop and the possibility that signals interfere with each other inside the drop.

Since the drops from the experiments have a varying size, simulations were performed for drop heights of 2, 3 and 5 mm. The average height for the ice drops from the experiments was 2.96mm. In Figure 4.5 shows a set of relevant frames from the simulation of ultrasonic waves in a 3mm ice drop. Furthermore, the width of the drop was also set to match the one of the transducer used in the experiments and the geometry was predefined to resemble a drop. The simulation showed that the shape indeed has a significant influence on the acoustic wave propagation. From the top left to the bottom right, the amplitude of the waves is shown by red and yellow colours. The wave propagates from top to bottom in the frames and are reflected when they interact with a surface.

Chronological overview frames:

0.10 μs A longitudinal ultrasonic pulse is transmitted from the transducer, into the drop of ice.

0.57 μs The wavefront encounters the curvature of the drop after which the longitudinal wave will be reflected. These reflections contribute to a horizontal propagation within the drop. The undisturbed part of the longitudinal wave continues to propagate towards the top surface of the drop.

0.75 μs The first horizontal reflected wavefronts meet in the center of the drop and start interfering with each other.

0.94 μs The undisturbed wavefront of the original pulse reaches the surface of the top. Meanwhile, the horizontal wavefronts from the reflections dominate the reading of the transducer. This is the reason why reflective signals are observed in the experiments before the reflection peak coming from the surface of the top of the drop.

1.32 μs The reflection from the top of the drop is travelling towards the transducer.

1.70 μs Impact of the reflection of the ultrasonic signal from the top of the drop onto the transducer. This impact creates the first large peak in in the measured ultrasonic response.

1.79 μs After the impact, this strong signal will be reflected back to the top of the drop.

2.45 μs The reflected signal approaches the surface of the top of the drop again. Once more, disturbing interactions of other pressure waves interact with the transducer.

2.55 μs After this second impact can be seen that the reflected signal encountered significant attenuation by this impact.

2.83 μs Interference of a curved wavefront moving towards a common center point makes the amplitude locally higher, resulting in a dark-red dot in the simulation frame moving towards the transducer now.

3.21 μs Close to the transducer, the wavefront dispersed more which decreased its intensity.

3.30 μs Second impact on the transducer of the reflected wave from the top of the drop. This creates a second, smaller peak.

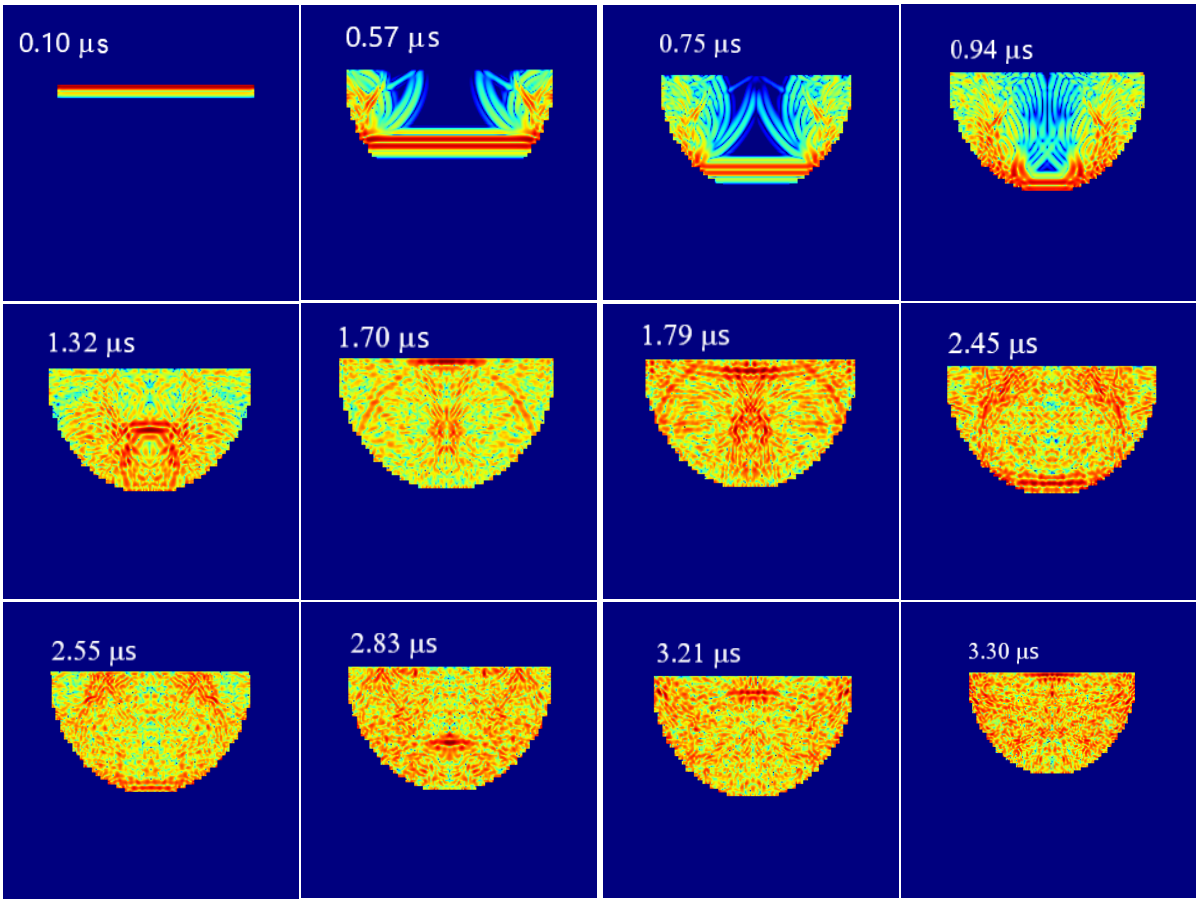


Figure 4.5: Simulated wave propagation in a 3mm ice drop. The transducer that sends and receives the ultrasonic signal is located at the flat surface or the top of the pictures. The amplitude of the Ultrasonic waves is represented by the red and yellow colors. Darker red and yellow represent stronger waves (higher amplitudes). (Credit: Margarita Hernandez)

The simulation entails the ultrasonic reading as seen from the transducer as well, which is presented in Figure 4.6. The time that each frame from Figure 4.5 represents, can be related to the x-axis of this graph. Right after $0\mu s$, the longitudinal pressure wave sent by the transducer can be seen. The first large peak at $1.70\mu s$ can be attributed to the top of the drop. The second large peak at $3.30\mu s$ is a reflection of the first large peak that came from the top of the drop. In between and in front of the first peak, acoustic disturbances are present as a result of the drop's geometry.

Important to clarify is that this simulates a wavefront that covers the entire bottom of the drop. In the experiments the receiver is half of the surface of the transducer. This would make the propagation within the drop look more chaotic because the propagation of the longitudinal waves will have more horizontal movements, but the ToF of the peaks of importance would not change much. The propagation of ultrasound in the drop experiments is further elaborated on in Chapter 5.

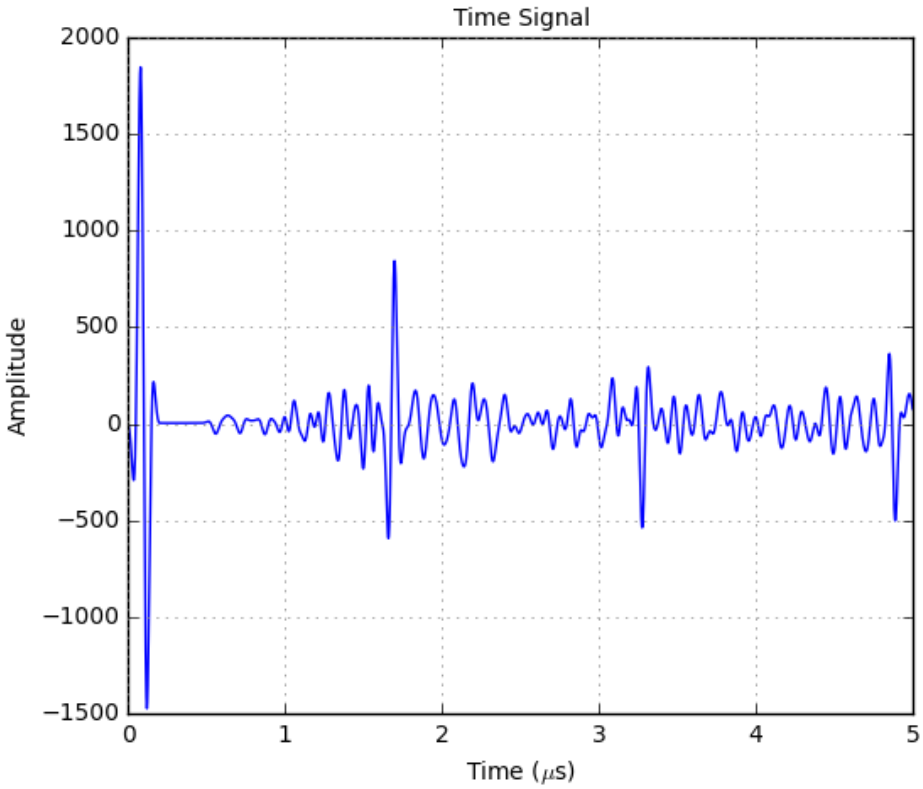


Figure 4.6: Response signal as seen by the transducer from which the pulse originates at the bottom of the drop (the top of the individual frames in Figure 4.5).

4.2.2. In porous ice drop

A similar set of simulations are done for porous ice drops to understand the influence of porosity on the experiments. The simulation creates a cross section of the drop with randomly filled porosity bubbles that have a random radius between $0.01mm$ and $0.1mm$. The drops are filled with bubbles until a certain percentage of surface area is covered by the porosity bubbles. Figure 4.7 has a porosity of 5% and it shows that while the wavefront of the pulse propagates through the drop, the porosity bubbles act as dispersive elements in the drop. By the time the wavefront reaches the top surface of the drop, it already decreased significantly in intensity. It decreases even further since the wave has to travel back to the flat transducer surface.

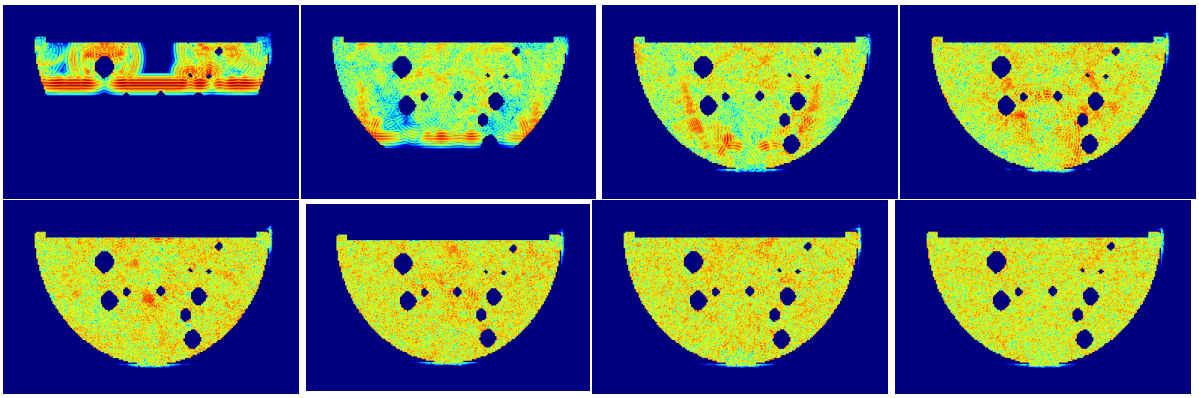


Figure 4.7: Simulated wave propagation in a 3mm porous ice drop. The transducer that sends and receives the ultrasonic signal is located at the flat surface or the top of the pictures. Note the dissipating effects caused by a porosity of 5%. The amplitude of the ultrasonic waves is represented by the red and yellow colors. Darker red and yellow represent stronger waves (higher amplitudes). (Credit: Margarita Hernandez)

By the analysis of the ultrasound readings from the transducer, the plots in Figure 4.8 and in Figure 4.9 were created that show the response in porous ice drops and porous liquid water drops respectively. The left plots in these figures is the simulated response from a drop without porosity that is compared to the corresponding right plots that show a composition of the response with three different levels of porosity. From both of the simulated responses can be seen that the attenuation is very high which makes the detection of the ultrasonic signature of the top of the drop very difficult or even impossible when the porosity is too high. In Figure 4.9 can be seen that for the blue line (5% porosity), the surface is visible in the ultrasound although it is highly damped. The higher the porosity in the bubble gets, the harder it gets to find a distinct peak that comes from the top of the surface of the drop.

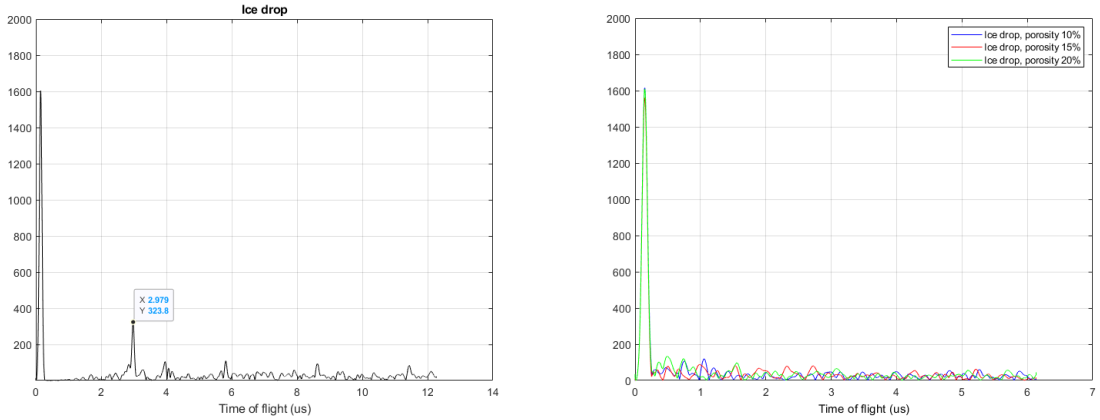


Figure 4.8: Simulated A-scans of the propagation in a 3mm water ice drop. The A-scan on the left is from a drop without porosity. The graph on the right shows the response in the A-scan of drops with 10%, 15% and 20% porosity in blue, red and green respectively. (Credit: Margarita Hernandez)

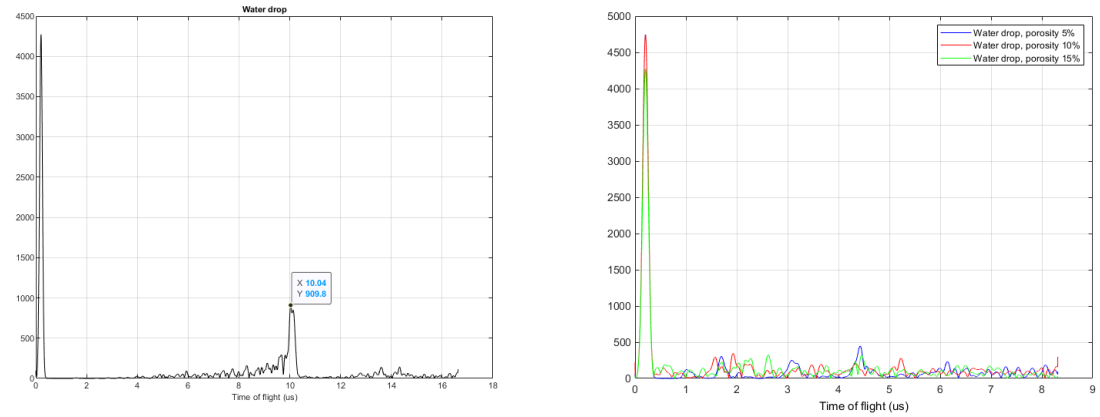


Figure 4.9: Simulated A-scans of the propagation in a 3mm liquid water drop. The A-scan on the left is from a drop without porosity. The graph on the right shows the response in the A-scan of drops with 5%, 10% and 15% porosity in blue, red and green respectively. (Credit: Margarita Hernandez)

4.2.3. In "Seta" + aluminium dish + ice

The "Seta" is a single methacrylate part that consists of a "Mesa", a disk that is connected at its outer edges to the copper plates of the sample holder for cooling down, and a "Base" which is a rod where the ultrasound will travel through that will ensure a thermal barrier between the cold "Mesa" and the transducer that is not supposed to be cooled down that far. In the process of trying to improve the ultrasonic response of the grown ice, several adaptations to the "Seta" were proposed. In one configuration, the good thermal conductivity of aluminium was preferred to grow the ice on while the poor thermal conductivity of the methacrylate would be maintained.

To verify what response was seen in the experiment and to check why the signal of ice is not very noticeable, the simulation of ultrasonic propagation through this configuration was done by dr. Margarita Hernandez. Figure 4.10 shows a set of 20 frames in which the propagation of ultrasound is made visible. When the initial wavefront hits the surface of the aluminium (and later the ice), more frames are shown in order to trace back the origin of the echo-pulses. The frame of 15.2μs shows the alignment of the first set of pulses that will be measured by the transducer. In figure 4.11, this frame is enlarged and the origin of the most important reflected wavefronts is tagged. The same tags are present in Figure 4.12, which shows the received signal as seen by the transducer.

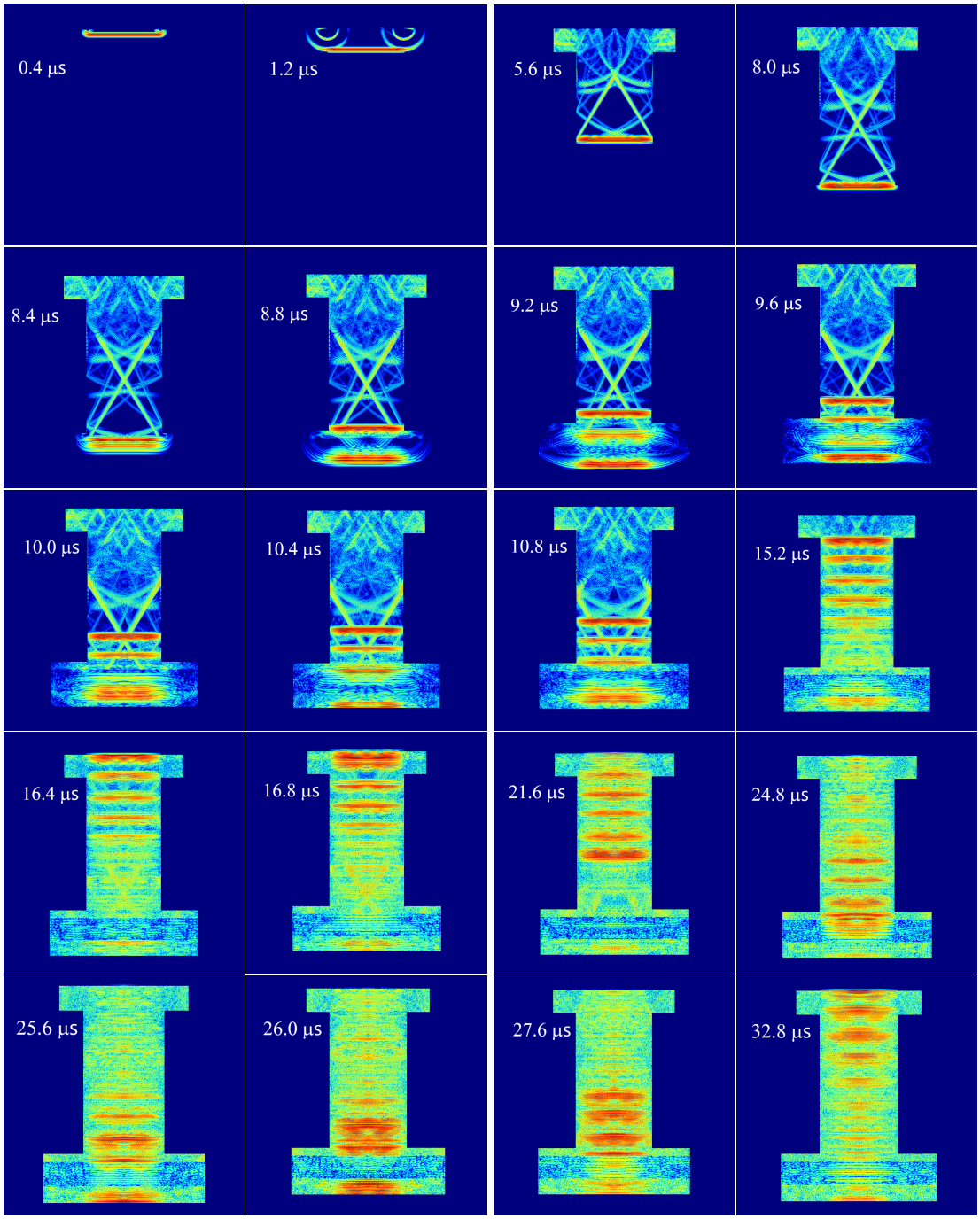


Figure 4.10: Simulated wave propagation in the following configuration: Methacrylate Substrate + 3mm Aluminium layer + 2mm Ice layer. The transducer that sends and receives the ultrasonic signal is located at the flat surface or the top of the pictures. The amplitude of the Ultrasonic waves is represented by the red and yellow colors. Darker red and yellow represent stronger waves (higher amplitudes). (Credit: Margarita Hernandez)

0.4 μs - 8.0 μs The first four frames describe how the sent pulse propagates through the methacrylate.

8.4 μs - 8.8 μs The wavefront reaches the end of the methacrylate and starts propagating through the aluminium while part of the wave will be reflected by this surface. The speed of sound in aluminium is high, which caused the wave to travel through the aluminium in a short time after which the wave will start travelling through the ice layer.

9.2 μs - 15.2 μs The wavefront reaches the end surface of the ice after which it will reflect a signal back. The speed of sound in ice is slower than in aluminium which causes two reflections of the aluminium-ice interface to run through the methacrylate before the signal of the end of the ice surface starts running through it. Eventually, a pulse-'train' of signals and reflections will propagate through the "Seta".

16.4 μs - 21.6 μs The 'train' of pulses will run to the transducer in order to be measure its peaks. Once again, all signals are reflected back towards the aluminium and ice layer.

24.8 μs - 27.6 μs All ultrasonic signals go through all the surfaces again, creating a series of reflections. The reflections of these surfaces overlap with incoming waves which makes it quiet impossible to keep track of the origin of the reflections.

32.8 μs At this Time of Flight (ToF), the second set of echoes from the sent pulse will be received.

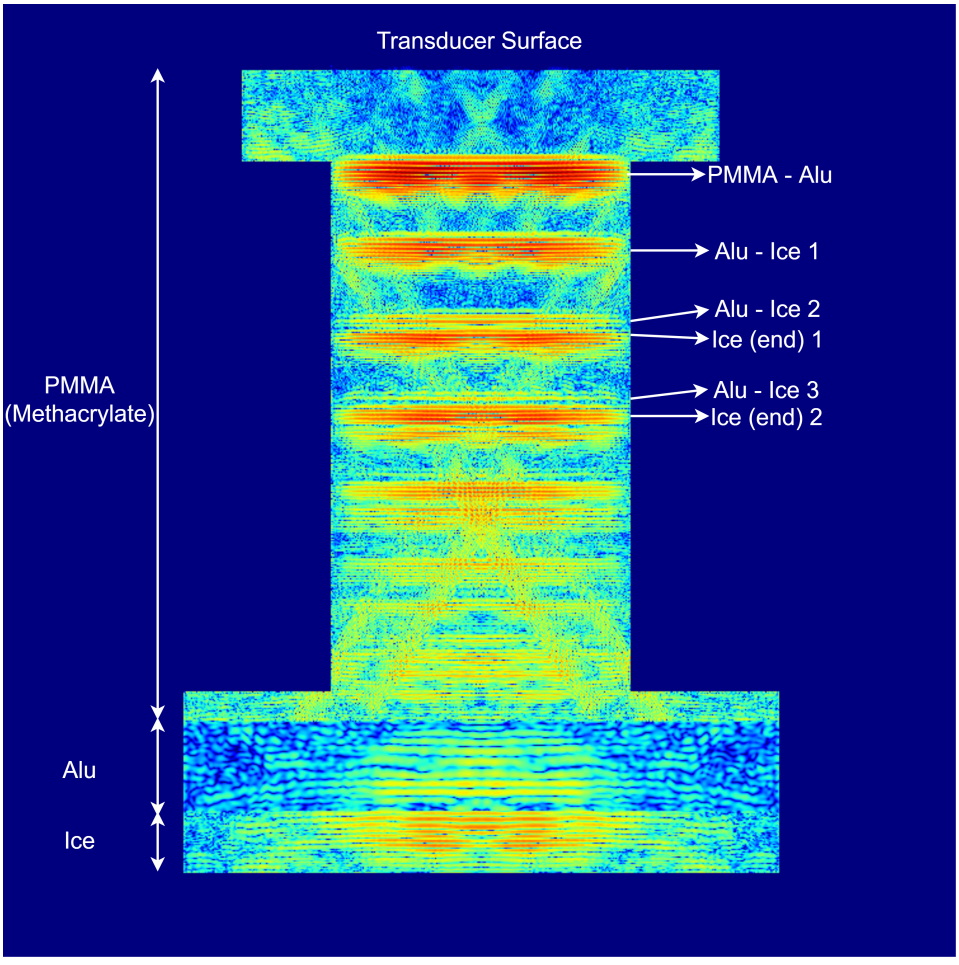


Figure 4.11: Frame at 15.2μs from Figure 4.10 shows the sequence of pulses that will be received by the transducer. The wavefronts visible are moving upwards and are tagged with the boundary transition they represent. Note that the second reflection of the aluminium will reach the transducer before the signal of the end surface of the ice.

The origin of the wavefronts is shown in Figure 4.11 and Figure 4.12. The signal from the end surface of the ice is hardly distinguishable from the one of the aluminium - ice interface. This shows the the ice thickness

is difficult to measure with such a setup, since the reflection due to the aluminium is difficult to disentangle from the refection due to ice.

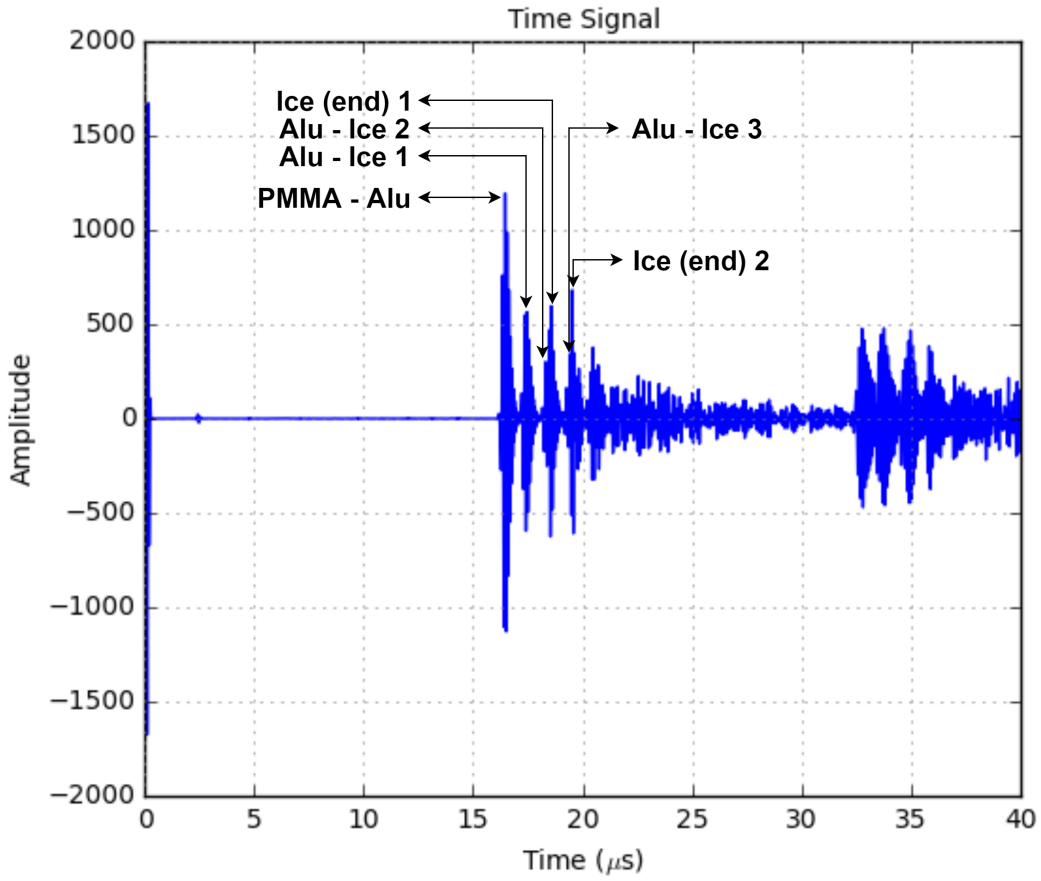


Figure 4.12: Received ultrasonic signal from the simulated situation in Figure 4.10. The reflection of the signal by the aluminium dish is visible and makes it hard to notice the grown ice.

5

Ice Drop Experiments and Results

To gain insight into the influence of porosity in ice on ultrasonic measurements in a fast and direct manner, it is chosen to freeze drops of water directly on a transducer. The normal (compact) ice drops were made with regular water while porous ice drops were made using sparkling water. In addition, alternative ice drops were created to emphasize the influence of different liquids and mixtures on the quick ($\pm 40 min$) experimental procedure allowed for a number of 52 drop experiments.

5.1. Compact Ice Drops

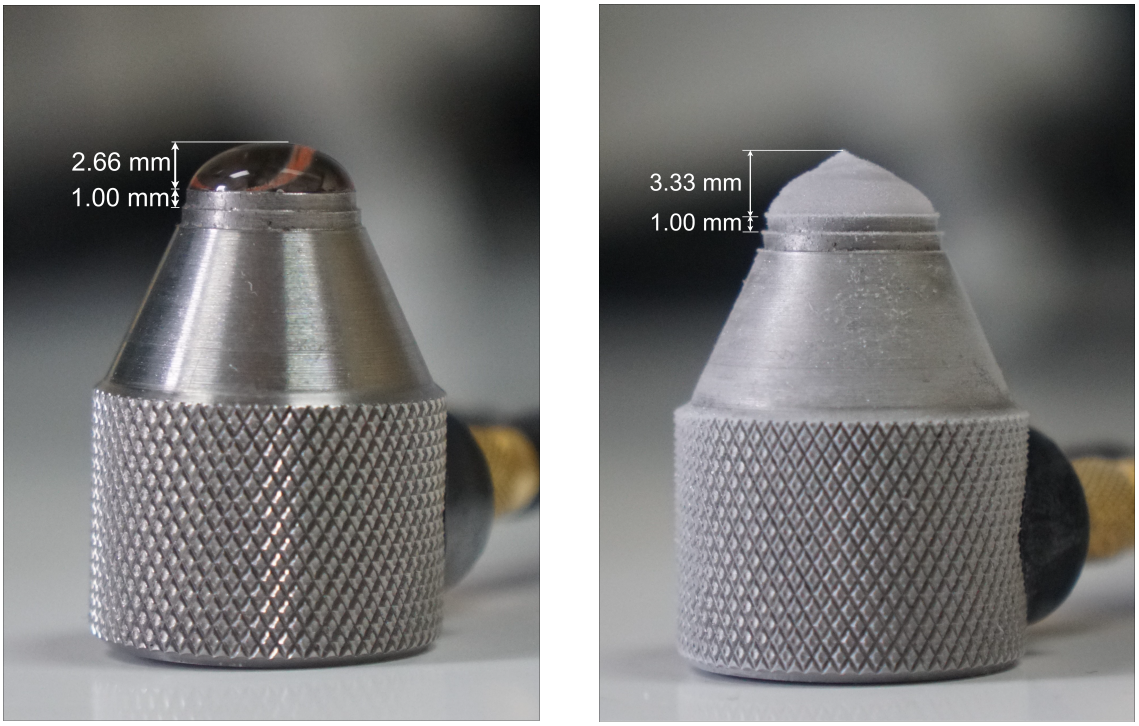


Figure 5.1: Optical determination of drop height from a liquid drop and from a frozen drop. The dimensions of the transducer were carefully measured so that its geometry could be used to subtract the dimensions of the drops. The pictures shown were taken from Ice Drop Experiment 45.

The first set of experiments are performed with "compact" water. This refers to the freezing of liquid water, which makes non porous ices, at the difference with the freezing of sparkling water making a porous ice (Section 5.2). Obtaining the speed of sound in these drops is done by optically determining the height of each drop and the Time of Flight (ToF), which is the time between the sent ultrasonic pulse and the received pulse, from the ultrasonic data. The optical height determination is done by analyzing images that were taken during the experiment (see Figure 5.1) and comparing the dimensions of the drop with the dimensions of the transducer that were carefully measured beforehand and considered to remain constant for all experiments.

Performing such estimates for the water drop of Drop Experiment 45, the found drop height is $2.66mm$ for liquid water and $3.33mm$ for ice. When the drop is put inside the freezer, it cools down from room temperature (R.T.) to freezing temperatures but the height of the drop is assumed to stay constant ($2.66mm$) for its liquid phase (between R.T. and 0°C). When mentioning these temperatures, it is important to understand that no temperature sensor is used to directly verify this. "R.T." is the actual room temperature which varied for every drop experiment. To find the peaks originating from the top surface of the drops, Amplitude-, or A-scans (see Figure 5.2) are made from the ultrasonic data. The A-scan figures show the amplitude of the ultrasonic response as a function of the ToF. The A-scans that refer to water at 0°C are from drops in the freezer at the moment before they froze. This moment is visible in the ultrasonic A-scans for which the last meaningful scan of the drop (before the response drops: see Section 5.5.1) can be considered as from liquid water at a freezing point temperature. Finally, the $-18°C$ is the freezer temperature and the drop is assumed to have the same temperature when it is frozen.

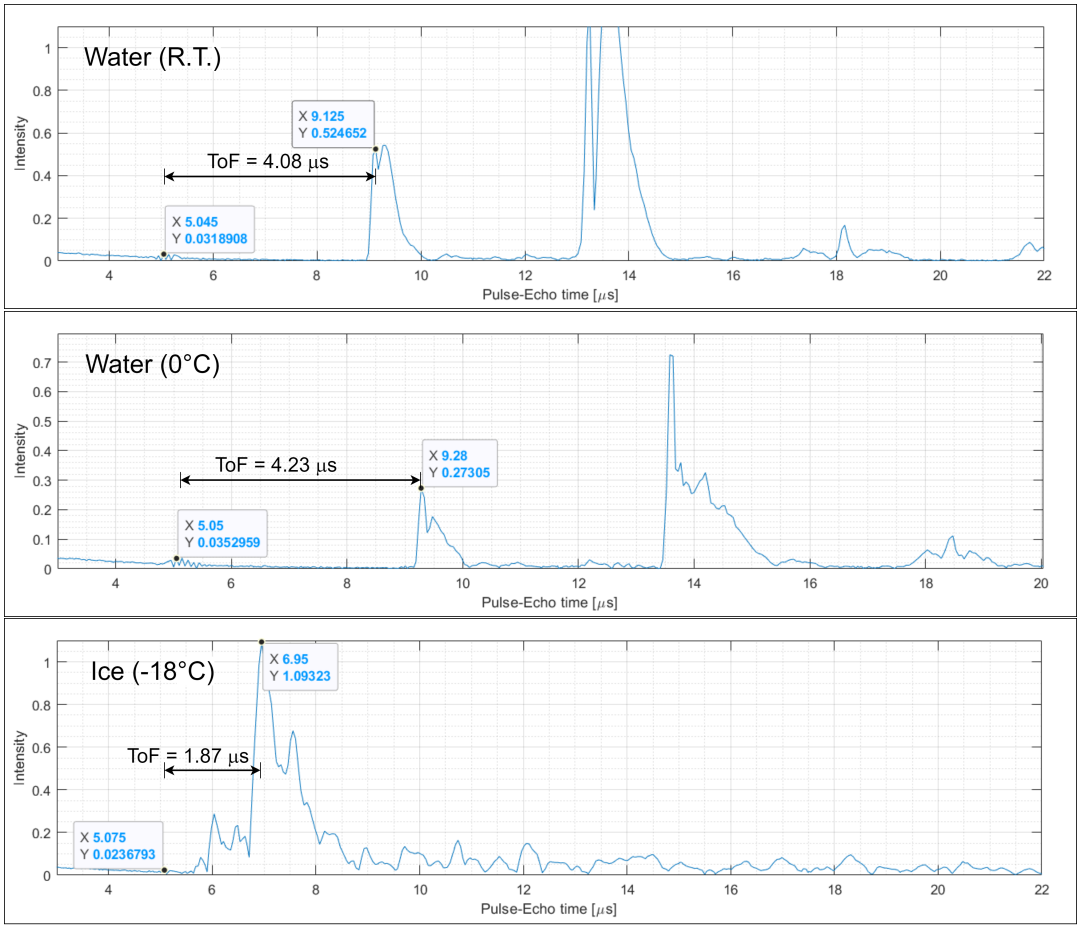


Figure 5.2: Typical set of A-scans for Drop Experiment 48. For 3 different temperature values, the ToF between the first arriving longitudinal reflected wavefronts of the surface of the transducer and the top surface of the drop is subtracted and displayed in the respective graphs. This value is used to calculate the speed of sound in the drops.

The ToF related to the height of the drop is subtracted from the ultrasonic data by the time difference between the surface of the transducer and the first peak that is observed. Generally, the peaks generated by compact ice are steep and obvious to select, making the determination of the ToF for these type of drops straight forward. Figure 5.2 shows the A-scans for a typical experiment with compact ice. Because of the large difference in speed of sound in liquid water and ice, the peak shifts close to the (relatively static) bump of the surface of the transducer when the water freezes. When taking a look at the top picture of Figure 5.2 that resembles the drop of liquid water at R.T. can be seen that the first large peak at roughly $9\mu s$ is the first reflection coming from the top of the drop. The second one, at roughly $13\mu s$ is a second reflection. It being larger than the first one is a consequence of the semi spherical shape of the drop and the fact that the transmitting and receiving parts in the transducer are separated.

For Experiment 48, the ultrasonic ToF of Figure 5.2 is used with its drop height referred to as h in the equations, $2.99mm$ and $3.58mm$ for liquid water and ice respectively to calculate the speed of sound shown in the following equations:

$$c_{R.T.} = \frac{2h}{ToF} = 2\frac{2.99\cdot10^{-3}m}{4.08\cdot10^{-6}s} = 1465.69m/s \tag{5.1}$$

$$c_{0°C} = \frac{2h}{ToF} = 2\frac{2.99\cdot10^{-3}m}{4.23\cdot10^{-6}s} = 1413.71m/s \tag{5.2}$$

$$c_{-18°C} = \frac{2h}{ToF} = 2\frac{3.58\cdot10^{-3}m}{1.87\cdot10^{-6}s} = 3828.88m/s \tag{5.3}$$

Comparison drop experiment 48 with literature

When these values are compared with literature values in Table 5.1, it becomes clear that this experimental procedure has a performance that has deviations less then ±2% for any temperature regime.

	$c_{R.T.}$	$c_{0°C}$	$c_{-18°C}$
Experimental [m/s]	1465.69	1413.71	3828.88
Literature [m/s]	1481.00	1403.00	3888.50
Difference [m/s]	15.31	-10.71	59.62
Difference [%]	1.03	-0.76	1.53

Table 5.1: Results of drop experiment 48 compared with literature values. Differences are given in m/s and in %.

Statistical results compact ice

The results of a single experiment are good to get a first impression, but reproducibility is important and the simplicity of the setup and the short experimental times allow for a high number of potential experiments that could be done. 52 drop experiments were performed, from which 22 with compact ice (see Appendix B). Not all of them had readable ToF's and with some of them, cracks in the ice made the ultrasonic signal disappear. This is why a lower number of experimental data could be used for statistics.

	$c_{R.T.}$	$c_{0°C}$	$c_{-18°C}$
# of useful experiments	18	8	8
Literature [m/s]	1481.00	1403.00	3888.50
Mean Experimens [m/s]	1477.55	1454.47	3922.25
SD Experiments [m/s]	104.18	62.20	151.28
SD Experiments [%]	7.05	4.28	3.86
Difference [m/s]	3.45	-51.47	-33.75
Difference [%]	0.23	-3.67	-0.87

Table 5.2: Results of all drop experiments compared with literature values. The mean values and the standard deviations (SD) are included. Differences are given in m/s and in %. Note that the speed of sound is calculated for $0°C$ using the assumption that the drop height would be the same as for R.T. The accuracy of the height measurements of the drops is better then $\pm0.09596mm$.

The results from the table project the relevance of having a large dataset of experiments. Because even though the standard deviation can be up to 7.05%, the difference between the mean of the drop experiments

at R.T. and the literature value is only 0.23%. The "high" difference for the ultrasound measured in water at 0°C could have been caused by the fact that no temperature sensor is used to get the temperature of the drop (it is an estimate with $\pm 5°C$) and the drop height that would be smaller compared to the R.T. height of the drop. Nonetheless, the performance of this experimental testing procedure is satisfying concerning the simplistic setup.

5.2. Porous Ice Drops

The research focuses on how the porosity in water affects the propagation of ultrasound. To make water ice porous under atmospheric conditions, sparkling water is used. The molar mass of the compounds in the mixture (water+CO_2) that was found in the bottle is 51.58 mol of water and 2.92 mol of CO_2 that corresponds to $928.4g$ of water with $128.4g$ of CO_2. The bubbles that are created by the sparkling water increase the attenuation of the ultrasonic signals significantly. This makes it harder to determine which peak from the ultrasonic A-scans comes from the surface on the top of the drop. The procedure used to select such peak is elaborated on by means of two examples: Drop Experiment 44 & Drop Experiment 46. These two were chosen because they show clear differences between each other as well as with the compact ice.

Drop Experiment 44

For these type of experiments, the determination of the drop height is done in the same manner as for the drops with compact ice. The left and middle image of Figure 5.3 shows the height measurement for the liquid and the frozen drop. While comparing the ice drop of the middle image to the one of the ice in Figure 5.1 for compact ice, the difference in the shape of the frozen drop stands out. While the drop for compact ice had rounder edges in general, the frozen drop for porous ice often tends more towards a conical shape. This is immediately correlated to the path the ultrasonic wave will travel. In addition, the ultrasonic wave will be obstructed by the bubbles that are frozen. The picture on the right of Figure 5.3 is taken after the frozen drop melted. It becomes immediately clear that the molten drop has fewer and smaller bubbles than present in its liquid phase prior to freezing. This rises the hypothesis that the drop might squeeze out part of the bubbles when the freezing of the drop starts. The figure of the molten drop also provides a top view of the transducer used in these experiments. Here can be seen clearly that the transducer contains two piezo-electric crystals that are used independently as a respective pulser and receiver.

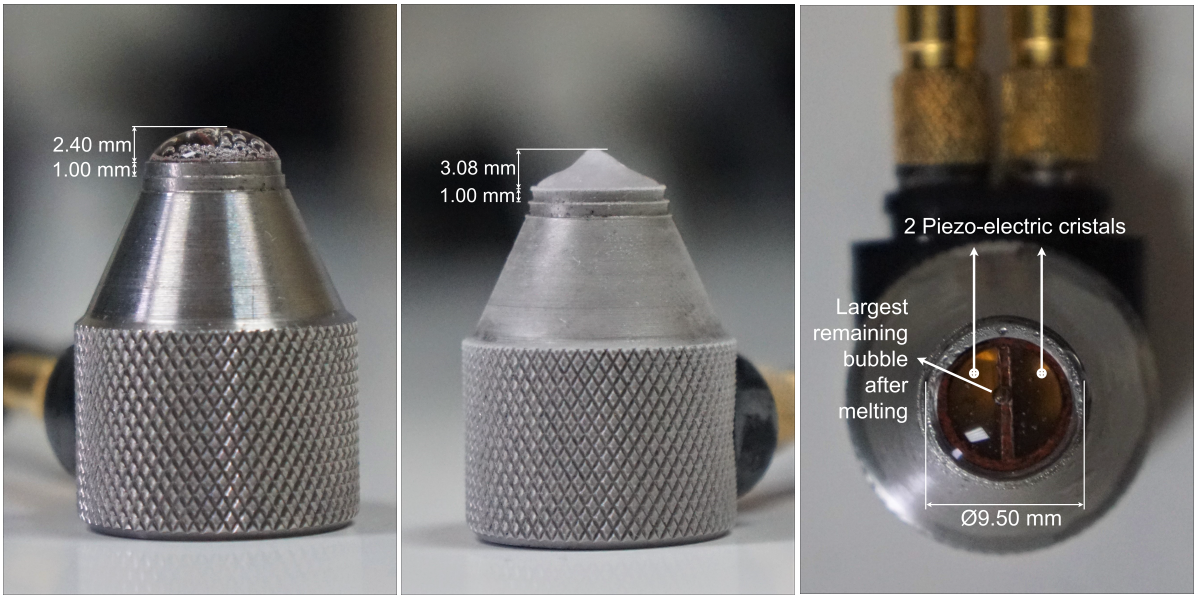


Figure 5.3: Optical determination of drop height at room temperature (left panel), as a frozen drop (middle panel) and after the drop melted (right panel). This set of images reveals the difference in porosity before and after freezing (comparing the left and the right panels). The pictures shown were taken from Ice Drop Experiment 44.

From the ultrasonic data, the A-scans were analyzed. The reflected signals exhibit peaks that look different than in the case of the compact ice drops. The intensity of the peaks dropped and the amplitude of the noise and intermediate reflections that originate from the bubbles increased. In the case of the experiments

with compact water, the top surface of the drop can be identified as the first peak that appears in these plots, but when comparing the ToF in the experiments with bubbles of the first peak to the one expected from the literature, one could see that the first peak usually is located before the literature value.

For experiment 44, the procedure of defining the top of water and ice drop is clarified by the graphs in Figure 5.4. Every A-scan has shown as 2 boxes where the bump from the transducer surface and the peak representing the top surface of the drop are reported. The left one comes from the surface between the transducer and the water or ice. The other one is the estimated peak that resembles the top of the drop. The expected ToF for compact ice ($ToF_{(no-bubbles)}$) is shown as the dark green dashed line in the graph. The speed of sound in porous water or ice is slower in bubble water and ice, causing the peak of the top surface of the drop to be behind the green dashed line. This is why any peak on the left of the green dotted boundary can be considered a consequence of the bubbles that are present in the drop. The signature of the bubbles is pointed at by the red circle in these A-scans. The two lighter green dashed lines are the positions in the graph for which the theoretical literature ToF of a compact drop is 25% and 50% more.

Following the analogy applied on the compact ice drops in Equations 5.1, 5.2 and 5.3, the speed of sound for the drop can be found. This results in $c_{R.T.} = 1352.11 m/s$, $c_{0°C} = 1347.35$ and $c_{-18°C} = 3468.96 m/s$ for the two liquid water drops with different temperature and the ice drop. This corresponds to 91.30%, 96.03% and 89.21% of the speed of sound with respect to water without bubbles at room temperature, at 0°C and to ice of -18°C respectively.

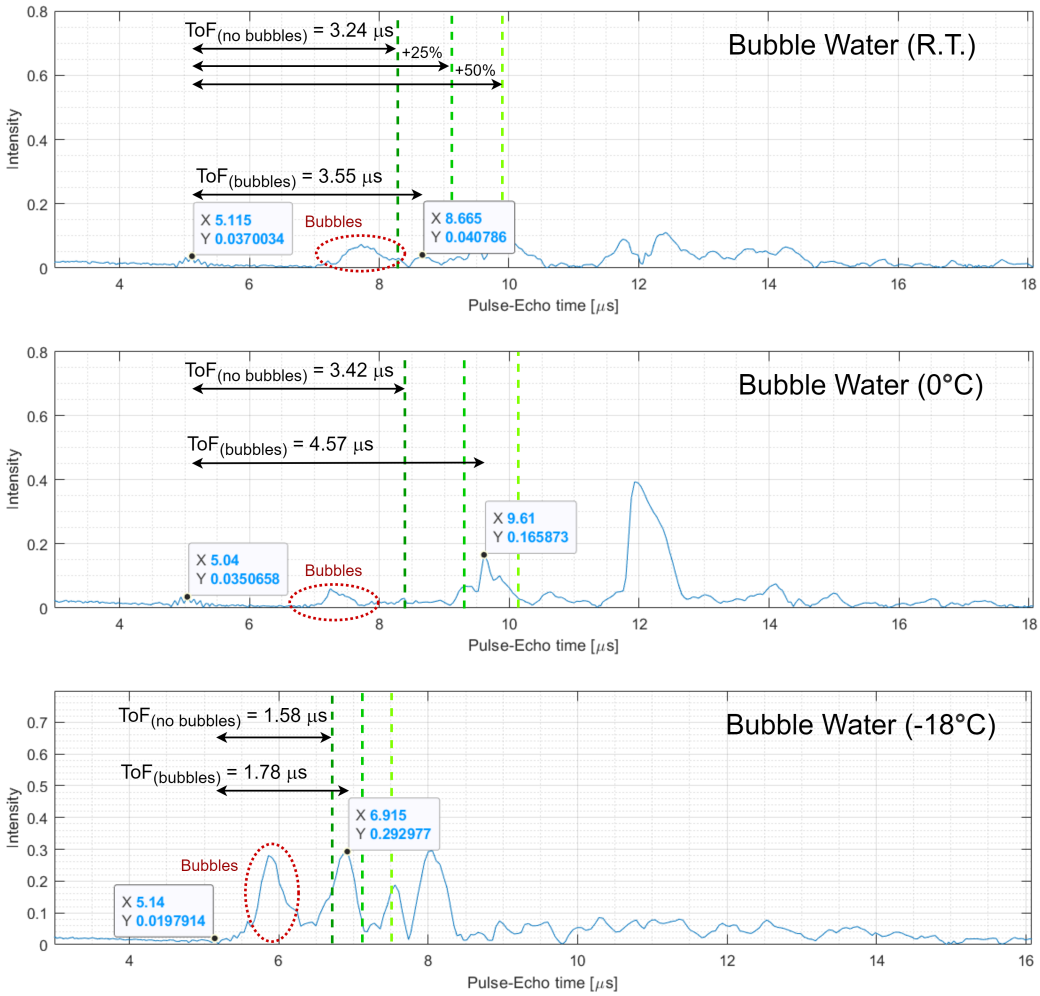


Figure 5.4: Typical set of A-scans for Drop Experiment 44. For 3 different temperature values, the ToF of the hypothetical compact ice (without bubbles) is drawn as the dark green dotted line. The other green dotted lines indicate lines of 25% and 50% beyond this time of flight. The ToF of the top of the porous drop is labelled as $ToF_{(bubbles)}$. The peaks that likely indicate bubbles are shown in the red dotted circles.

Drop Experiment 46

A second porous ice drop experiment is discussed to highlight differences between A-scans. For the compact ice drop experiments, all experiments showed similar, predictable behaviour in their measured ultrasonic response, the porous ice drop experiments show less consistency and a higher unpredictability. Similar to the previously discussed experiments, the determination of the drop height can be seen in Figure 5.5 and the set of A-scans are presented in Figure 5.6.

The graphs in Figure 5.6 are provided with marks on the points of interest and corresponding ToF's. The suspected signature of bubbles in the ultrasound is marked with red circles. When comparing the A-scan at room temperature with the one at 0°C, one can see that a new bubble has grown during the cool-down of the drop while the reflected signal moves to the rights with respect to the expected position obtained from literature values compact drop (the green vertical lines). This indicates that the drop would have grown in the freezer for which the height measurement of the liquid drop in Figure 5.5 is no more valid. The determination of the height of the ice drop is found to be a better estimate of the real height of the drop at 0°C. Therefore, the measurement performance of the liquid drop at freezing temperature should be considered lower than the others.

Selecting which peaks from the ToF corresponds to the surface of the top of the drop is a difficult procedure. The freedom of the bubbles in the water drops cause the ultrasonic peaks to change in intensity and ToF over time, which is why a single A-scan frame can not provide enough information to derive the ToF of the height of the drop. The ones selected in the graphs were found to be the best estimates after analyzing how peaks propagate over time for the entire duration of the experiment.

After determination of the drop height and its corresponding ToF, the estimated speed of sound can be found as calculated in Equations 5.1, 5.2 and 5.3. This results in $c_{R.T.} = 1358.84 m/s$, $c_{0°C} = 1247.47$ and $c_{-18°C} = 3667.41 m/s$ for the two liquid water drops with different temperature and the ice drop. This corresponds to 91.75%, 88.91% and 94.31% of the speed of sound with respect to water without bubbles at room temperature, at 0°C and to ice of -18°C respectively.

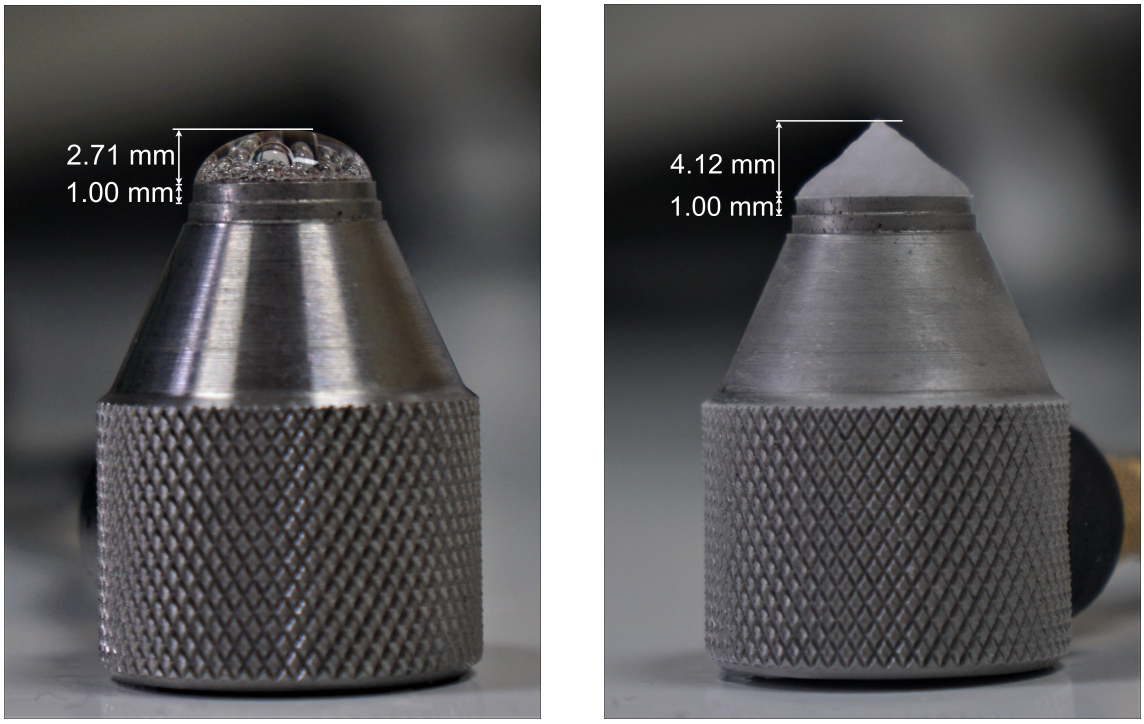


Figure 5.5: Optical determination of drop height at room temperature and as a frozen drop. The pictures shown were taken from Ice Drop Experiment 46.

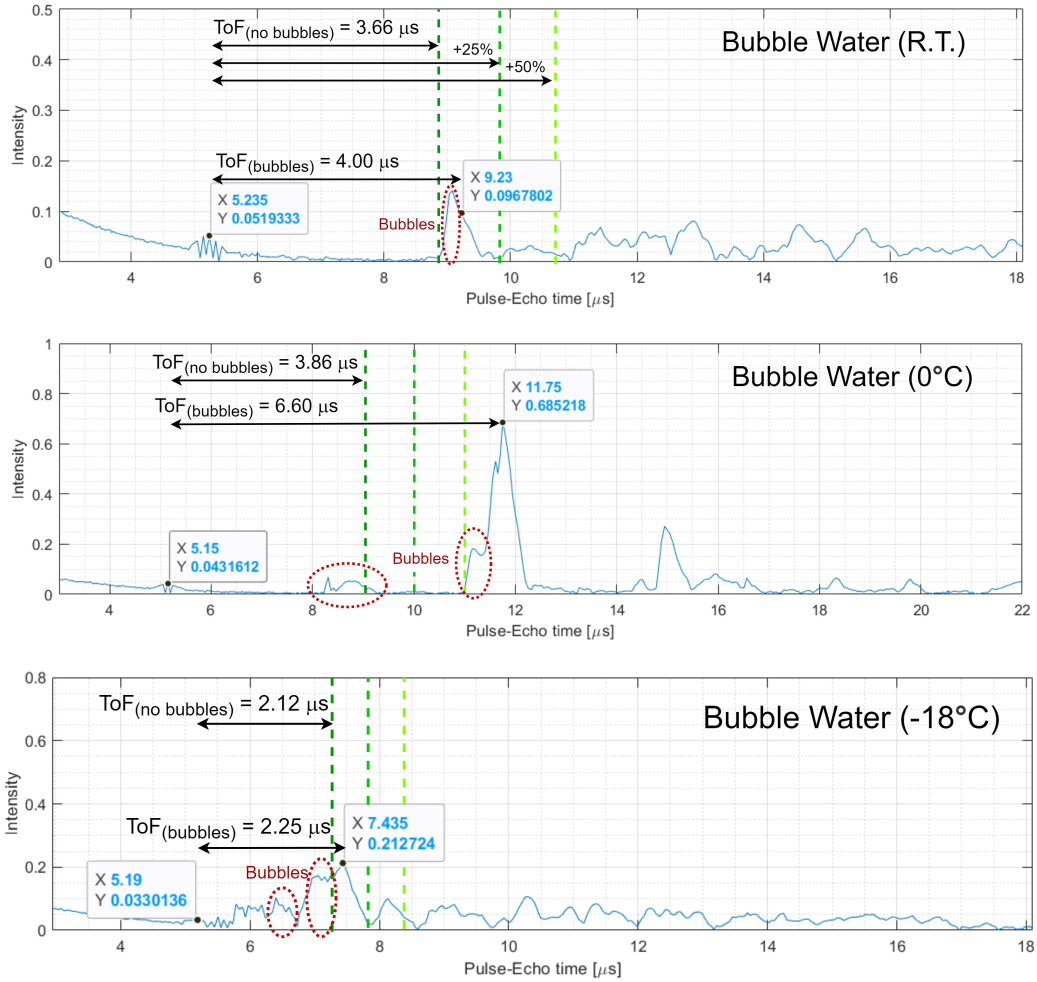


Figure 5.6: Typical set of A-scans for Drop Experiment 46. For 3 different temperature values, the ToF of the hypothetical compact ice (without bubbles) is drawn as the dark green dotted line. The other green dotted lines indicate lines of 25% and 50% beyond this time of flight. The ToF of the top of the porous drop is labelled as $ToF_{(bubbles)}$. The peaks that likely indicate bubbles are shown in the red dotted circles.

Statistical results porous ice

A number of experiments were performed with porous ice to increase its reliability. The statistical outcome of all porous drop experiments are summarized in Table 5.3. The individual outcome of every experiment is listed in Appendix B. From this appendix, the mean values with their standard deviations are shown in the table from which can be seen that the average speed of sound for these type of experiments is slightly lower then the literature values for compact water.

	$c_{R.T.}$	$c_{0°C}$	$c_{-18°C}$
# of useful experiments	13	20	19
Compact Lit. [m/s]	1481.00	1403.00	3888.50
Mean Experiments [m/s]	1343.84	1299.97	3435.99
SD Experiments [m/s]	123.59	145.29	376.58
SD Experiments [%]	9.20	11.18	10.96
Difference [m/s]	137.16	103.03	452.51
Difference [%]	9.26	7.34	11.64

Table 5.3: Results of all porous drop experiments compared with literature values. The mean values and the standard deviations (SD) are included. Differences are given in m/s and in %.

5.3. Compact vs porous ice drop experiments

When comparing the results of experiments of compact drops with porous drop, it can be noticed that the average speed of sound in porous drops is lower than for compact drops. Unfortunately, the difference is not large enough to be able to distinguish a compact drop from a porous one by its measured speed of sound. In Figure 5.7 a scatter plot can be seen for all relevant experiments with compact and bubble water. From these figures can be seen that the spread of the porous ice drop experiments overlaps with the compact ice drop experiments.

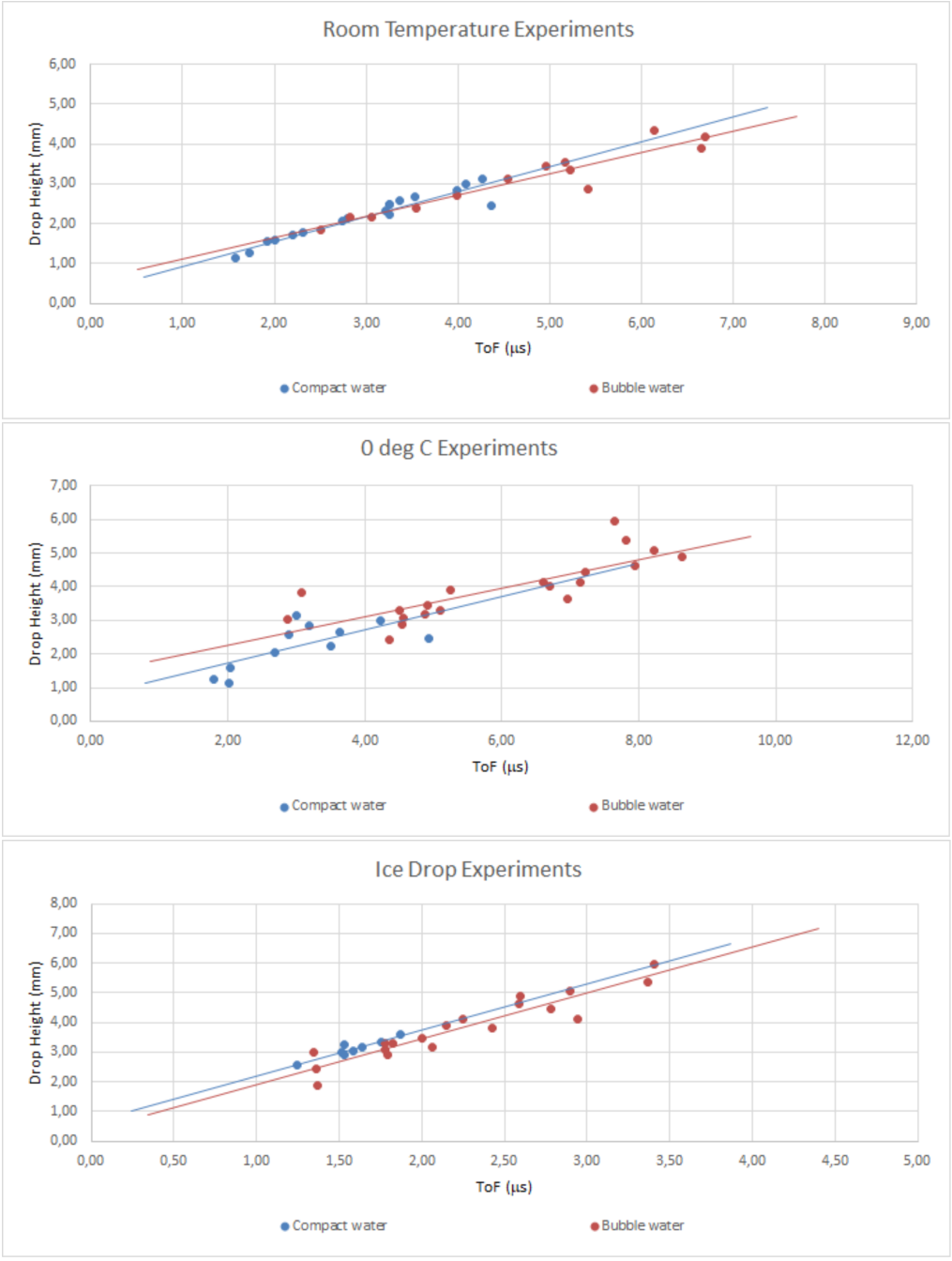


Figure 5.7: Scatter plots with trend lines of experiments with compact and bubble water (blue: compact water; red: bubble water). The Y-axis is the height of the drop; The X-axis is the ToF of the ultrasonic signal. Note that this ToF is the derived ToF from the ultrasonic A-scans, so it travels twice the distance of the height of the drop in this time.

Going deeper into the differences of porous drop with respect to compact drops, one can notice that the bubbles in the drops allowed for larger drops to be placed on the transducer. Together with the fact that the speed of sound is lower in porous drops, this means that the porous experiments will result higher (larger drop height) and more to the right (larger distance to be covered with lower speed of sound: larger ToF's).

When comparing the statistical numbers side by side in Table 5.4, it becomes clear that the standard deviation is much higher for porous drops. From the average speed of sound for both types, it is interesting to notice that their difference increases when the temperature decreases from 9.05% at room temperature to 12.4% for the frozen drop.

		$c_{R.T.}$	$c_{0°C}$	$c_{-18°C}$
Compact Ice Drop	Mean [m/s]	1477.55	1454.47	3922.25
	SD [m/s]	104.18	62.20	151.28
	SD [%]	7.05	4.28	3.86
Porous Ice Drop	Mean [m/s]	1343.84	1299.97	3435.99
	SD [m/s]	123.59	145.29	376.58
	SD [%]	9.20	11.18	10.96
Difference	Mean [m/s]	133.71	154.5	486.26
	Mean [%]	9.05	10.62	12.40

Table 5.4: Summary of statistical values of the speed of sound derived from the compact drop experiments and the porous drop experiments. The comparison entails absolute values (in m/s) and values in percentage.

5.4. Alternative Ice Drops

Because of the quick nature of the experiments, time and opportunity arose to divert the research into ultrasonic propagation in other substances. The purpose of this is to understand in which manner certain elements (mixture or bubbles) influence the ultrasonic propagation. A lower number of experiments were done with these substances because they were not the main focus. This means that the outcome of the results is not as accurate as the water drop experiments.

5.4.1. Bubble-free sparkling water

Experiment 20 was performed with a drop from the bottle of sparkling water. The water was poured out of the bottle after which the gas could escape the water. It rested overnight to make sure that as much gas could escape as possible. The water did not contain any more bubbles when it was placed on the transducer. The ultrasonic waves propagated in a very similar way than in as in water without bubbles.

The drop placed on the transducer had a smaller diameter than the transducer itself. By manually placing the drop in the freezer, the shape of the drop changed which caused the bottom of the drop to have the same diameter as the transducer. Because of this the height of the drop decreased. Since the image of the drop taken has a larger height than the one the ultrasound reports, the calculations of the speed of sound is not considered valid. The measurements for the ice drop were acceptable to take into account.

The found ultrasonic velocity for bubble-free sparkling water ice at $-18°C$ is $4273.45 m/s$. This corresponds to $837.46 m/s$ or 19.60% higher than the average of the speed of sound of the porous ice drop experiments and $351.20 m/s$ or 8.22% higher than the average speed of sound of the compact ice drop experiments. This concludes that the drop of sparkling water, used for the porous drop experiments, can be categorized as a "compact" drop when the drop is free of bubbles.

Since this has been a single experiment, it is hard to conclude whether or not the composition of the drop is the reason for the high speed of sound in ice. More certainty can be achieved with a higher number of these type of experiments.

5.4.2. Beer

Some experiments were done with beer since it is a mixture of water, ethanol and carbohydrates such as sugar and it was convenient to use. Furthermore, the size of the bubbles that originated from the beer were different. This made it possible to study the influence of different bubble sizes on the ultrasonic propagation. Two different beers were used during the experiments: Alcohol free beer (Carrefour) and Karmeliet.

Alcohol free beer

Compared to Karmeliet, the mixture of alcohol free beer contains carbohydrates ($4.7g/100ml$) with a higher amount of sugars ($2.6g/100ml$) and its bubbles are slightly larger. Two experiments were done with this beer drop at room temperature and at $0°C$. Because of a crack in the frozen beer drop, no data is available for the frozen ice drop. From the liquid drops, an average speed of sound of $935.51m/s$ is found at room temperature and $924.12m/s$ at $0°C$ with a standard deviation of 6.43% and 9.04% respectively.

Figure 5.8 shows the drop of the experiment at room temperature and its corresponding A-scan plot. The peaks that are caused by bubbles are present before $10\mu s$. The bubbles in the drop increase the attenuation which is so strong that no second reflection can be seen in the plot.

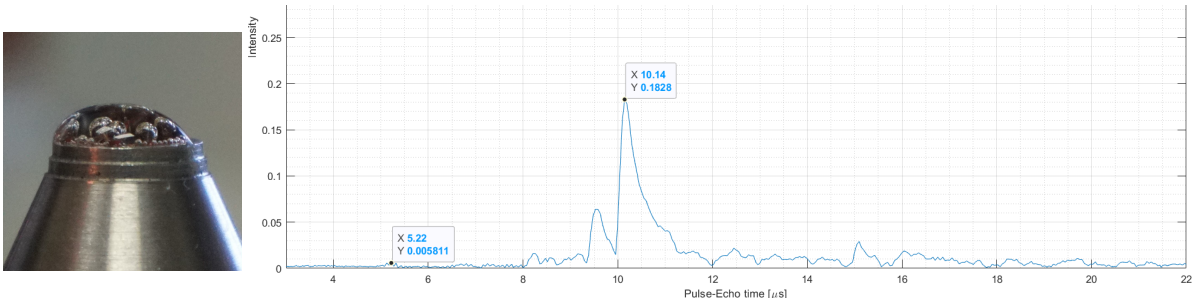


Figure 5.8: Drop experiment 12: alcohol free beer drop at room temperature. Left: picture of the beer drop. Right: A-scan of the ultrasonic signals with the top of the drop marked.

Karmeliet

Karmeliet has an alcohol content of 8.4%, a higher amount of carbohydrates ($6.8g/100ml$) but a lower amount of sugars ($0.3g/100ml$) in comparison with the alcohol free beer. The experiments with Karmeliet showed that the bubbles cause a noticeable noise in the ultrasonic response signal. This is because of the dynamic nature of these bubbles. They grow in size and move upwards, making it hard for the ultrasonic propagating waves to receive a static signal. In Figure 5.9 can be seen how the bubbles influence the signal before the main peak of the top surface of the drop. Note that this frame of the A-scan was taken after minutes waiting for the signal to stabilize. A freshly placed drop of Karmeliet has a lot of bubble activity that obscures the peak from the top of the drop.

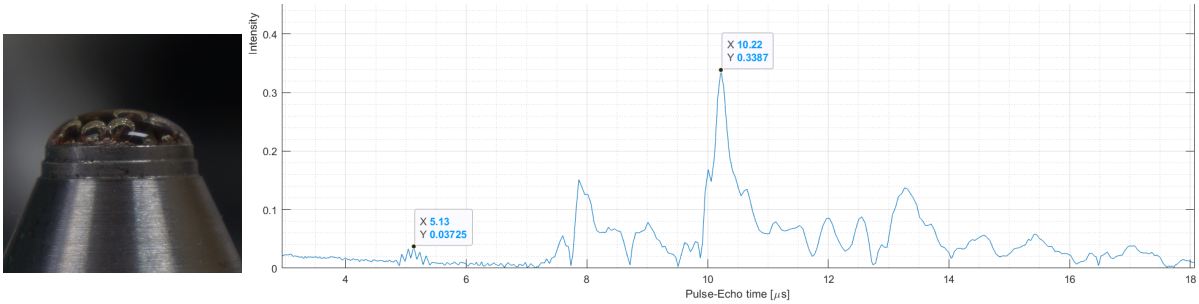


Figure 5.9: Drop experiment 49: Karmeliet beer drop at room temperature. Left: picture of the beer drop. Right: A-scan of the ultrasonic signals with the top of the drop marked.

The results of the drop experiments with Karmeliet give an average of $1529.74 m/s$ at room temperature and $1406.49 m/s$ at $0°C$. With a standard deviation of 2.04% for the room temperature experiment and 4.25% for the experiment at $0°C$ can be concluded that the experiments with liquid Karmeliet are fairly consistent. Only one experiment was able to capture valuable data for the frozen drop of Karmeliet. To make sure a crack in the ice would not prevent the ultrasonic waves to travel through the drop, the freezer was set at a temperature of $-27°C$. At this temperature, the speed of sound in frozen Karmeliet is measured to be $3208.56 m/s$.

To be able to compare the results of the Karmeliet drops, a drop of Karmeliet was stirred to make it release its gasses. When no more bubbles were present, the experiment was performed. The found speed of sound at room temperature conditions is $1619.34 m/s$. Comparing this to the literature value of a mixture with 8% of ethanol (alcohol) [23], which is $1531 m/s$, the difference is "only" 5.77%. Comparing this literature value with the found average speed of sound of Karmeliet with bubbles results in a deviation of 0.08%. But the literature value does not come from a mixture with bubbles, so this high performance should be interpreted with caution.

Conclusion beer drops
The lower speed of sound from the experiments with alcohol free beer can be related to the composition and the bubbles. For the experiments with Karmeliet, the experiment without bubbles showed an increase in speed of sound higher than the literature values for a mixture of water with 8% of ethanol [23]. This higher speed of sound can be attributed to the carbohydrates and other elements in this mixture. The reduction in speed of sound for Karmeliet drops compared to the speed of sound in the drop without bubbles can logically related to the presence of the bubbles.

5.4.3. Ethanol (96%)

Since beer is not exactly a mixture of only water and ethanol, it is hard to find appropriate literature for it. To benchmark the technique on substances other than water, ethanol is used with a purity of 96%. From Figure 5.10 can become clear that the ultrasonic propagation in the drop doesn't encounter a lot of damping. The first peak after the peak of the surface (at $7.55 \mu s$) of the transducer can be related to the top surface of the drop.

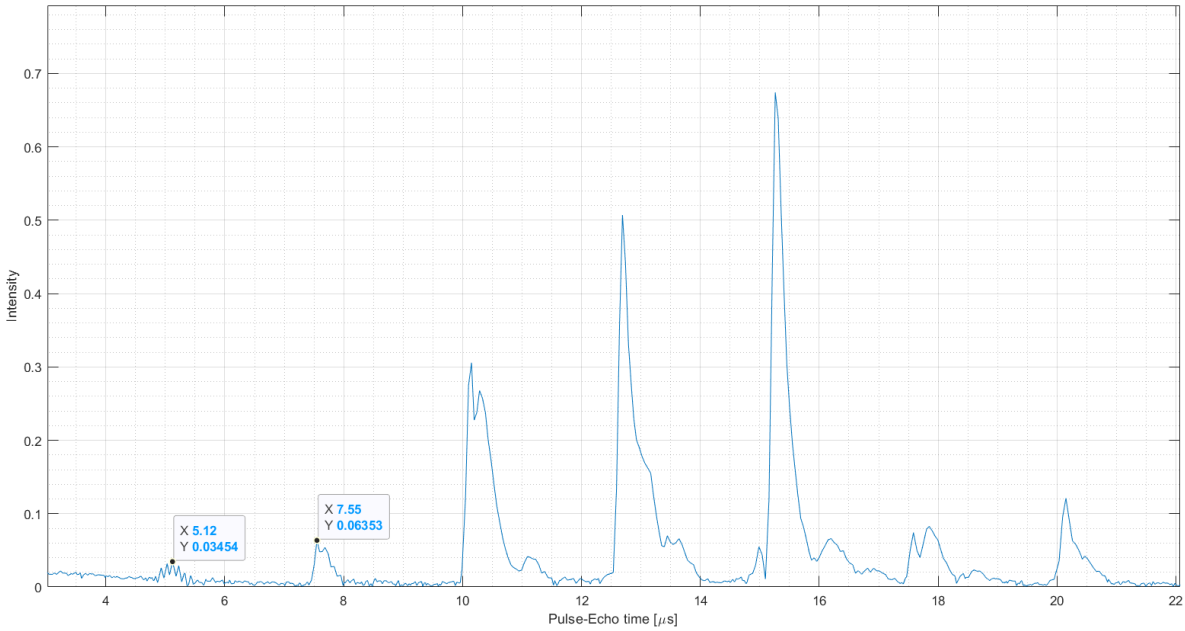


Figure 5.10: Room temperature A-scan of a drop of ethanol with 96% purity.

Note that the larger peaks that follow are a result of the shape of the drop and the fact that the transducer has two piezo-electric crystals in which one is the transmitter and the other is the receiver. This is visualized in the sketch in Figure 5.11 in which the wavefront close to the center (wavefront 1) creates the first peak because it is the only one that requires a single reflection before the wave touches the receiving piezo-electric crystal (Rx). The other wavefronts (2,3 and 4) require 3 or more reflections. Therefore, the distance travelled by these waves is larger causing the ToF of the other peaks to be larger than the first one. Waves 2, 3 and 4 also have a different horizontal distance to cover, which makes them form individual peaks.

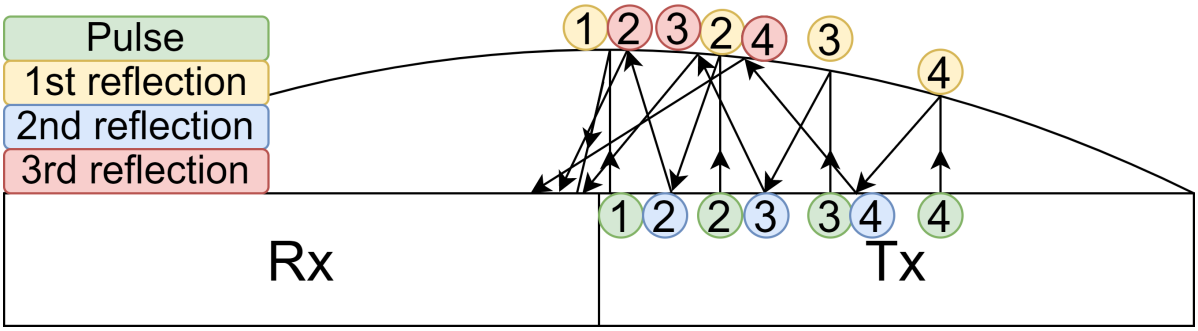


Figure 5.11: Reflections inside of a shallow drop such as the one for ethanol. Rx and Tx resemble the receiving and transmitting piezo-electric crystals respectively. The waves start all together at the transmitting crystal (Tx) and are numbered 1, 2, 3 and 4. As can be seen by the reflections, only wave 1 reaches the Rx crystal after a single wave.

From the ultrasonic ToF from the plot in Figure 5.10, a speed of sound of 1131.69m/s can be derived. The literature value for the speed of sound of pure ethanol is found to be 1142m/s [40] which makes the difference only 0.90%. As a sidenote should be added that during this experiment, the ToF of the peaks was growing smaller slowly but steadily (peaks moved to the left). This is most likely related to evaporation of the ethanol at room temperature. Therefore the height of the drop should be monitored frequently when experiments require a long term exposure to atmospheric conditions.

5.5. Irregularities

The high number of experiments allowed for several independent irregularities to be discovered. They are easily overlooked because they are hardly noticeable even though they influence the outcome in some way. These will be discussed in further detail in this paragraph.

5.5.1. Ultrasonic signal during phase transition (Freezing & Melting)

The good thermal conductivity of the transducer causes the transducer to quickly have a temperature close to the ambient temperature (freezing temperature of room temperature) which makes the bottom of the drop to have the largest heat transfer. This is valid both for freezing and melting.

Freezing

The freezing of the liquid drop of Experiment 48 is shown in Figure 5.12. This experiment was done with water without bubbles in order to be able to show clear results, but it is important to understand that this freezing behavior applies to all type of drops.

The drop gradually cools down from the bottom until the water is close to the freezing temperature (see top graph of Figure 5.12). Once ice starts to grow, it grows from the bottom and it blocks the ultrasonic waves to further locations in the drop (see second graph of Figure 5.12). If the thickness of the ice becomes significant, a peak appears in the ultrasonic graphs. This peak moves slowly to the right in the graph, which means that the ice thickness is still growing (see third graph of Figure 5.12). Eventually the drop is rigid and the ultrasonic signal stops moving (see bottom graph of Figure 5.12). This is when the drop completed its freezing process.

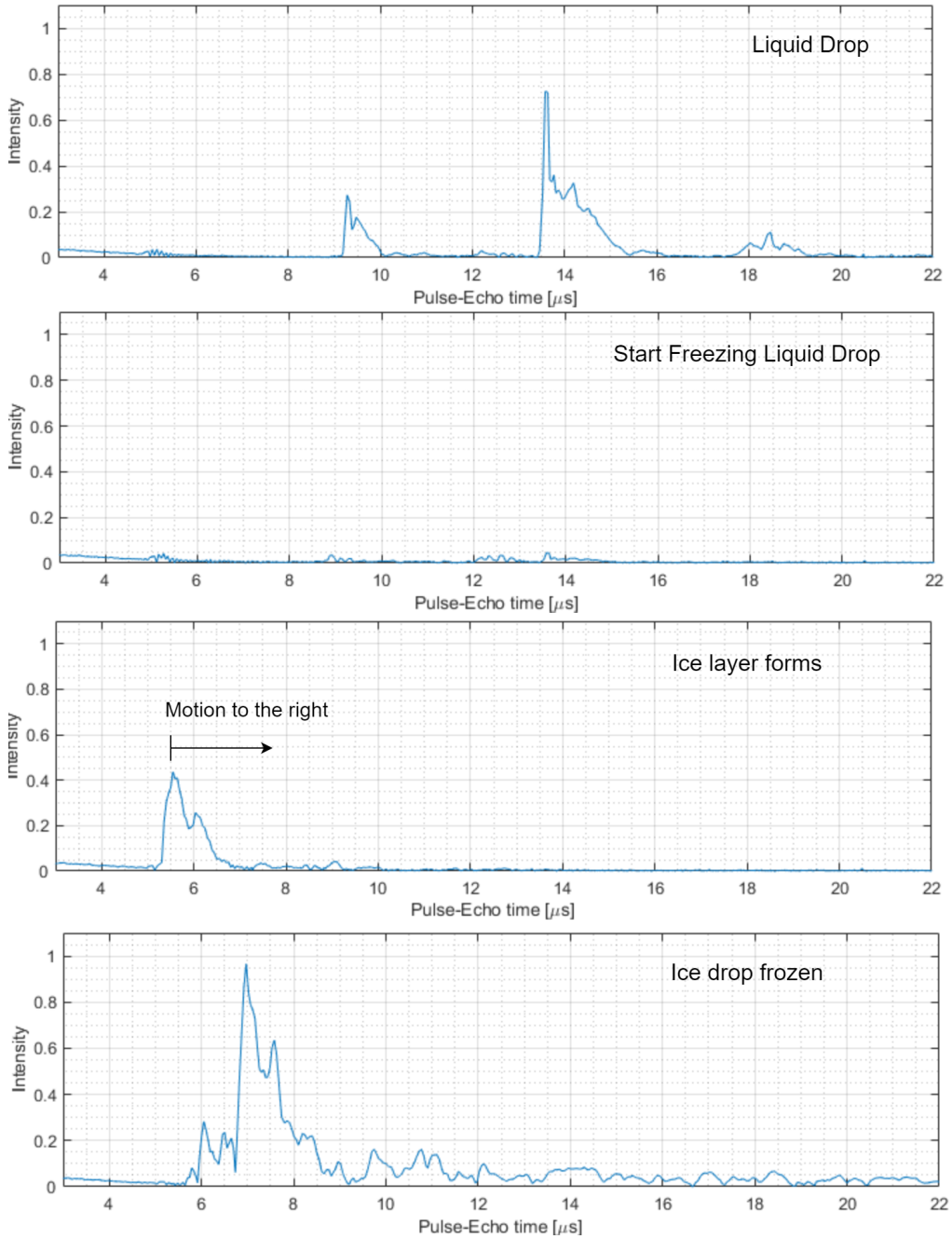


Figure 5.12: Freezing of the liquid drop of Experiment 48 visualized in frames chronologically ordered from top to bottom. The top graph shows the last signal of the liquid drop, before the freezing sequence that starts with the second graph. A peak grows from the transducer which is the ice layer that is formed in the second last graph. The last graph shows the ultrasonic response after the drop is completely frozen.

Melting

After a frozen drop is taken out of the freezer, the transducer and the drop start to warm up. Because of the high thermal conductivity of the transducer, the drop primarily melts from the bottom as shown in Figure 5.13. The ultrasonic signals from the ice drop remains visible until a layer of water starts to emerge from the bottom by the melting of the drop. Similar to the freezing of the drop, the ultrasonic signal will shortly disappear. But once there is a visible layer of liquid water, a peak can be observed in the A-scans. This peak is the boundary of the water and the ice that floats on top of it. As the drop melts further, the layer of water becomes larger and the peaks move further to the right. Because of the lower speed of sound for water than for ice, the peaks seem to move faster than for the freezing of the drop. When the peaks stop moving, their

ToF remains constant and all ice has melted.



Figure 5.13: Melting sequence of drop experiment 45. The melting primarily starts at the bottom of the drop. The drop melts from the top surface to a lesser extent.

5.5.2. Cracks in Ice

When drops are placed on the transducer and put in the freezer, they cool down and form ice. Unfortunately, sometimes during the formation of the ice, cracks in the ice occur which blocks the path for the ultrasonic signal to reach the top surface of the drop. Most of the time, the crack is located on the surface between the transducer and the ice drop. This type of crack is hard to discover because it is not visible in the images. This can only be confirmed with ultrasound which gives no reflective signals at all in this case.

In some cases, cracks occur in between the bottom and top of the frozen drop (see Figure 5.14). In these cases, the the ultrasound seems to reflect on the crack, which makes it almost impossible to determine the peak from the top surface of the frozen drop.



Figure 5.14: Examples of drops with cracks. The two left most images are from drop experiment 28 while the two right most images come from drop experiment 29.

The reason for the existence of these cracks is thought to come from the freezer. The freezer cools by blowing cold air from the top back of the freezer. For the first set of experiments the drop was located on the top shelf in the freezer, which preserved the drop to be in the stream of cold air. Once the drops were measured ultrasonically while freezing, the transducer was placed a shelf down to allow the wire inside. The cold air from the freezer might have come down on the drop, causing it to start freezing from the top and the bottom simultaneous. Both freezing directions would meet halfway, causing a crack in the drop. This problem was fixed by placing a cardboard box upside down over the transducer while freezing. After this adaptation, no more drops with cracks halfway were grown. The cracks at the surface of the transducer and the bottom of the drop could still occur, but to a lesser extent.

A fun exercise that can be done is take the ToF from the existing A-scans for the drops with cracks and perform the theory backwards now, in order to estimate the height of the crack in the ice drop by using literature values for the speed of sound. For drop experiment 29, corresponding to the two right most pictures in Figure 5.14, this resulted in a crack height of $2.19mm$ measured from the bottom of the drop. Note that this was not possible for drop experiment 28 because that crack was more vertical, acoustically separating the two parts of the drop causing the receiving piezo-electric crystal to not receive any signal.

5.5.3. Feature at $\pm 1\mu s$ ToF in ice drops

From the ice drop experiments without bubbles, a remarkable feature in the ultrasonic response signals stands out (see Figure 5.15). What is unexpected is that its ToF is between the surface of the transducer and the top of the drop. This strange peak consistently returns and is only present when the drop is frozen. By noticing this, it became clear that if the frozen drop is too small, the peak of the surface of the drop might be superposed on top of this feature making them hard to distinguish.

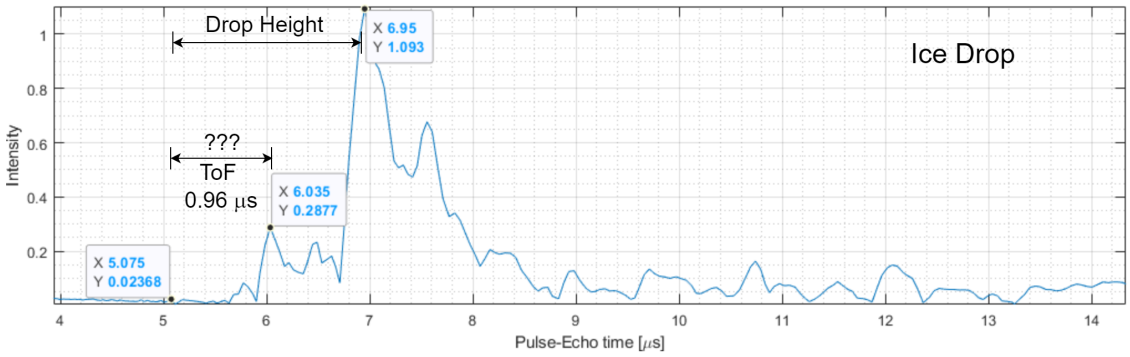


Figure 5.15: A-scan of the ice drop of experiment 48. In this graph, the ToF of the drop height is marked as well as the odd feature that has a ToF of $0.96\mu s$.

A suspected cause of this ultrasonic peak is the presence of surface waves. They travel in a transverse direction of the longitudinal acoustic propagation on boundary surfaces in solids. Surface waves are usually never the cause of a misreading in ultrasound because they travel with a much lower velocity ($c_surface = 1900m/s$ at $-16°C$ [39] compared to $c_long = 3883m/s$ at the same temperature). This is why surface waves are usually found as small disturbances at the end of the ultrasonic scans while the peak of the longitudinal wave is found in front of this scan.

In this case, however, the surface wave caused by the transmitting piezo-electric crystal (Tx) travels directly towards the receiving crystal (Rx) (see Figure 5.16). The surface waves would only have to cross the small gap between Tx and Rx, which is less than $1mm$. Even though the longitudinal waves are faster, they will arrive later because they travel twice the distance to the top of the drop.

Bringing up surface waves as a likely cause for this peak has been one hypothesis to explain such feature. The only way to prove whether or not this was the case is by performing a similar drop experiment with a transducer that has only one piezo-electric crystal that would be used for transmitting and receiving the ultrasonic signals. Unfortunately no single-crystal transducer, capable of placing a drop upon, was available at the time the drop experiments took place.

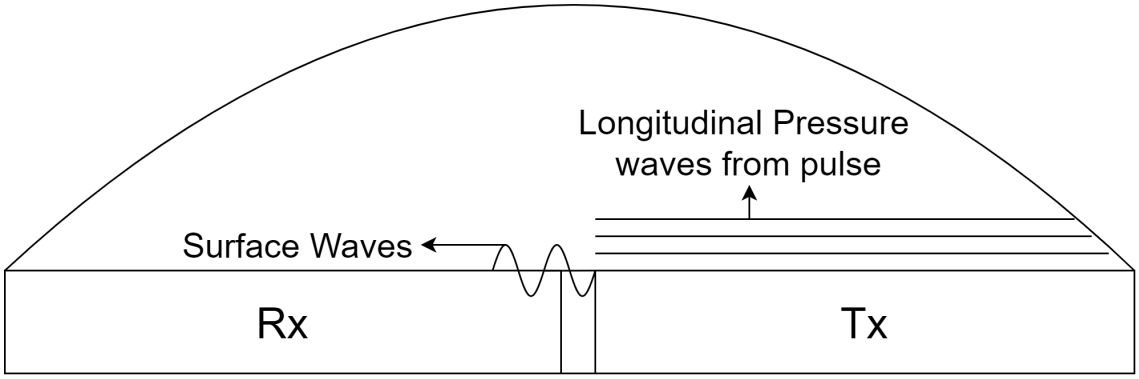


Figure 5.16: Suspected cause of the strange ultrasonic response that keeps occurring: A surface wave travels through the surface of the frozen ice from the transmitting piezo-electric crystal to the receiving one on the transducer. Even though the speed of the surface wave is about half of the longitudinal wave, the surface wave will arrive first at Rx because the distance to travel is so small.

5.5.4. Room Temperature variations

The room temperature experiments were taken without measuring the temperature of the room and the room was not held at a constant temperature as described by the S.I. metric system. This is why during the course of the drop experiments, the measured speed of sound started to change slightly. The drop experiments were held in the month of October 2020, spread over about three weeks. In this month, the maximum temperatures changed from about 25°C to 18°C during the scope of the experiments. When plotting a trendline through the scatter plot of the drop experiments that were ordered chronologically, it becomes clear that the room temperature drops were susceptible by the changing room temperature (see Figure 5.17). The spread of the experiments can be the result of temperature variations during the day (colder in the morning, warmer in the afternoon). The average values correspond to a temperature of 21.5°C which is close to the "official" room temperature of 20°C. Considering this, the experiments provided an average result very close to the literature value because the average room temperature was close to the official room temperature.

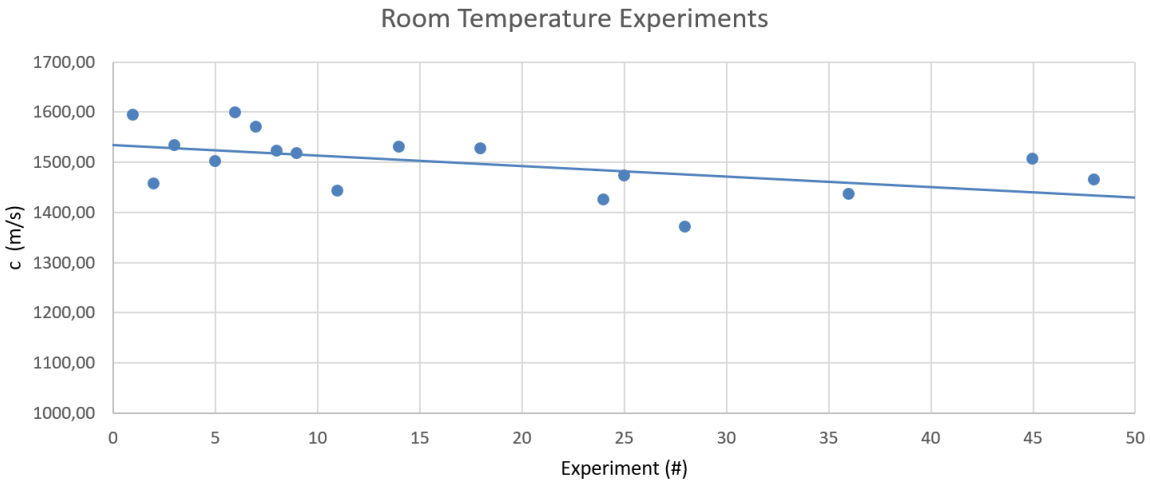


Figure 5.17: Ultrasonic velocity of room temperature experiments for compact water. The x-axis represents the chronological experiment number (up to 52).

6

Vacuum Chamber Experiments and Results

6.1. Vacuum Chamber Experiments

The first vacuum chamber that was used for these experiments gave meaningful results that are all listed in Appendix C. Various types of vacuum chamber experiments were done with different deposition approaches that will be further discussed in this section by level of complexity.

6.1.1. Without ice deposition

Experiments without any deposition of ices were proposed so that the influence of cooling the system towards an equilibrium temperature could be studied. This also enables us to see what the ultrasonic signal looks like without any deposition in order to understand the influence of the depositions and the grown ice on the substrate which is visible in all other experiments. The B-scan of Experiment 15, that will be used as an example, is shown in Figure 6.1. In the figure, the colors represent positive (yellow) or negative (Dark blue) values while almost zero values are shown in light blue and the intensity of the ultrasound can be noticed by the color vividness. The x-axis shows the time the experiment takes and the y-axis shows the Time of Flight (ToF) the ultrasound travels trough the methacrylate. Different phases through the experiments are marked in this plot. In this plot can be seen that the ToF becomes smaller during the cool down phase. This is because the methacrylate gets cold and the speed of sound in methacrylate is inversely proportional with temperature [10]. After some time, the temperature reaches an equilibrium, causing the contraction of the methacrylate to be stable as well which can be seen as the stable ToF in the figure. When no more liquid nitrogen is added, the substrate starts to warm up which is indicated by "warm up + desorption". Since the vacuum in the chamber is maintained, the warm up of the substrate occurs gradually and at a much slower pace compared to the cool down phase. After the warm up exceeds the sublimation temperature of water ice ($198.15K - 273.16K$ for the pressure range of $10^{-3} mbar - 6.12 mbar$ [28]), any frozen molecule would be sublimated and the temperature steadily stagnates towards room temperature.

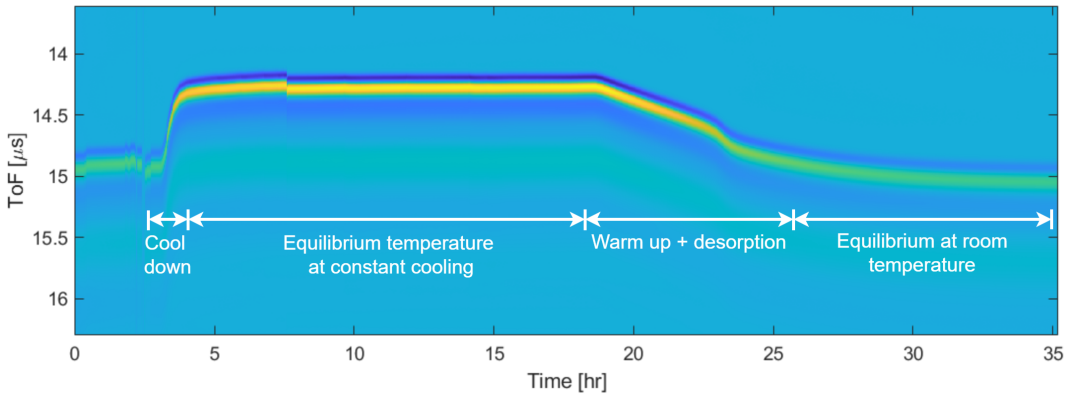


Figure 6.1: Ultrasonic B-scan of the experiment without deposition on 15/07. Different phases in the experiment are marked. The x-axis represents the amount of hours the experiment takes, the Y-axis is the ToF it takes the ultrasonic pulse to reach the surface of the methacrylate substrate and travel back to the transducer.

Temperature sensors were placed on the sample holder and on the methacrylate substrate at the mesa and close to the transducer. During the experiment, these sensors record the temperature once every 30 seconds. The temperature of these sensors is plotted in orange in Figure 6.2. The average temperature of the methacrylate is considered to be the average of the two measured values on the substrate (on the mesa and close to the transducer). The plot contains a graphical representation of the setup that is located in the graph in such a way that the lines of the temperature cross their physical placement on the methacrylate substrate. The temperature sensor on the sample holder was mounted at the bottom of the copper piece. From this plot can be concluded that the methacrylate is an excellent thermal insulator. The blue line in the plot represents the ToF of the largest peak derived from the ultrasonic data which would correspond to the surface of the methacrylate substrate.

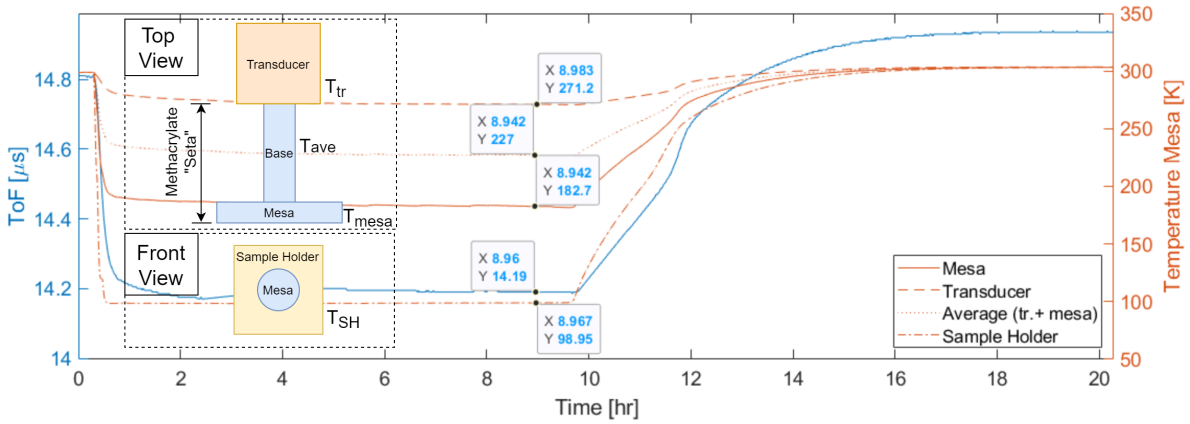


Figure 6.2: Blue: the ToF of the peak of the reflection of the surface of the substrate throughout the experiment. Orange: Temperature measurements on the "Seta" through which the ultrasonic wave travels. The lowest temperature is measured at the copper sample holder. A sketch is provided to illustrate the positioning of the temperature sensors on the Seta: one close to the transducer and one on the mesa.

The speed of sound in methacrylate at low temperatures has been reported in literature [10]. A linear dependency can be found between the speed of sound in methacrylate and temperature. This corresponds to $c_{PMMA} = 3367.5 m/s - 1.955 m/(sK) * T$ in which c_{PMMA} is the speed of sound and T is the temperature in Kelvin. When assuming that the temperature of the methacrylate is the average of the temperatures measured close to the transducer and the mesa, the theoretical speed of sound in the methacrylate substrate throughout this experiment can be calculated, resulting in the graph of Figure 6.3. From this graph can be seen that the speed of sound increases from $2783 m/s$ to $2925 m/s$ in the temperature range from $\approx 300K$ to $\approx 180K$.

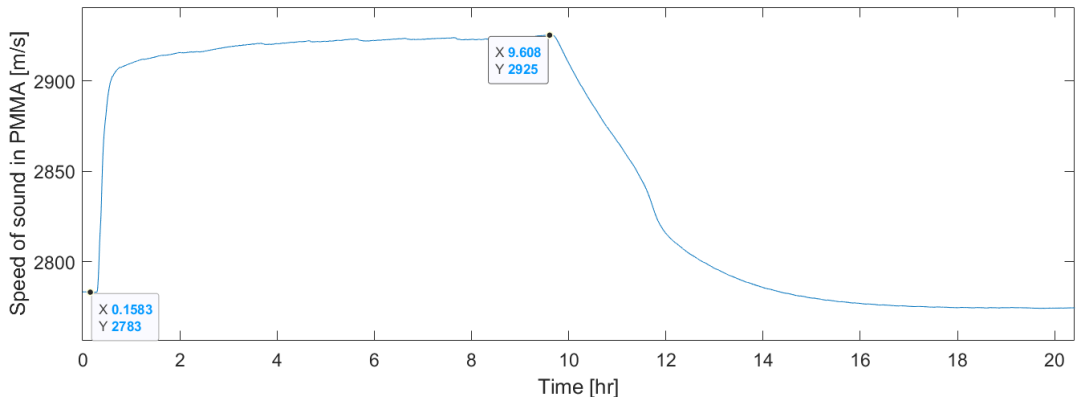


Figure 6.3: Speed of sound derived from the average temperature in the methacrylate throughout the experiment.

Lastly, a sensor measures the pressure in the vacuum chamber throughout the experiment which is plotted in the graph in Figure 6.4 together with the temperature measurements. As can be seen in the graph, the pressure in the vacuum chamber reached minimum pressure levels in the order of $10^{-2}mbar$, before the cool down of the substrate started. After the cool down the pressure dropped by an order of magnitude. This is caused by the freezing of atmospheric water molecules that remain present in the vacuum chamber in a gaseous form even though the vacuum pump runs for an extended period of time. While the experimental setup remains cooled, the pressure stays constant (in the order of $10^{-3}mbar$). During the warm up, a large peak in the pressure appears (while continuously running vacuum pump). This indicates desorption of water molecules that froze onto cold surfaces in the setup. The fact that it is spread over a certain temperature range over time points out that the desorbing water ice is present on surfaces with different temperatures. The warm up of the system occurs gradually over the frozen surfaces which is why the ice can desorb at some places first while other surfaces remain below the freezing temperature. Also note that after the temperatures exceeded the freezing temperature of ice, gaseous water vapour is present in the vacuum chamber again which leaves the chamber with a higher pressure.

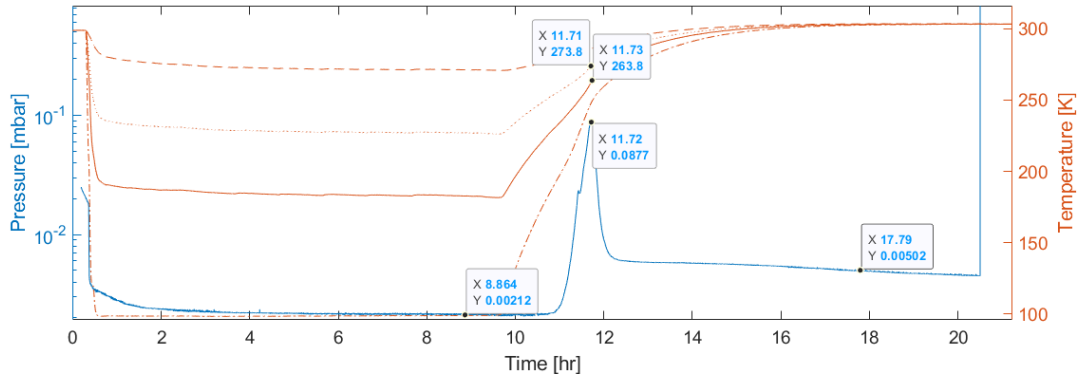


Figure 6.4: Blue: Pressure in the vacuum chamber throughout the experiment. Note that there is a pressure peak caused by accreted water molecules even though the deposition valve remained closed throughout the entire experiment. Orange: Temperatures on the sample holder, the mesa and the transducer. The average of the last two is added as a reference temperature of the methacrylate substrate.

6.1.2. H_2O deposition without refill of the deposition tube

Since the temperature of the mesa is considerably warmer than in the simulations (see Table 4.1), it can be concluded that the contact surface between the sample holder and the mesa is rather poor in reality. During the regular H_2O deposition experiments, lower mesa-temperatures could be achieved. This led to believe that water molecules freeze into the gaps between the surfaces, enhancing the thermal conductivity through the ice. The experiment with the deposition without refilling the deposition tube with water released into the vacuum chamber aims to demonstrate the cooling capabilities of the system after the first deposition. From the B-scan in Figure 6.5 it can already be seen that the deposition phase influences the contraction of the methacrylate noticeably by the reduction in ToF. The ultrasound travels faster through the methacrylate because its retraction makes the distance the pulse need to propagate through, smaller. The steady, slow

cooling phase after the deposition shows an even further contraction of the methacrylate.

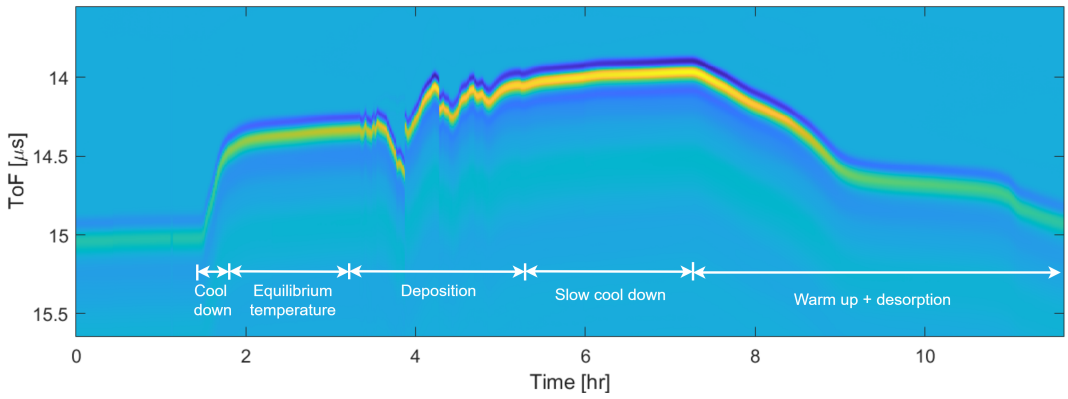


Figure 6.5: B-scan of the experiment on 22/07 with a single H_2O deposition. Different phases in this experiment are marked in white.

Having a lower temperature at the mesa is beneficial because gaseous molecules are more drawn towards them for accretion, resulting in a well distributed ice layer. Therefore the performance of the increased thermal conductivity between the sample holder and the mesa is important. When analyzing the results from the graph in Figure 6.6, it can be noticed that the temperature of the mesa dropped from 185K ($-88.15°C$) to 124.5K ($-148.65°C$) which is a difference of $60.5°C$. This demonstrates that the thermal conductivity of the water ice of one deposition significantly increases the freezing potential of water ice on the substrate. Also note that the temperature on the transducer side also dropped to 248.8K ($-24.35°C$) while the function of the methacrylate was to form a thermal barrier in order for the transducer to have a temperature above its rated minimum temperature of 253.15K ($-20.00°C$). Even though reaching this temperature on the transducer side was unintended and unwanted, the transducer kept on working fine without consequences.

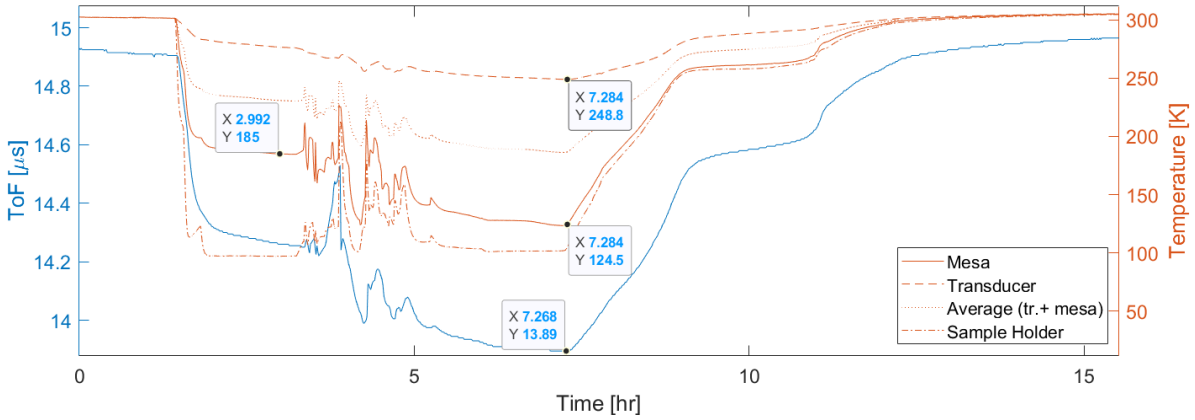


Figure 6.6: Blue: the ToF of the peak of the reflection of the surface of the substrate throughout the experiment. Orange: Temperatures on the sample holder, the mesa and the transducer. The average of the last two is added as a reference temperature of the methacrylate substrate. The different phases in the experiment are the cool-down phase (the steep decrease in temperature that happened between $x = 1.5hr$ and $x = 2hr$), the temperature equilibrium phase (from $x = 2hr$ to $x = 3.2hr$), the deposition phase (from $x = 3.2hr$ to $x = 5.2hr$), the slow cool down phase (from $x = 5.2hr$ to $x = 7.2hr$) and the warm up + desorption phase (from $x = 7.2hr$ till the end).

The lower temperature causes the average speed of sound in the methacrylate to rise as well as the methacrylate to shrink. Both of them cause the ToF of the outer edge of the substrate to shrink to $13.89\mu s$ (see Figure 6.6). Figure 6.7 shows that the average speed of sound in the methacrylate went from $2778m/s$ at room temperature to $3003m/s$ at the lowest temperature in this experiment.

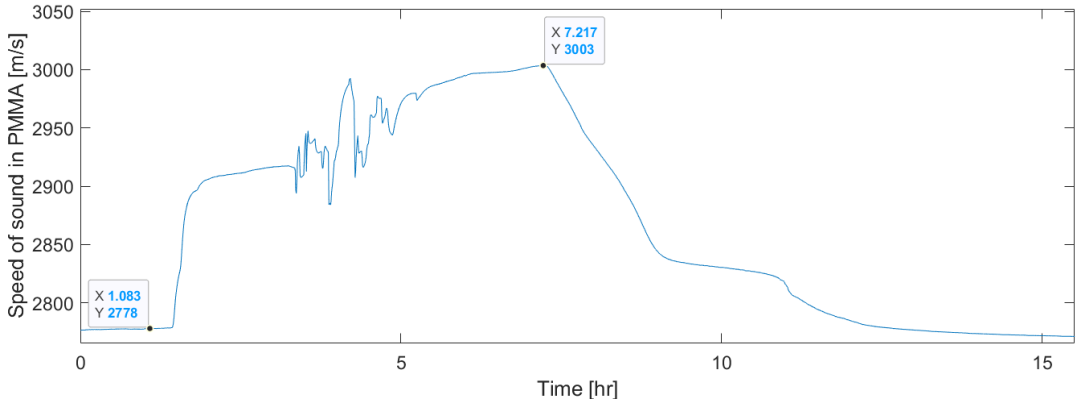


Figure 6.7: Speed of sound derived from the average temperature in the methacrylate throughout the experiment.

In Figure 6.8 can be seen how the pressure changes during the experiment. The large peak at 3.366 hours in the experiment resembles the opening of the valve that contains a tube with water for the deposition. After that the valve is kept partially open so that the deposition pressure stays low enough. When the pressure comes close to the pressure before the opening of the valve, the valve is switched open more. The evaporation of the liquid water in the deposition tube demands energy to evaporate which makes the water in the tube drop in temperature. When little water is left, this even causes the water to freeze inside the deposition tube which ceases the evaporation rate and becomes a slow sublimation rate (because the ice on top of the water blocks the water from the vacuum). In this experiment, the tube was warmed from the outside when ice was present inside. This is done by submerging part of the tube in a bowl with warm water. This melts the ice inside the deposition tube and therefore increases the evaporation rate and also causes the evaporated water molecules to have a higher temperature. The warm water molecules introduce more thermal energy inside of the vacuum chamber that needs to be cooled. This is why the temperature fluctuates while the deposition pressure remains low.

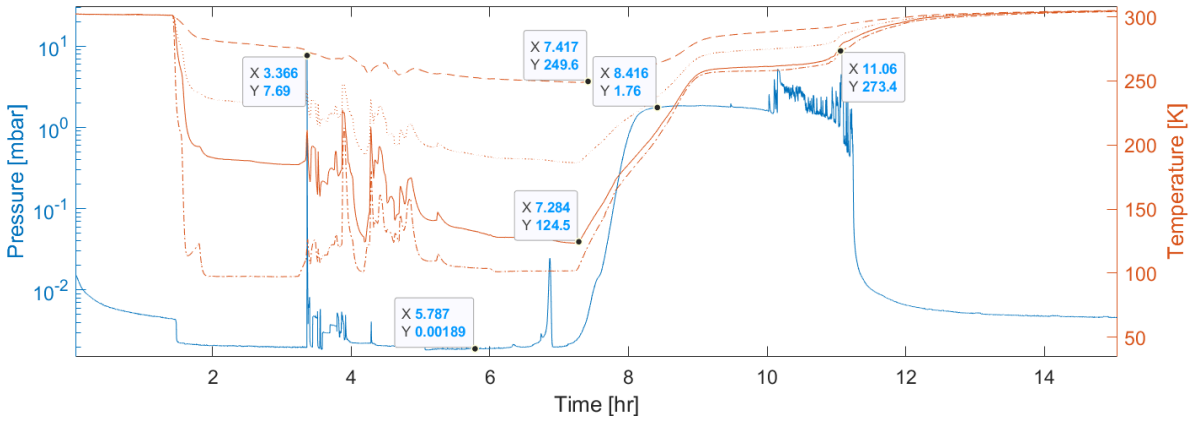


Figure 6.8: Blue: Pressure in the vacuum chamber throughout the experiment. Orange: Temperatures on the sample holder, the mesa and the transducer. The average of the last two is added as a reference temperature of the methacrylate substrate.

When the warm-up starts (from $x = 7.2hr$ till the end of the experiment), so does the desorption. From the pressure in the graph in Figure 6.8 can be seen that the desorption reaches a relatively constant pressure of $1.76mbar$ for roughly 4 hours. During the desorption, the temperature stays below the sublimation temperature at that pressure which can be seen by the flat nature of the curve the temperature sensors report. The ice in the vacuum chamber therefore keeps the substrate cool during the desorption of the ice. When taking a closer look at the shape of the pressure curve, the desorption can be categorized into two parts: One with a steady pressure and one with a turbulent pressure. The steady part is from the straight forward desorption that propagates from the icy surfaces themselves. The turbulent part is likely superposed onto the steady part. These sporadic periods of temporal pressure increase are thought of to originate from ices that are trapped inside cavities of the structure of the sample holder and released when those specific cavities surpass the sublimation pressure of the ice.

6.1.3. H_2O deposition with multiple refills of the deposition tube

The largest number of experiments done, were experiments with H_2O depositions. They aim for ice growth on the mesa, in order to become measurable by ultrasound. The experiment of 24/07 is a good example (see Figure 6.9).

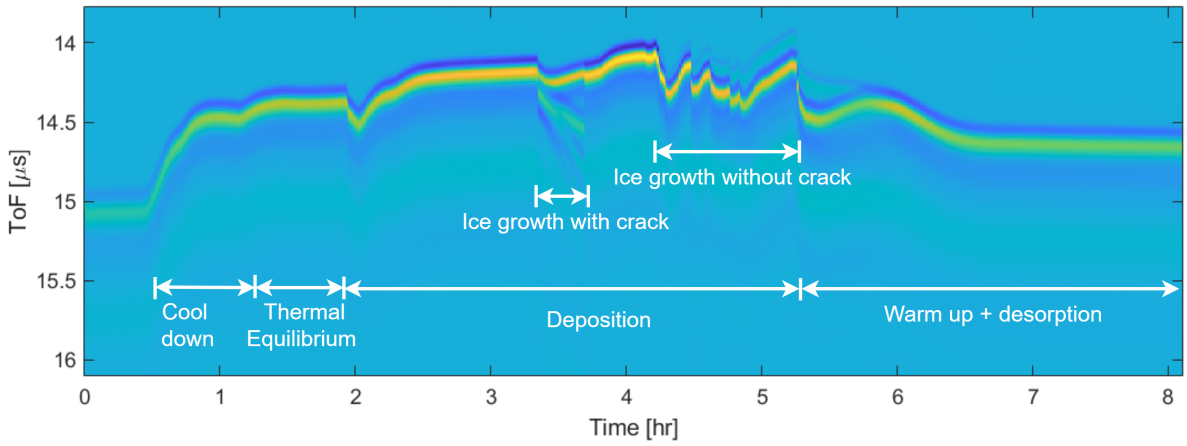


Figure 6.9: B-scan of the experiment on 24/07 with H_2O. A number of different phases in the experiment are marked with white. The growth of ice is noticeably visible in this experiment. Apart from the expected ice growth, the first ice growth showed signs in the ultrasound of a possible crack that eventually resulted in a piece of ice falling off the substrate.

In Figure 6.9, ice is marked two times. The first time ice grew on the mesa, the signal of the ice detached from the signal of the boundary of the methacrylate. Even though this is desired, the fact that the intensity of the ultrasonic signal of the reflected ice is lower than the one from the methacrylate, points at a weak bond between the two materials (possibly a crack). This ice eventually detached physically from the methacrylate substrate. The second grown ice shows the ice growth clearer. Here the first, low-intensity peak is attributed to the boundary between the mesa and the ice while the highest intensity peak comes from the surface of the ice. From this B-scan, the ultrasonic signal that was present at the 5.2 hour mark is shown separately in Figure 6.10. From this figure can be seen that the estimated difference in ToF is about $0.15\mu s$.

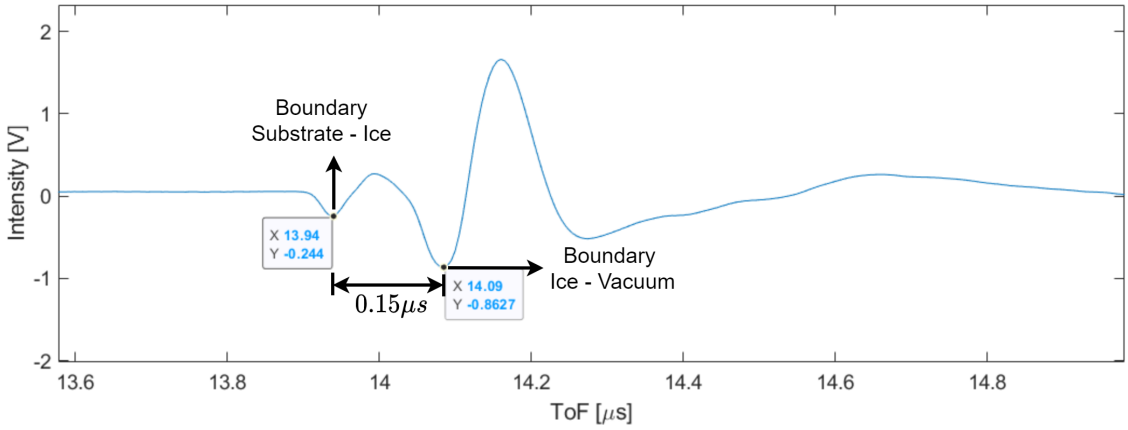


Figure 6.10: Ultrasonic signal at about 5.2 hours into the experiment. The first, smaller peak comes from the boundary between the methacrylate and the ice. The second, larger peak resembles the end surface of the grown ice on the substrate.

When considering the speed of sound of compact ice used in the ice drop experiments ($3888.50 m/s$), this would correspond to an ice thickness of $t = \frac{1}{2} * ToF * c_{ice} = \frac{1}{2}(0.15 \cdot 10^{-6} s \cdot 3888.50 m/s) = 0.2916 mm$. Assuming this value for the speed of sound though, is not a good assumption because it represents the speed of sound of compact ice at $-18°C$ while the measured temperature on the mesa is 123.8K or $-149.35°C$ (see Figure 6.11). Furthermore, the presence of porosity is neglected in this calculation. Multiple attempts tried to measure the grown ice thickness with a Laser Doppler Vibrometer (LDV), but the outcome of these measurements were not useful. An example of such a measurement is provided in the appendix. Ideally, the thickness of the ice

could be derived from these measurements so that the exact speed of sound in this ice can be calculated which could potentially be linked to a level of porosity.

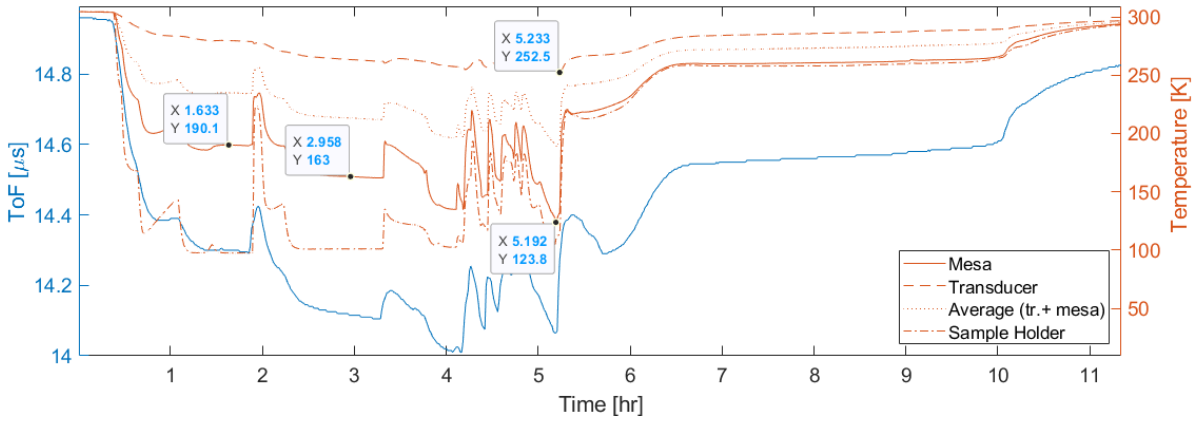


Figure 6.11: Blue: the ToF of the largest peak of the reflection of the ultrasonic pulse throughout the experiment. Orange: Temperatures on the sample holder, the mesa and the transducer. The average of the last two is added as a reference temperature of the methacrylate substrate.

When analyzing the contraction of the methacrylate by the plot in Figure 6.11, one should keep in mind that the growth of ice influences the peak of the ToF that resembles the blue line in this figure. Since the algorithm that determines this ToF chooses the peak with the highest intensity, it changes from the surface of the methacrylate to the surface of a growing ice analog. In practice, this means that the reported lowest ToF occurs at about the 4 hour mark while the temperature at the 5.2 hour mark is lower. This is because the ToF at the 4 hour mark is without ice, so the ultrasonic pulse with the highest intensity travels through the methacrylate alone. In case of the signal at the 5.2 hour mark, it travels through the methacrylate and the grown ice analog.

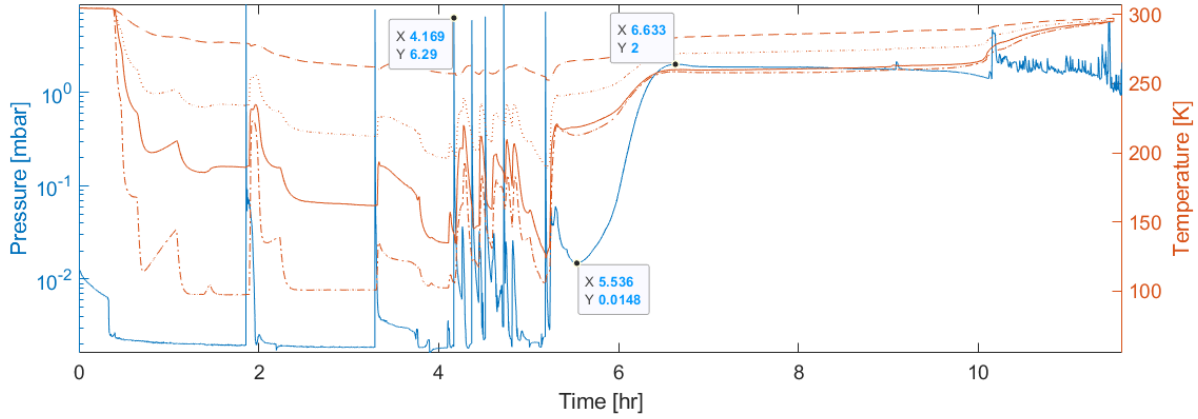


Figure 6.12: Blue: Pressure in the vacuum chamber throughout the experiment. Orange: Temperatures on the sample holder, the mesa and the transducer. The average of the last two is added as a reference temperature of the methacrylate substrate.

From the plot in Figure 6.12 can be seen that the experiment had 7 deposition tubes filled with water by the pressure peaks present in this graph. The first deposition (at $x = 1.9hr$) made sure the mesa would have a sufficiently cold temperature. The second deposition (at $x = 3.3hr$) already grew some ice on the substrate, but the bonding between the ice and the methacrylate did not allow for good acoustic propagation through the ice. Eventually this ice cracked and fell off of the mesa. After this the temperature dropped even further and 4 more depositions were done (between $x = 4.2hr$ and $x = 4.7hr$) with successfully growing a large ice that shows in the B-scan. An ice analog was able to grow and was visible in the ultrasound. When the last deposition was done (at $x = 5.2hr$), the liquid N_2 ran out. This caused the system to loose its cooling capabilities. The warm water vapor of the last deposition caused the temperature in the vacuum chamber to rise quickly after which the desorption set in. The valve of the deposition tube was closed as soon as

the temperature could not go down anymore. The desorption of this experiment took a long time. This graph shows a smooth desorption that took roughly 4 hours after which the desorption with more turbulent superposed values started for a couple of hours more. Unfortunately, the measurements of the experiments were stopped before the 12 hour mark, but the shape of the desorption part in the pressure would be similar, but more elongated, than to the one in Figure 6.8.

6.1.4. CH_3OH deposition

Looking into the deposition of other possible molecules of astrophysical importance on the substrate, the ones listed in Table 6.1 were considered. Because of the limitations in vacuum and minimum temperature, some ices are not possible to grow in the vacuum chamber. The minimum pressure that can be reached with the vacuum chamber after cooling down is $\approx 10^{-3}$ mbar and its minimum temperature on the substrate is $\approx 123.15K$ ($-150°C$) after initial deposition to increase the thermal conductivity between the sample holder and the methacrylate.

The most viable other ice to grow apart from water would be ammonia (NH_3), but since it is not suitable for the current setup because this is a gas and the deposition tube is only made for liquids, another ice should be chosen. CO_2 and mehtanol CH_4 require a temperature that cannot be reached on the mesa of the substrate at vacuum chamber pressures, which eliminates them from the viable options that are present. With a poorer vacuum though, the sublimation temperature of CO_2 rises (eventually to -78.5°C at 1 bar). In the case of ethanol and methanol, the freezing temperatures can be reached, but the triple point pressure is low. For methanol the triple point pressure is close to the limit of the vacuum chamber and for ethanol it is three orders of magnitude lower.

This practically means that the grown ice is more likely to melt into a liquid at deposition pressure which is not beneficial in the vacuum chamber. This is why for ethanol a Turbomolecular Pump (TMP) will be necessary to grow it into an ice analog. For the creation of methanol, the implementation of a TMP is only recommended. Since the logistics of installing a TMP would take a long time, the experiments were chosen to proceed with methanol without the TMP.

	T_{max} [K]	T_{max} [°C]	P [mbar]	Viable?	Comment
H_2O [38]	199.56	-73.59	10^{-3}	Yes	
CH_3OH [20]	175.61	-97.54	$1.86 * 10^{-3}$	Yes	Around triple point
CH_3CH_2OH [30]	150.00	-123.15	$4.4 * 10^{-6}$	Yes	After implementation of TMP
$CO_2(P_{atm})$ [13]	194.65	-78.5	1000	Yes	Possible with higer pressure
$CO_2(P_{vacuum})$	105.09	-168.06	10^{-3}	No	Required T too low
NH_3 [38]	135.93	-137.22	10^{-3}	Yes	
CH_4 [32]	44.84	-228.33	10^{-3}	No	Required T too low

Table 6.1: Viability check for different substances of astrophysical importance to grow ice on the mesa in the vacuum chamber. For methanol (CH_3OH), a Turbomolecular Pump (TMP) is advised. A TMP is necessary to form ice of ethanol (CH_3CH_2OH). In this table, T_{max} is the maximum temperature at which the compound can be in ice-form in combination with the displayed pressure (P).

A typical B-scan of an experiment with the deposition of methanol looks as shown in Figure 6.13. In this figure can be seen that ices grow several times after which the signal of the ice suddenly stops. While comparing it to the graphs in Figure 6.14 and Figure 6.15, it becomes clear that the second ice feature referred to in the B-scan lost its physical bond with the mesa most likely because of a crack. The first marked ice feature from the B-scan also disappears quickly, but this happened because of a chain reaction that is related to the fact that the methanol ice in the vacuum chamber turns liquid. Unfortunately, these experiments did not result in ice formation as clear as for water ice. In these experiments the ToF of the methanol ice could not be isolated visually. Deconvolution theory came up as a viable way of signal processing to find this ToF, but applying this theory was not straight forward which led to having to discard this technique.

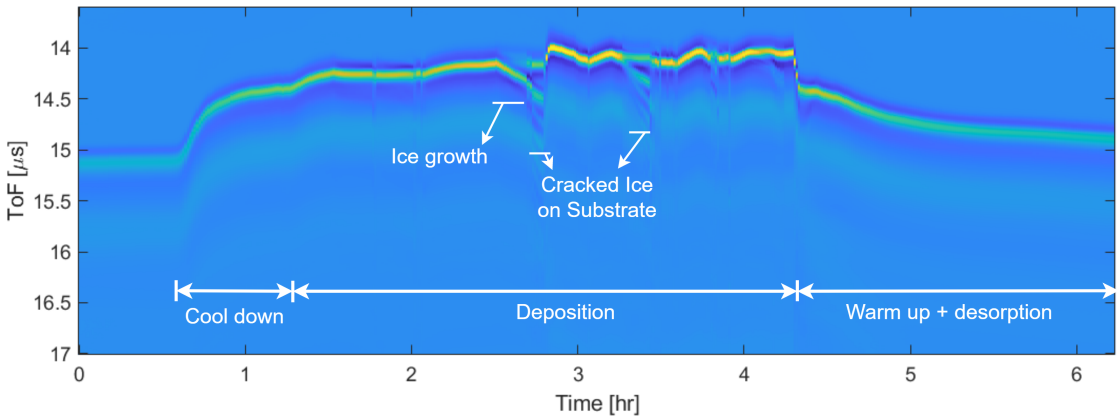


Figure 6.13: B-scan of the experiment on 30/07 with CH_3OH. Different phases in the experiment are marked in the graph. mehtanol ice growth is visible in the deposition. Possibly cracked ice signatures in the signals are visible.

Even though the temperature on the mesa reported a sufficiently low temperature for ice formation at that pressure, the pressure started to rise suddenly to what became the large pressure peak at the 2.8 hour mark. The moment the pressure started to rise, the deposition valve was closed. Nonetheless, the pressure stayed high for a while. This high pressure pushed the methanol to turn liquid which made the methacrylate substrate to have a uniform temperature. It decreased the temperature at the transducer side to an unprecedentedly low level of 200.4K (-72.75°C). Because the decrease of temperature on the transducer side and the increase on the sample holder side, the average temperature of the methacrylate, that is directly proportional to the speed of sound in the methacrylate, did not change much. This effect is translated in the B-scan: It can be seen that roughly the same ToF is maintained after the signature of the ice disappeared even though parts of the methacrylate had a rising/shrinking temperature.

After the transducer temperature dropped significantly, it took a long time for the transducer to have an acceptable temperature again. The heat source in this case is the transducer itself. In operation, it should provide enough heat to remain warm enough, but warming up after being that cold is a struggle.

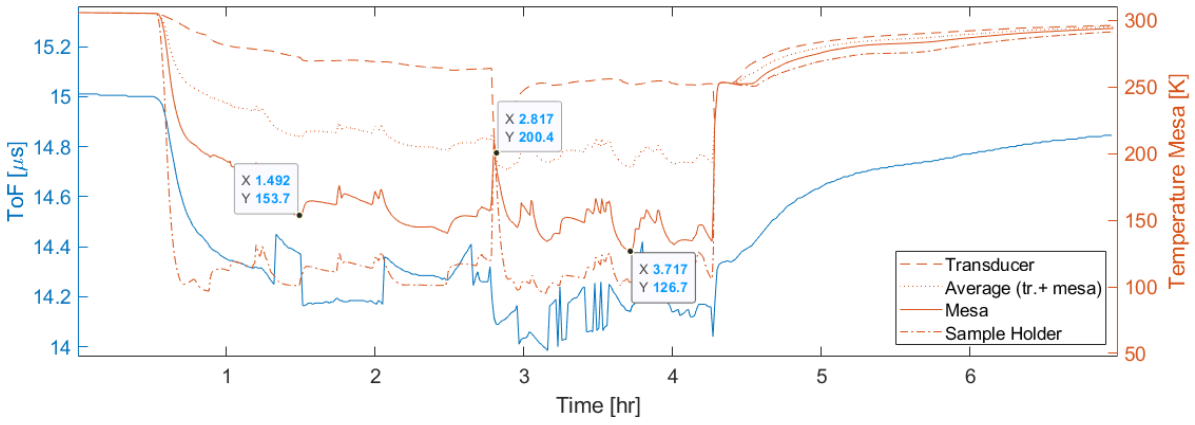


Figure 6.14: Blue: the ToF of the largest peak of the reflection of the ultrasonic pulse throughout the experiment. Orange: Temperatures on the sample holder, the mesa and the transducer. The average of the last two is added as a reference temperature of the methacrylate substrate.

The last deposition was done at the 4 hour mark (see Figure 6.15). Soon after, the liquid N_2 in the tank ran out, causing the system to warm up. Because of its sensitively close triple point, the methanol immediately melted after which the temperature rose and the methanol desorption started. The Desorption of methanol happens significantly fast compared to water ice desorptions.

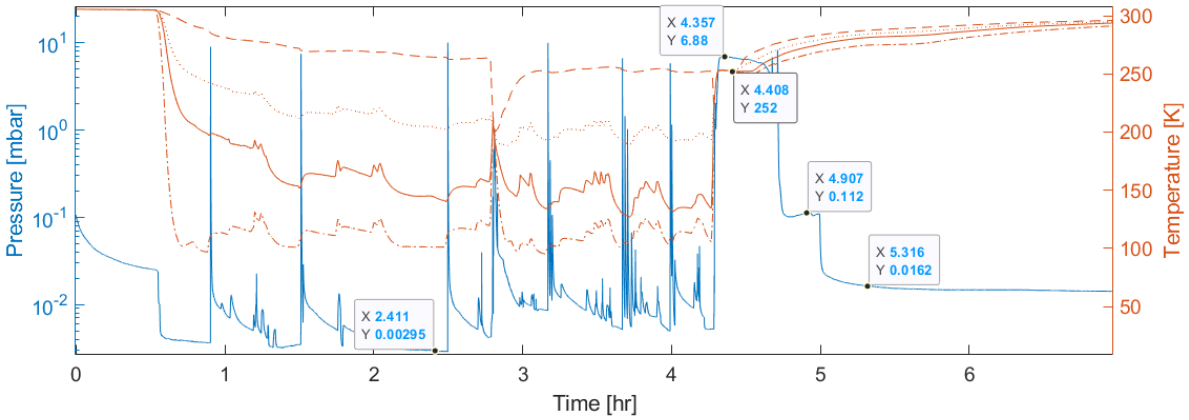


Figure 6.15: Blue: Pressure in the vacuum chamber throughout the experiment. Orange: Temperatures on the sample holder, the mesa and the transducer. The average of the last two is added as a reference temperature of the methacrylate substrate.

To elaborate more on the chain reaction in which all methanol ice melts, the sketch in Figure 6.16 was made for clarification. The temperatures that are present in the sketch are from the experiment on 29/07 the moment right before the chain reaction happened. This shows that the sample holder and the mesa both have a sufficiently low temperature for the grown methanol ice to remain ice. On the back side though, the "base" that connects the mesa with the transducer has a large gradient of temperature ranging from $-123°C$ on the mesa to $-14°C$ at the transducer side. This means that on this piece of methacrylate is a virtual line (freezing line) that represents the boundary on which the methanol can freeze. But slight temperature variations can move this virtual line back and forth. Because the triple point is very close, this methanol ice at the freezing line will start melting and a liquid drop starts to form gradually. When it has become large enough, the drop falls on the inner surface of the vacuum chamber which is at room temperature. This causes the drop to rise in temperature so quickly that it will evaporate which will increase the pressure inside the vacuum chamber and the temperature as a consequence of the high temperature of the vacuum chamber wall.

The conditions created by this first drop are enough for the present ice to melt. Eventually all ice will melt and drop down on the inner side of the vacuum chamber. Removing the methanol from the vacuum chamber takes a while because the methanol needs to evaporate before it can be pumped out of it.

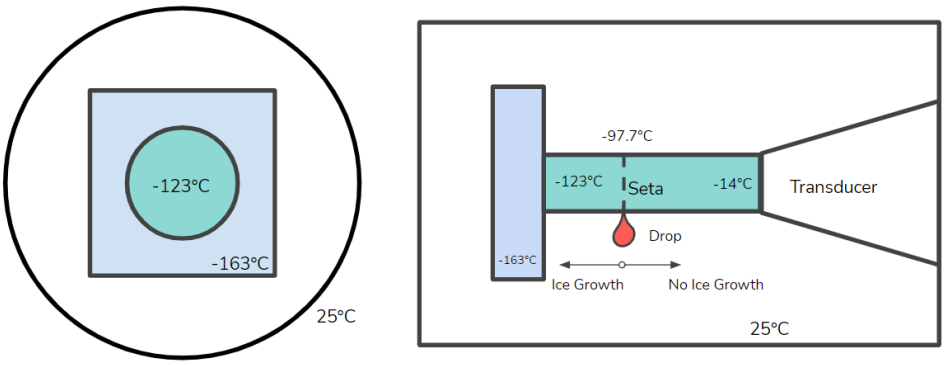


Figure 6.16: Sketch of hypothesis for the cause of the chain reaction in which all deposited mehtanol gets lost. Because of temperature fluctuations during deposition, methanol starts growing at the back of the Seta up to the freezing temperature of methanol. A higher temperature during a later deposition, shifts the line of the freezing temperature, melting the present methanol ice. A methanol drop starts to form and will eventually drop.

6.1.5. Deposition type comparison

After having the experience of 2 experiments without deposition, 5 experiments with water and 3 with methanol, a number of characteristics are different. How they compare exactly is summarized in Table 6.2. In this table the complexity quantifies the level of attention required to end up with desirable results. Without deposition, only the liquid nitrogen tank needs to be refilled. With water you need to open valves and also check the temperature before any new deposition. With mehtanol, everything has to be monitored very closely.

The consumption of liquid nitrogen is influenced by the number of depositions done as well as the type of molecule. Obviously, the experiments without deposition require the least liquid nitrogen which enables the experiment to take a large amount of time. Experiments with H_2O require the most because the thermal capacity of water is large. Depositing mehtanol requires a normal amount of nitrogen, but once all mehtanol turns liquid, a lot of liquid nitrogen is required to cool down the sample holder again. Apart from this, the minimum temperature of the mesa, the usual absorption time and the absorption pressure as well as the risk of losing ice are listed as characteristics for comparison. The risk of losing ice is important because when this happens, a large part of the experiment has to be done over again.

	No Deposition	H_2O Deposition	CH_3OH Deposition
Complexity	Simple	Difficult	Complex
Consumption (Li N_2)	Low	Very High	High
Min. Temp. Mesa [$°C$]	-90.3	-149.85	-155.85
Desorption time [hr]	~ 1	~ 6	~ 0.8
Desorption pressure [mbar]	$\sim 10^{-2} - 10^{-1}$	$\sim 1 - 2$	$\sim 0.1 - 10$
Risk losing ice	No	Low	High

Table 6.2: Comparison of types of experiments in which a distinction is made between deposition substance. The complexity of the experiment type entails the ability to obtain a detectable signal in the ultrasound. Without any deposition, this condition is always satisfied. For water deposition, the ice needs to be grown big enough in order for the ultrasound to have a distinct signature for the present ice. This condition needs to be met for methanol as well on top of the fact that a chain reaction needs to be prevented at all cost during the deposition which makes it more complex than for water ice.

6.2. Improved Vacuum chamber Experiments

Unfortunately, after these last experiments, the methacrylate Seta and the transducer broke down. Most likely this was caused by wear of the thermal stresses and the chemical reactivity of methanol. This event allowed for improvements to impliment on the current design.

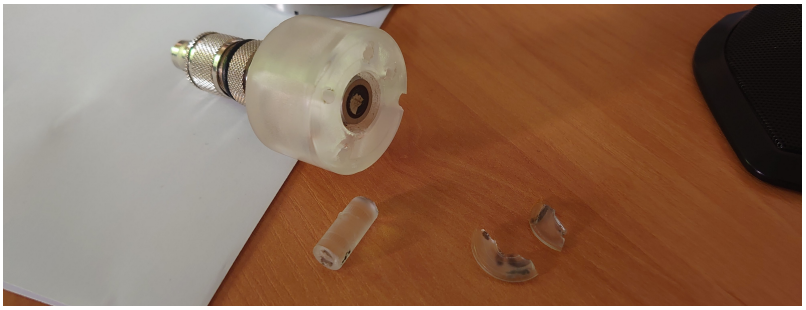


Figure 6.17: Picture of the damage on the components. On the top the transducer can be seen which is inside methacrylate spacing material in order for the transucer to be perfectly aligned. On the bottom the broken pieces of the seta can be seen. The base on the left and the mesa on the right.

6.2.1. Aerograph Experiments

To bridge the time it would take for ordered components for the improved vacuum chamber to arrive, ice would be deposited without a vacuum by means of an aerograph (see Figure 6.18) with a new transducer glued onto a new seta. During this experiment, the temperature did not cool down as much as with the vacuum chamber, but ice could be frozen on the substrate directly and quickly. These experiments were also assisted by the laser vibrometer (see Figure 6.19) in order to see whether it works better without the crystal window of the vacuum chamber being able to reflect part of the beam. Unfortunately, the nature of the ice, which has a snowy morphology, caused the laser beam to scatter early on which made the outcome of the laser vibrometer measurements meaningless. Furthermore, while doing the depositions with the aerograph, the ultrasonic signal barely showed any sign of ice. The reason for this might be that at some point early in the experiment, the thermal stresses between the surface on the boundary between the ice and the methacrylate become too large, which causes a crack. Any ice that is further deposited on top of the present (cracked) ice will not have any influence to the ultrasound in this case. After a number of attempts of aerograph depositions without desirable results, this type of experiment was discarded.




Figure 6.18: Left: The aerograph used for spraying small water drops on the substrate to create ice in the experiments. Right: A small compressor to provide a customizable pressure to the aerograph.

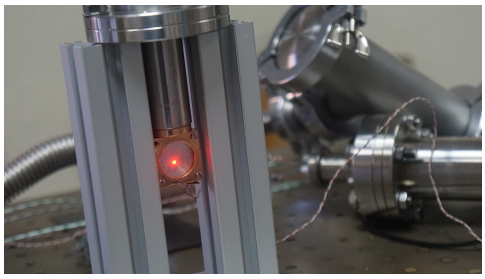
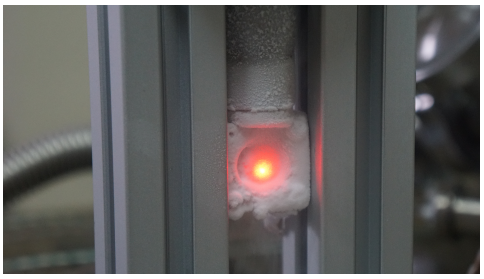



Figure 6.19: Left: The setup with the sample holder, here equipped with an aluminium plate to have an optimal thermal conductivity, before cooling down. The liquid N_2 cryostat is mounted upright on top of the construction. The red dot is the laser spot from the vibrometer Right: The same setup after cooling down and depositing with the aerograph. The scattering of the laser decreased the received signal from the vibrometer.

6.2.2. Improvements to Vacuum Chamber

The breakdown of the seta and transducer in the previous setup was considered an opportunity to improve the vacuum chamber in its capability to grow astrophysical ice analogs in a better way. In the previous setup, the deposition valve was located at the window of the vacuum chamber. This made the flow of water molecules from the front to the back, while in space accretion of molecules happens randomly. Therefore, the new setup has its deposition valve at the bottom of the vacuum chamber. The dimensions of the vacuum chamber were also increased to make it easier to replace parts inside the vacuum chamber when small adjustments or repairs are required. The new transducer that is installed is much smaller in dimension so that it would not need support material as in the previous setup. Furthermore, the bottom of the vacuum chamber is mounted directly on a vibration-dampening table. This will prevent the system from bending down when liquid N_2 is poured in the cryostat in order to get better results with the laser vibrometer. A second improvement to decrease vibrations in the vacuum chamber is the elongation of the deposition valve. By making the tube that connects the deposition valve with the vacuum chamber longer, the vibrations that arise when the valve is opened manually will not cause vibrations of the vacuum chamber. Lastly, a deposition tube/reservoir with a larger volume was connected in order to be able to continue an experiment with less refilling of the deposition tube.

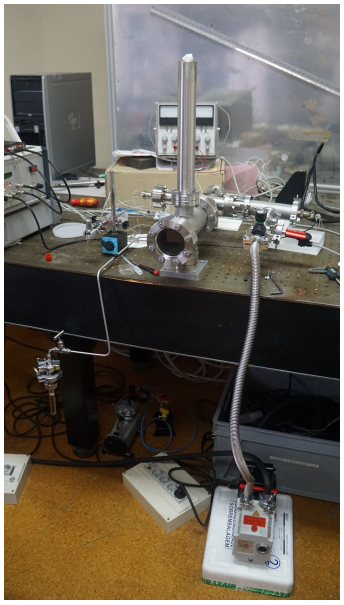


Figure 6.20: Improved vacuum chamber mounted on a vibration-dampening table.

6.2.3. New Obstacles and Fixing Attempts

Despite the effort to improve the design of the first small vacuum chamber, it turned out to be hard to grow ice on the substrate, especially at the center where the ultrasonic waves travel to. This is why a series of solutions were proposed to improve ice growth. These solutions are summarized below.

Aluminium tape

To improve the thermal conductivity, a piece of aluminium tape was used and it connected the mesa with the sample holder (see left in Figure 6.21). The aluminium conducted the cold from the copper sample holder well and ice grew everywhere on the tape. Unfortunately, the tape was not a good conductor of the ultrasonic signal, which made the ice undetectable with ultrasound. As a consequence, the idea of the tape remained, but with a hole inside. The tape provides cooling for the mesa of the substrate in order for the ice to be able to grow in the center, where the ultrasonic pulses are able to pass trough (see middle and right picture in Figure 6.21). After ice deposition, this configuration still had a hole in the center.

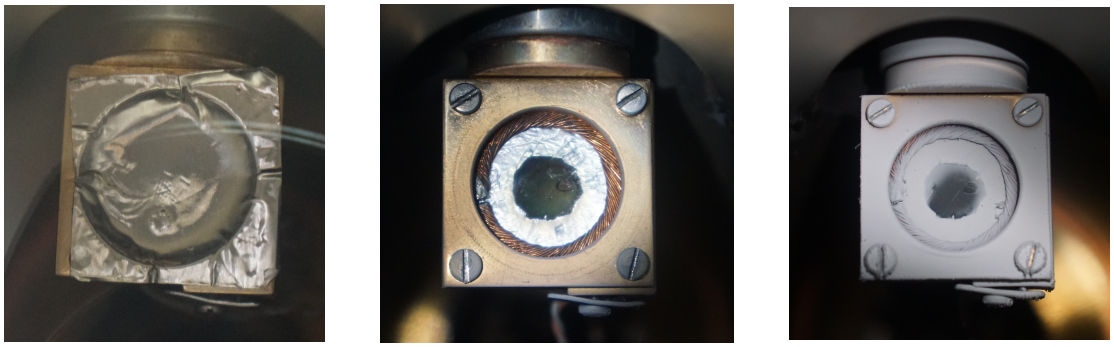


Figure 6.21: Left: Aluminium tape used to increase thermal conductivity. Middle and right: Aluminium tape with a hole inside taped directly on the mesa before mounting in the sample holder.

Aluminium dish

By using an aluminium dish as mesa, the thermal conductivity of the mesa would be sufficient. To make sure the ice would be detectable with ultrasound, the dish had to have a thickness of at least $3mm$. This is because the speed of sound in aluminium is a multitude of the one of methacrylate which results in plenty reflections with the ToF the pulse needs to travel through the aluminium acting as a separator of these reflections. By separating the reflections caused by the aluminium, the signature of the ice in the ultrasound can become visible between these reflections. The methacrylate was mounted to the aluminium with an adhesive, but once the sample holder was cool at the start of an experiment, a metallic "click"-sound was heard after which the reflections of the aluminium disappeared. From this could be concluded that the contraction of the aluminium as a reaction to its cold temperature caused sufficient shear stresses in the adhesive for it to crack. After this incident a more flexible adhesive was used which resulted in the same type of crack.

Silver paint + Aluminium tape

The next option to stimulate ice growth in the center of the mesa is by applying a silver paint. This allows a thin layer of highly thermal conductive paint that will cool the mesa down sufficiently. To increase the thermal conductivity even more, the aluminium tape with a hole inside is applied on top of the painted mesa. From the pictures in Figure 6.22 can be seen that ice forms everywhere on the surface of the mesa, but a thinner ice is observed at the center. Eventually also the silver paint cracked because of its contraction.



Figure 6.22: Silver painted mesa with aluminium tape with a hole inside.

Gold coating

The idea of a gold coating on the mesa arose together with the silver paint idea since they share the same principle. The coating has a number of layers in order for the thermal conductivity to be optimal. From the pictures in Figure 6.23 can be seen that it certainly helped with the ice growth, although the ice grown in the center of the mesa is still too thin to be noticed. Because of contraction of the gold coating, cracks occurred in the gold coating. Because the coating has a very strong bonding with the surface of the methacrylate, the crack did not happen between these two materials, but across an isothermal circle on the surface, separating the center of the surface of the mesa from the outer boundaries of the mesa that are in contact with the sample holder.



Figure 6.23: Sample holder with gold coated mesa. The left most picture is early in the experiment where the temperature gradient marks the gold coating with a color gradient. In the two middle pictures can be seen in what pattern the ice freezes onto the mesa which eventually results in the last picture. Note that even here, the ice seems more transparent and thus thinner at the center of the mesa.

Regular tape

Since the deposition flow of water molecules points directly to the bottom of the sample holder, where ice immediately starts to grow, this growth is thought to be a consequence of the motion of the molecules. Because the suction of the vacuum pump is towards the back of the vacuum chamber and the flow of deposition molecules comes from the bottom of the vacuum chamber, the motion of the molecules in front of the substrate is thought to be negligible. This might be the reason why plenty of ice grows on the sample holder while the ice takes a long time to grow a thin layer on the methacrylate mesa. A piece of regular tape (see on the bottom right corner of Figure 6.24) is used to cover the access to the vacuum chamber from the bottom and guide the deposition gasses towards the front of the vacuum chamber. The water molecules will change direction and move towards the back of the vacuum chamber. This motion will be perpendicular to the surface of the methacrylate which initiates a fast growth of ice with an almost-equal distribution.

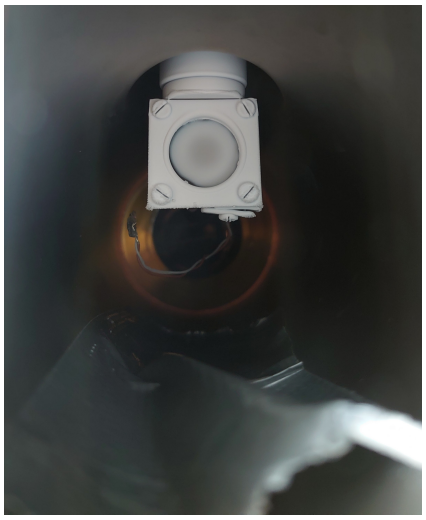


Figure 6.24: Changing the direction of the flow of water molecules from the bottom to the front by means of a piece of regular tape, visible on the bottom in the picture. The tape guides the flow towards the front, after which it will change direction since the pump suction is in the back.

Smaller outer diameter

A last design change that was considered is a reduction in diameter of the mesa. Having a mesa with a smaller diameter is beneficial to decrease the temperature in the center of the methacrylate substrate. This will allow the cold copper plates of the sample holder to bring the cold temperature from the cryostat closer to the center, resulting in better conditions for ice growth on the methacrylate. Pictures of this experiment are shown in Figure 6.25. The first picture from the left was taken minutes after the deposition valve was opened. This fast deposition is the result of the guided flow of water molecules by the tape discussed in the previous section that was still present during this experiment. The second picture from the left is when the ice thickness reached an equilibrium (after hours with the deposition valve opened). The third and last picture shown is from the desorption that happened after the deposition valve was closed and the liquid N_2 ran out. The pictures show that the desorption starts in the center, caused

by the heat transmitted by the transducer. The ice thickness in the deposition equilibrium picture should have been thick enough to be noticed by the ultrasonic measurements, but it was not detected. Therefore the ultimate conclusion after having tried a number of different configurations that eventually solved the thermal conductivity struggle is that the ice created inside the vacuum chamber is not compact enough to transmit the ultrasounds. The previous iteration of the vacuum chamber allowed for this because the flow of water molecules was faster, thus creating a more compact ice that is better detectable.



Figure 6.25: Sample holder for substrate with smaller diameter to increase cooling capacity near the center. The left picture was taken a minute after the deposition valve was opened. The second picture to the left was taken at its deposition equilibrium. The two pictures on the right are from the desorption phase after the deposition.

6.2.4. Successful experiments

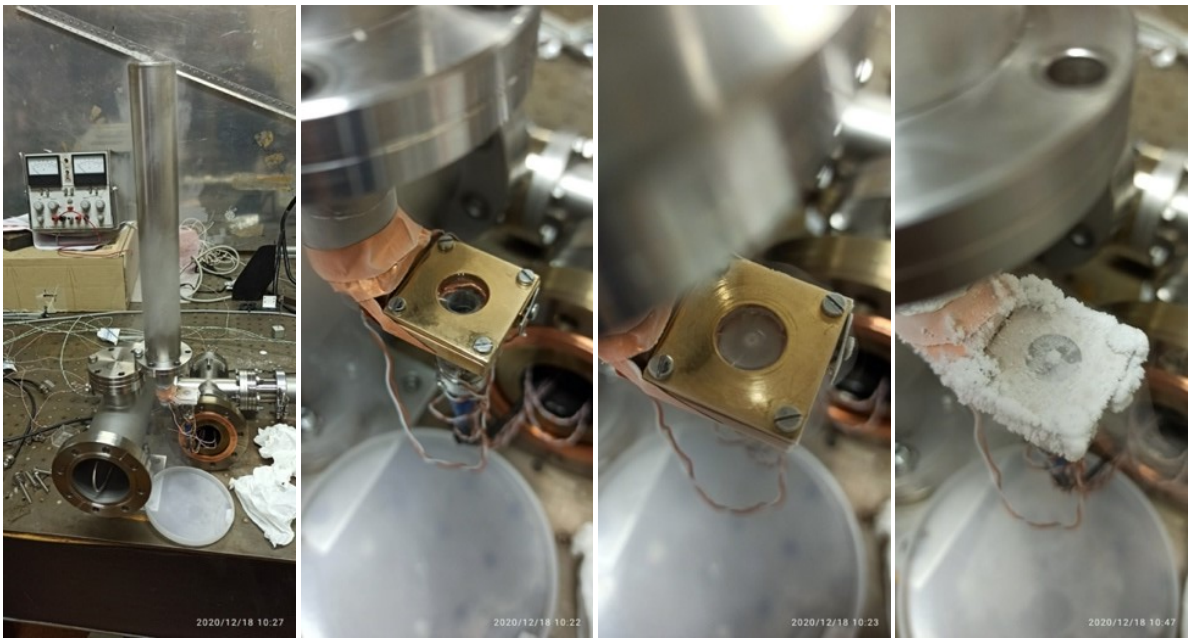


Figure 6.26: The first picture shows the new configuration with the horizontal sample holder out of the vacuum chamber. The second picture shows the sample holder with water put directly on the substrate. The third picture is while cooling. The water present freezes in one minute. The last picture is taken several minutes later. Atmospheric water vapor freezes on the cold surfaces of the sample holder.

To verify that compact ice can be measured by this sample holder, the setup was reconfigured. A thermally conductive part was made that allowed the sample holder to remain horizontal. In such a way, liquid water can be added on top of the mesa after which it will freeze by the cryostat (see Figure 6.26). This is the first time the ultrasound as a function of temperature is measured for this large range of temperature. The lowest temperatures at which ultrasound in ices have been measured comes from the low temperatures on Earth (Antarctica and Greenland) that usually go as low as $-60°C$ while the cryostat at atmospheric pressure allows for temperatures that go below $-100°C$ and much lower ($-149°C$) after the vacuum is applied. Future experiments with this setup will reveal the speed of sound in other compounds such as methanol, ethanol,

propanol, ... Since this configuration was finished after the end of my stay in Madrid, colleagues performed the experiments and shared their findings.

Three types of experiments were done: without deposition, with water deposition and with alcohol (96%) deposition. The experiment without deposition is to understand how the contraction of the methacrylate behaves and the one with water is to prove that compact water ice is detectable with the current setup.

To calculate the speed of sound, the ToF in the ice is extracted from the ultrasonic data and the thickness of the ice was measured to be $2mm$. To help understand how the ToF is extracted from the ultrasonic data, the B-scan of the experiment with water is shown in Figure 6.27. The x-axis represents the time in the experiment while the y-axis shows the ToF in $s * 10^{-5}$. The different phases the experiment encountered are marked at the bottom of the figure, going from the "Liquid cooling down" till the "Liquid water warming up"-phase. In this figure can be seen that after the liquid cooled down, the freezing happened very quickly, after which the ultrasonic signal of the top surface of the ice appeared. Once the water is frozen, the ToF keeps decreasing which is the effect of the contracting methacrylate and the increase in speed of sound as a consequence of the decrease in temperature. When the liquid N_2 tank runs out, the system starts warming up (in the "Ice slowly warming up"-phase) after which the ice will melt and the ultrasonic signal of the ice will disappear (in the "slow melting"-phase). Because the ice became liquid, the ultrasonic signature of the water returned. Extracting the ToF in the ice is done by taking the difference in time between the ultrasonic pulses of the methacrylate surface and the top surface of the ice which is shown in the figure as the distance covered by the vertical arrows.

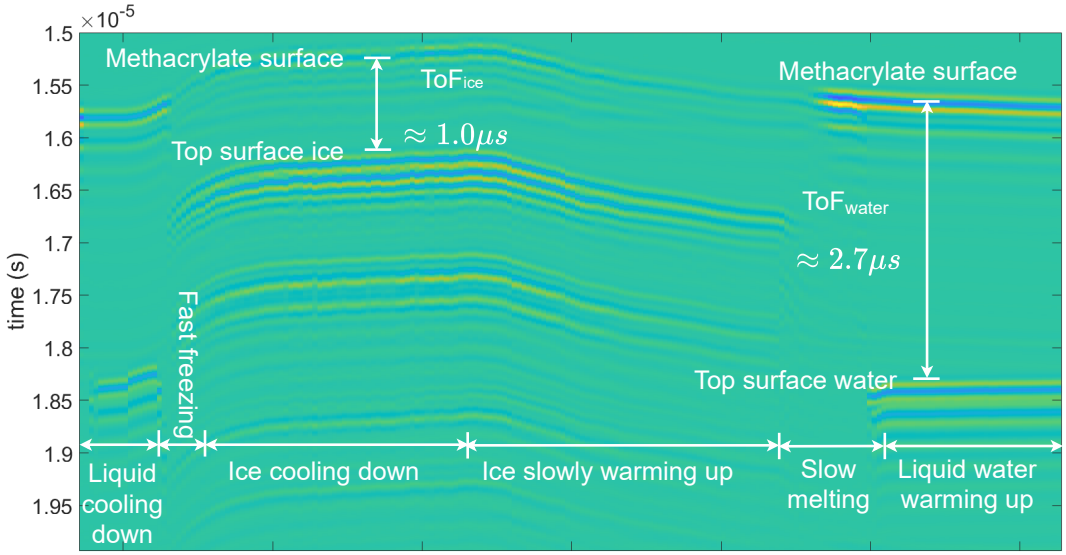


Figure 6.27: B-scan of the freezing experiment of the liquid water. The x-axis represents the time in the experiment while the y-axis is the ToF presented in $s * 10^{-5}$ with the different phases of the experiment marked below (from "liquid cooling down" till "liquid warming up"). The determination of the ToF is graphically visualized for the frozen ice and the liquid water of $2mm$. Note that the displayed values of $ToF_{ice} \approx 1.0\mu s$ and $ToF_{water} \approx 2.7\mu s$ are rough estimations. (Credit: Cristóbal Gonzalez Diaz)

From the plot in Figure 6.28, that entails the experiment with the growth of water ice, can be seen that it has a rising, linear trend for a decreasing temperature with slope $\frac{dc_{(T)}}{dT} = -2.5494 m/(s°C)$ and an offset at $0°C$ of $c_{(T=0°C)} = 3616.86 m/s$. In the paper of Vogt et al. [39], the ultrasonic speed of sound in 'bubble-free' or compact water ice is documented. This paper makes a distinction between "laboratory" experiments and "in-situ" (Antarctica and Greenland). The longitudinal speed of sound in these laboratory experiments was measured between $-20°C$ and $0°C$ whereas the in-situ experiments were done in the temperature range of $-16°C$ and $-58°C$. When comparing the slopes of the experiment done with the the $c_{(T)}$-fittings from this paper, which are $\left(\frac{dc_{(T)}}{dT}\right)_{In-situ} = -2.30 m/(s°C)$ and $\left(\frac{dc_{(T)}}{dT}\right)_{Lab} = -2.80 m/(s°C)$, can be stated that the found slope of $\frac{dc_{(T)}}{dT} = -2.5494 m/(s°C)$ lies in between those. By comparing the offsets, which are $c_{(T=0°C)In-situ} = 3798.00 m/s$ and $c_{(T=0°C)Lab} = 3838.00 m/s$, one can see that the offset obtained from the experimental data plotted in Figure 6.28 is at least 4.8% lower than the Vogt et al. work.

The reason for this discrepancy is unknown, but the speed at which the sample holder cools down might have a significant influence on the synchronicity of the temperature measurement that was done while cooling down and the temperature of the water itself. Because of the high thermal capacity of water, it resists to cool down while the rest of the sample holder is already below freezing temperatures. The "thermal inertia" that is present in this fast-cooling experiment causes the temperature sensor, that is located at the back of the substrate and therefore not in direct contact with the water, to measure slightly different values (lower values during cool-down and higher values during the warm-up phase).

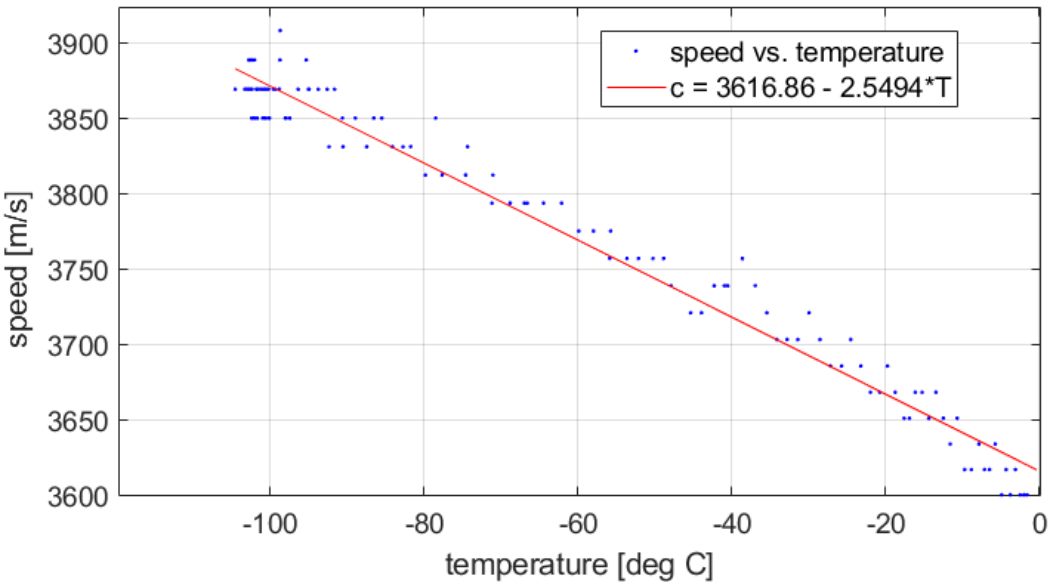


Figure 6.28: Speed of sound measured in ice made from freezing of liquid water for a range of temperatures. The blue dots represent single datapoints during the experiment, the red line is the trendline of the set of dots. (Credit: Cristóbal Gonzalez Diaz)

7

Concluding remarks and applications

7.1. Concluding remarks

This thesis is an experimental feasibility study about the detectability of porosity in planetary and cometary ices. The experiments performed took place inside a vacuum chamber because this best represents the conditions of ice growth in outer space. In the vacuum chamber, the sample holder that carries the substrate of methacrylate is mounted on the cryostat which cools down to temperatures close to the one of liquid nitrogen. The methacrylate substrate is a single part that consists of a dish (on which the measured ice grows) and an extending rod at the back of the dish. The main function of the methacrylate is to provide thermal insulation between the cold of the ice and the ultrasonic transducer which is directly mounted on the extension rod of the substrate. Ultrasonic pulses travel through the methacrylate substrate after which a reflected signal travels back. Ice growth on the substrate was thought of to leave a signature in the ultrasonic response since the pulse would travel through the ice after which a reflection would travel back into the methacrylate to end up on the transducer. This would result in two distinct peaks in an ultrasonic readout during the experiments.

The findings of the experiments prove that ices grown in vacuum chambers are too "fluffy" to leave signatures in the ultrasonic measurements. The ice growth in vacuum chambers make the water molecules freeze in a random way on the surface of the substrate. This phenomenon makes the ice less dense and less stiff than the ice on Earth and leads to a high attenuation encountered by propagating ultrasonic pulses.

Experiments with water drops with- and without bubbles (that represent a certain amount of porosity) show that the influence of the bubbles is present in the ultrasound. The bubbles make the signal "noisy" by reflecting the ultrasonic pulse in all directions in the drop. Eventually the locations of the bubbles and the top surface of the drops could be determined in the ultrasonic data. Prior knowledge on the height of the drop is crucial to ensure the right reflected pulse is selected. It is easy to mistake the reflection coming from a bubble with the one coming from the top of the drop.

At last, the setup of the vacuum chamber has been converted in such a way that the sample holder is held horizontal which allowed to grow ices without vacuum directly on the methacrylate substrate. Since this ice is compact, it is detectable by ultrasound and from the measurements, a linear trend for a decreasing temperature with slope $\frac{dc_{(T)}}{dT} = -2.5494 m/(s°C)$ and an offset at $0°C$ of $c_{(T=0°C)} = 3616.86 m/s$ has been found for a temperature range from $0°C$ to $-100°C$.

The versatility of the small vacuum chamber makes it attractive to be used in a variety of future experiments. Its rather simple build allows for quick ice growth compared to large vacuum chambers, but when growing ices in the vacuum, the use of ultrasound is not recommended. By converting the setup, ices can be measured with ultrasound at atmospheric pressure. Therefore, the speed of sound for a variety of compounds can be characterized for temperatures that can go down to $-100°C$.

7.2. Possible applications derived from this thesis

Probe on Icy Moon:

When a probe travels through a thick layer of ice, ultrasound can guide the probe by revealing cracks and surfaces on the go. The reflection of the ultrasonic signal which can be interpreted as a boundary of the ice the probe is traveling through. Such a boundary indicates the nearby presence of liquid water (possibly an ocean), an ice-cave or a small crack in which ice layers are separated. No reflected peak would mean that there is still a large amount of ice in the direction of the wave propagation. When approaching a surface in the ice that can be caused by a crack or a subsurface ocean, a peak would appear in the ultrasonic response that can be translated into a distance. This application works similar to the way parking sensors work that are embedded in the bumpers of modern cars.

Quick check for sample retrieval:

When considering sample retrieval missions (on comets, the Moon, Mars, ...) it might be interesting to know whether or not the soil in which will be drilled is homogeneous. If this would be the case, a hole would not have to be drilled very deep. Using ultrasound, heterogenic soils can be found which allows for a greater variety of compounds in the sample.

7.3. General applications

Extraterrestrial Submarine:

When a submarine would move inside the ocean of an icy moon or planet, ultrasound can be used for the detection of obstacles as well as for measuring distance and velocity when docking or carefully approaching a surface of interest. The velocity and direction of currents in the ocean could be detected as well. With this information, the submarine can change its relative angle with the current to get desired aerodynamic properties. Knowing these currents is also advantageous in anticipating motion caused by the currents that are present.

Crack detection/delamination in composites:

On Earth, ultrasound is used frequently to perform inspections especially on composites because they almost show no wear. Since the next generation of manned space vehicles would be re-usable, these inspections could take place within the missions themselves. Defects can be repaired, or parts can be replaced accordingly.

Ice detection on aircraft wings:

Aircraft wings embedded with ultrasonic transducers can allow for the detection of ice formation. This could give information about the thickness of the ice and the type of ice (glaze-like ice or rime-like ice) [19] grown on the airfoil for which ice-type specific anti-/de-icing systems can be developed that allows for a reduction in de-icing costs and safer flight operations.

Bibliography

[1] S. Amari, P. Hoppe, E. Zinner, and R. S. Lewis. Interstellar SiC with unusual isotopic compositions - Grains from a supernova? *apjl*, 394:L43–L46, August 1992. doi: 10.1086/186468.

[2] MAX PLANCK INSTITUTE FOR ASTRONOMY. Low-mass star formation. URL http://www.mpia.de/en/PSF/research/low-mass. [cited 23-05-2019].

[3] Eva Graulund Bøgelund. A molecular journey: Tales of sublimating ices from hot cores to comets, 2019.

[4] A. C. A. Boogert, P. A. Gerakines, and D. C. B. Whittet. Observations of the icy universe. *araa*, 53:541–581, August 2015. doi: 10.1146/annurev-astro-082214-122348.

[5] A.C. Adwin Boogert, Perry A. Gerakines, and Douglas C.B. Whittet. Observations of the icy universe. *Annual Review of Astronomy and Astrophysics*, 53(1):541–581, 2015. doi: 10.1146/annurev-astro-082214-122348. URL https://doi.org/10.1146/annurev-astro-082214-122348.

[6] S. Cazaux, J.-B. Bossa, H. Linnartz, and A. G. G. M. Tielens. Pore evolution in interstellar ice analogues. Simulating the effects of temperature increase. *aap*, 573:A16, January 2015. doi: 10.1051/0004-6361/201424466.

[7] Martin Chaplin. Water vibrational spectrum, April 2019. URL http://www1.lsbu.ac.uk/water/water_vibrational_spectrum.html. [cited 26-06-2019].

[8] L. Dones, R. Brasser, N. Kaib, and H. Rickman. Origin and Evolution of the Cometary Reservoirs. *ssr*, 197:191–269, December 2015. doi: 10.1007/s11214-015-0223-2.

[9] J. A. Fernandez and W.-H. Ip. Some dynamical aspects of the accretion of Uranus and Neptune - The exchange of orbital angular momentum with planetesimals. *icarus*, 58:109–120, April 1984. doi: 10.1016/0019-1035(84)90101-5.

[10] Mikio Fukuhara and Asao Sampei. Low-temperature elastic moduli and internal dilational and shear friction of polymethyl methacrylate. *Journal of Polymer Science Part B: Polymer Physics*, 33(12):1847–1850, 1995. doi: https://doi.org/10.1002/polb.1995.090331214. URL https://onlinelibrary.wiley.com/doi/abs/10.1002/polb.1995.090331214.

[11] R. T. Garrod and E. Herbst. Formation of methyl formate and other organic species in the warm-up phase of hot molecular cores. *aap*, 457:927–936, October 2006. doi: 10.1051/0004-6361:20065560.

[12] R. T. Garrod, V. Wakelam, and E. Herbst. Non-thermal desorption from interstellar dust grains via exothermic surface reactions. *aap*, 467:1103–1115, June 2007. doi: 10.1051/0004-6361:20066704.

[13] W. F. Giauque and C. J. Egan. Carbon dioxide. the heat capacity and vapor pressure of the solid. the heat of sublimation. thermodynamic and spectroscopic values of the entropy. *The Journal of Chemical Physics*, 5(1):45–54, 1937. doi: 10.1063/1.1749929. URL https://doi.org/10.1063/1.1749929.

[14] E. Herbst and E. F. van Dishoeck. Complex Organic Interstellar Molecules. *araa*, 47:427–480, September 2009. doi: 10.1146/annurev-astro-082708-101654.

[15] Sergio Ioppolo. Surface formation routes of interstellar molecules: A laboratory study, 2010.

[16] A. Johansen, J. Blum, H. Tanaka, C. Ormel, M. Bizzarro, and H. Rickman. The Multifaceted Planetesimal Formation Process. *Protostars and Planets VI*, pages 547–570, 2014. doi: 10.2458/azu_uapress_9780816531240-ch024.

[17] H. F. Levison, A. Morbidelli, C. Van Laerhoven, R. Gomes, and K. Tsiganis. Origin of the structure of the Kuiper belt during a dynamical instability in the orbits of Uranus and Neptune. *icarus*, 196:258–273, July 2008. doi: 10.1016/j.icarus.2007.11.035.

[18] Jack J. Lissauer and Imke de Pater. Fundamental planetary science: Physics, chemistry and habitability, 2013.

[19] Yang Liu, Leonard Bond, and Hui Hu. Ultrasonic-attenuation-based technique for ice characterization pertinent to aircraft icing phenomena. *AIAA Journal*, 55:1–8, 01 2017. doi: 10.2514/1.J055500.

[20] Stéphanie Lucas, Daniel Ferry, Benjamin Demirdjian, and Jean Suzanne. Vapor pressure and solid phases of methanol below its triple point temperature. *The Journal of Physical Chemistry B*, 109(38): 18103–18106, 2005. doi: 10.1021/jp053313v. URL https://doi.org/10.1021/jp053313v. PMID: 16853325.

[21] D. Lynden-Bell and J. E. Pringle. The evolution of viscous discs and the origin of the nebular variables. 168:603–637, September 1974. doi: 10.1093/mnras/168.3.603.

[22] G M. Muñoz Caro, Jose Martin Gago, Celia Rogero, A Jiménez-Escobar, Jesús Sobrado, C Atienza, and S Puertas. *The Interstellar Astrochemistry Chamber (ISAC)*, page 17. Centro de Astrobiologia, CSIC-INTA, 05 2010. doi: 10.1142/9789812838162_0040.

[23] Kevin Martin and David Spinks. Measurement of the speed of sound in ethanol/water mixtures. *Ultrasound in medicine & biology*, 27:289–91, 03 2001. doi: 10.1016/S0301-5629(00)00331-8.

[24] R. Martín-Doménech, G. M. Muñoz Caro, J. Bueno, and F. Goesmann. Thermal desorption of circumstellar and cometary ice analogs. *aap*, 564:A8, April 2014. doi: 10.1051/0004-6361/201322824.

[25] MIT. Material property database - material: Pmma, May 2020. URL http://www.mit.edu/~6.777/matprops/pmma.htm. [cited 30-05-2020].

[26] M. Molero-Armenta, Ursula Iturrarán-Viveros, S. Aparicio, and M.G. Hernández. Optimized opencl implementation of the elastodynamic finite integration technique for viscoelastic media. *Computer Physics Communications*, 185(10):2683–2696, 2014. ISSN 0010-4655. doi: https://doi.org/10.1016/j.cpc.2014.05.016. URL https://www.sciencedirect.com/science/article/pii/S0010465514001702.

[27] A. Morbidelli. A coherent and comprehensive model of the evolution of the outer Solar System. *Comptes Rendus Physique*, 11:651–659, November 2010. doi: 10.1016/j.crhy.2010.11.001.

[28] James Mortimer, Christophe Lécuyer, François Fourel, and James Carpenter. D/h fractionation during sublimation of water ice at low temperatures into a vacuum. *Planetary and Space Science*, 158:25–33, 2018. ISSN 0032-0633. doi: https://doi.org/10.1016/j.pss.2018.05.010. URL https://www.sciencedirect.com/science/article/pii/S003206331830059X.

[29] G. M. Muñoz Caro, U. J. Meierhenrich, W. A. Schutte, B. Barbier, A. Arcones Segovia, H. Rosenbauer, W. H.-P. Thiemann, A. Brack, and J. M. Greenberg. Amino acids from ultraviolet irradiation of interstellar ice analogues. *nat*, 416:403–406, March 2002. doi: 10.1038/416403a.

[30] NIST. Ethanol - triple point temperature, September 2018. URL https://webbook.nist.gov/cgi/cbook.cgi?ID=C64175&Units=SI&Type=TTRIPLE. [cited 11-03-2021].

[31] Karin Ingegerd Öberg. Complex processes in simple ices: Laboratory and observational studies of gas-grain interactions during star formation, 2009.

[32] Rolf Prydz and Robert D. Goodwin. Experimental melting and vapor pressures of methane. *The Journal of Chemical Thermodynamics*, 4(1):127–133, 1972. ISSN 0021-9614. doi: https://doi.org/10.1016/S0021-9614(72)80016-8. URL https://www.sciencedirect.com/science/article/pii/S0021961472800168.

[33] Hilke E. Schlichting and Re'em Sari. RUNAWAY GROWTH DURING PLANET FORMATION: EXPLAINING THE SIZE DISTRIBUTION OF LARGE KUIPER BELT OBJECTS. *The Astrophysical Journal*, 728(1):68, jan 2011. doi: 10.1088/0004-637x/728/1/68. URL https://doi.org/10.1088%2F0004-637x%2F728%2F1%2F68.

[34] D. Semenov and D. Wiebe. Chemical Evolution of Turbulent Protoplanetary Disks and the Solar Nebula. *apjs*, 196:25, October 2011. doi: 10.1088/0067-0049/196/2/25.

[35] N. I. Shakura and R. A. Sunyaev. Black holes in binary systems. Observational appearance. 24:337–355, 1973.

[36] C. J. Shen, J. M. Greenberg, W. A. Schutte, and E. F. van Dishoeck. Cosmic ray induced explosive chemical desorption in dense clouds. *aap*, 415:203–215, February 2004. doi: 10.1051/0004-6361:20031669.

[37] Martin H Skjelvareid. Synthetic aperture ultrasound imaging with application to interior pipe inspection. 2012.

[38] Daniel R. Stull. Vapor pressure of pure substances. organic and inorganic compounds. *Industrial & Engineering Chemistry*, 39(4):517–540, 1947. doi: 10.1021/ie50448a022. URL https://doi.org/10.1021/ie50448a022.

[39] Christian Vogt, Karim Laihem, and Christopher Wiebusch. Speed of sound in bubble-free ice. *The Journal of the Acoustical Society of America*, 124:3613–8, 01 2009. doi: 10.1121/1.2996304.

[40] Wayne Wilson and David Bradley. Speed of sound in four primary alcohols as a function of temperature and pressure. *Journal of the Acoustical Society of America*, 36(2):333–337, January 1964. ISSN 0001-4966. doi: 10.1121/1.1918956.

A

Complete Roadmap of the Project

Figure A.1 shows how the main goal of the project will be achieved. It serves as a guideline for the experiments that are performed. This roadmap is mainly elaborated on in Chapter 3.

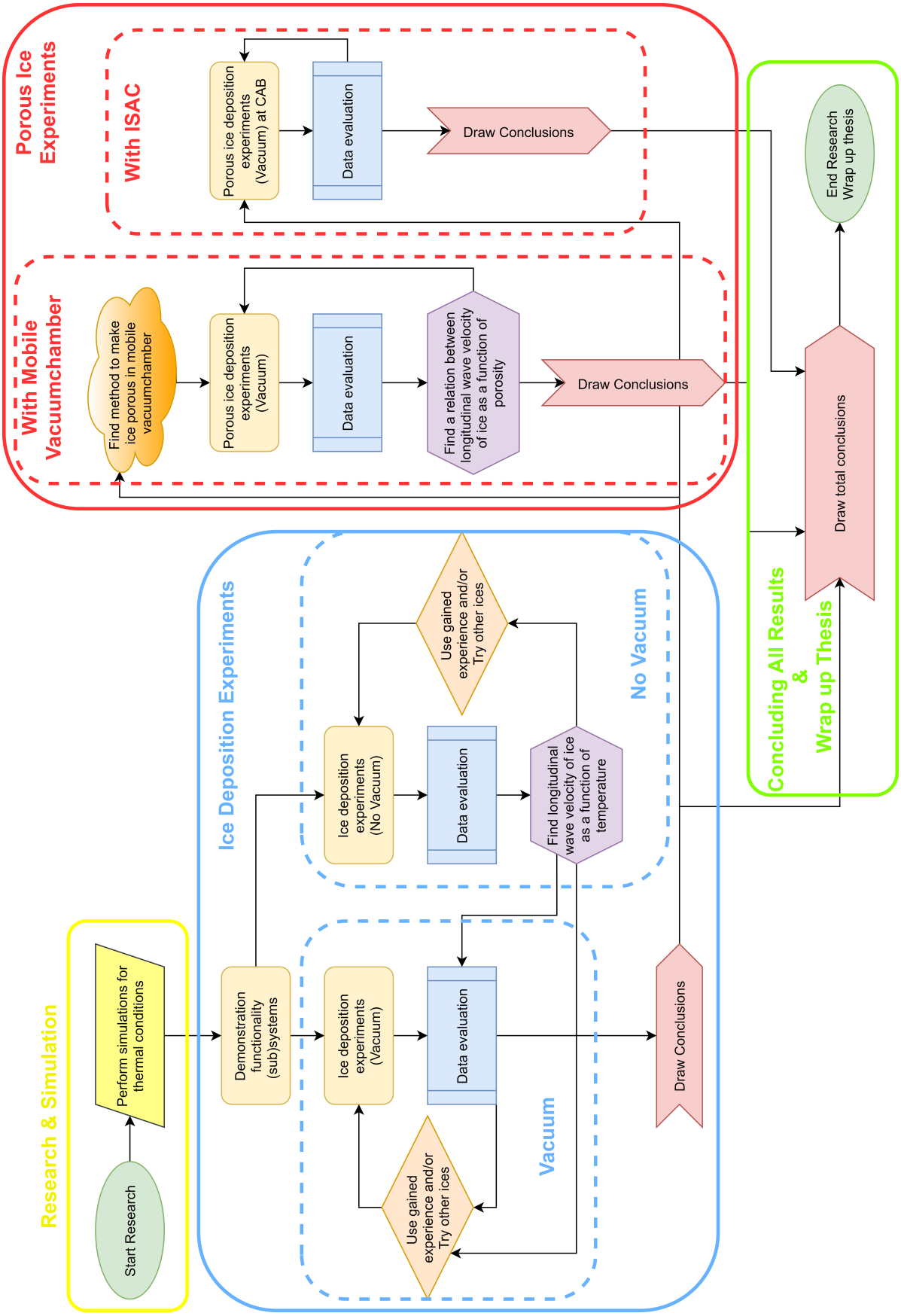


Figure A.1: This project roadmap presents approach of the project and the different sets and types of experiments that are necessary to proceed to the next ones in order for all results to be concluded eventually.

B

Data from drop experiments

This chapter entails the results from all drop experiments. The compact, porous and alternative ice drop experiments are grouped together in the next sections. For every drop experiment, the height of the drop is derived from images. The ToF is derived as described in Chapter 5 from the ultrasonic echos. The speed of sound in the drop is derived from the height and the ToF of the drop. Since the received signal is the reflection that happens on top of the drop, the ultrasonic signal travels twice the distance of the height before it is measured. Finally, values that differ much from the literature values were checked again. When this is caused by an obvious reason for which this value should not be considered valid to take into consideration with the calculation of the statistical values (mean and standard deviation), these values are considered outliers.

B.1. Compact Ice drop experiments

	Height [mm]		Time of Flight [μs]			Speed of Sound [m/s]			Outliers
	Water	Ice	$ToF_{R.T.}$	$ToF_{0°C}$	$ToF_{-18°C}$	$c_{R.T.}$	$c_{0°C}$	$c_{-18°C}$	
Ice Drop 1	1.59	-	2.00	2.03	0.72	1594.89	1571.32	-	
Ice Drop 2	1.26	-	1.73	1.79	-	1456.88	1408.04	-	
Ice Drop 3	1.77	-	2.31	-	-	1533.49	-	-	
Ice Drop 4	0.65	-	-	-	-	-	-	-	
Ice Drop 5	2.06	2.67	2.74	2.68	-	1502.43	1536.07	-	
Ice Drop 6	1.54	-	1.93	-	-	1598.65	-	-	
Ice Drop 7	1.73	2.11	2.20	-	-	1570.25	-	-	
Ice Drop 8	2.47	-	3.25	-	-	1522.95	-	-	
Ice Drop 9	2.12	2.70	2.79	-	1.25	1518.03	-	4313.12	x
Ice Drop 10	-	3.23	-	2.75	1.53	-	-	4226.39	
Ice Drop 11	2.32	2.92	3.21	-	1.53	1442.86	-	3812.64	
Ice Drop 14	2.50	3.15	3.26	-	1.64	1531.14	-	3841.46	
Ice Drop 18	2.57	2.56	3.37	2.90	1.25	1527.29	1766.97	4108.74	x
Ice Drop 24	2.84	3.02	3.99	3.18	1.59	1425.06	1901.09	3814.17	x
Ice Drop 25	3.14	2.99	4.27	3.01	1.52	1472.45	1988.04	3949.83	x
Ice Drop 27	-	2.92	-	2.85	0.94	-	2051.28	6252.57	x
Ice Drop 28	2.23	2.51	3.26	3.51	-	1370.85	1429.06	-	
Ice Drop 29	2.45	3.54	4.37	4.94	1.13	1121.18	1433.23	6287.10	x
Ice Drop 35	-	4.39	4.21	4.29	-	-	1380.09	-	
Ice Drop 36	1.13	2.04	1.58	2.02	-	1436.13	2020.56	-	x
Ice Drop 45	2.66	3.33	3.54	3.64	1.76	1506.65	1465.20	3793.80	
Ice Drop 48	2.99	3.58	4.08	4.23	1.87	1464.66	1412.72	3830.98	

	Outlier Explanation
Ice Drop 9	Crack in Ice
Ice Drop 18	For 0 deg: Drop went from small to large diameter, so drop height is lower than measured
Ice Drop 24	For 0 deg: Drop went from small to large diameter, so drop height is lower than measured
Ice Drop 25	For 0 deg: Drop went from small to large diameter, so drop height is lower than measured
Ice Drop 27	Visible Crack; For 0 deg: Drop went from small to large diameter, so drop height is lower than measured
Ice Drop 29	Visible Crack
Ice Drop 36	For 0 deg: Drop went from small to large diameter, so drop height is lower than measured

Table B.1: Summary of the data subtracted from the compact ice drop experiments. The columns represent: The drop height that was measured from the water, or ice drop; The ToF of the reflected ultrasonic signal from the top surface of the drop for different temperatures; The speed of sound derived from the drop height and ToF; The experiments for which outliers have been identified. The reasoning behind the outlier selection is found in the lower table.

B.2. Porous Ice drop experiments

	Height [mm]		Time of Flight [μs]			Speed of Sound [m/s]		
	Water	Ice	$ToF_{R.T.}$	$ToF_{0°C}$	$ToF_{-18°C}$	$c_{R.T.}$	$c_{0°C}$	$c_{-18°C}$
Ice Drop 15	3.14	3.17	4.54	4.88	2.06	1382.88	1297.81	3074.43
Ice Drop 16	4.18	4.64	6.70	7.95	2.59	1249.24	1167.18	3582.65
Ice Drop 17	4.33	2.64	6.14	-	-	1412.66	-	-
Ice Drop 19	3.58	4.02	-	6.70	-	-	1199.77	-
Ice Drop 21	3.36	3.64	5.23	6.96	-	1285.03	1047.55	-
Ice Drop 22	-	3.31	-	-	-	-	-	-
Ice Drop 23	3.89	4.13	6.65	7.15	2.94	1168.83	1156.18	2811.79
Ice Drop 26	2.26	3.02	-	2.87	1.35	-	1578.99	4484.57
Ice Drop 30	-	5.37	-	7.81	3.37	-	1376.12	3193.90
Ice Drop 31	-	4.44	-	7.22	2.78	-	1230.89	3196.76
Ice Drop 32	-	2.89	-	4.55	1.79	-	1270.90	3230.50
Ice Drop 33	-	5.07	-	8.23	2.90	-	1233.98	3499.82
Ice Drop 34	2.17	3.83	2.82	3.08	2.43	1538.50	1408.63	3161.48
Ice Drop 37	-	1.87	2.93	-	1.37	-	-	2724.19
Ice Drop 38	-	2.42	2.64	4.36	1.37	-	1111.24	3549.45
Ice Drop 39	2.86	3.29	5.42	5.10	1.83	1055.43	1291.99	3606.95
Ice Drop 40	3.55	5.97	5.17	7.66	3.41	1373.31	1558.95	3504.79
Ice Drop 41	1.86	3.28	2.51	4.51	1.78	1482.63	1455.17	3682.90
Ice Drop 42	-	3.89	3.32	5.25	2.15	-	1483.22	3630.25
Ice Drop 43	3.45	4.89	4.96	8.64	2.60	1394.37	1131.60	3765.47
Ice Drop 44	2.40	3.08	3.55	4.57	1.78	1352.11	1347.35	3468.96
Ice Drop 46	2.71	4.12	4.00	6.60	2.25	1358.84	1247.47	3667.41
Ice Drop 47	2.17	3.45	3.06	4.91	2.00	1416.12	1404.31	3447.58

Table B.2: Summary of the data subtracted from the Porous ice drop experiments. The columns represent: The drop height that was measured from the water, or ice drop; The ToF of the reflected ultrasonic signal from the top surface of the drop for different temperatures; The speed of sound derived from the drop height and ToF

B.3. Alternative Ice drop experiments

	Height [mm]		Time of Flight [μs]			Speed of Sound [m/s]		
	Water	Ice	$ToF_{R.T.}$	$ToF_{0°C}$	$ToF_{-18°C}$	$c_{R.T.}$	$c_{0°C}$	$c_{-18°C}$
	Beer (0%)							
Ice Drop 12	2.45	2.17	4.92	5.16	-	995.62	840.61	-
Ice Drop 13	3.41	3.08	7.80	6.12	-	875.40	1007.63	-
	Bubble Water (No bubbles)							
Ice Drop 20	2.89	2.85	3.58	2.78	1.34	1592.18	2050.36	4273.45
	Karmeliet							
Ice Drop 49	2.41	1.69	3.22	2.52	-	1498.56	1346.70	-
Ice Drop 50	1.59	1.36	2.04	1.86	0.85	1560.92	1466.28	3208.56
	Karmeliet (No Bubbles)							
Ice Drop 51	1.23	1.24	1.52	1.54	0.61	1619.34	1615.64	4065.57
	Ethanol (96%)							
Ice Drop 52	1.38	0.00	2.43	-	-	1131.69	-	-

Table B.3: Summary of the data subtracted from the alternative ice drop experiments. Every type of experiment is tagged individually in the table. The columns represent: The drop height that was measured from the water, or ice drop; The ToF of the reflected ultrasonic signal from the top surface of the drop for different temperatures; The speed of sound derived from the drop height and ToF.

	Comments on Experiments
Ice Drop 12	For 0 deg: Drop went from small to large diameter, so drop height is lower than measured
Ice Drop 13	Size of drop changed (decreased) significantly;
Ice Drop 13	Leads to higher speed of sound measurements than actually present.
Ice Drop 20	For RT: Asymmetrical placement of the drop on the transducer could have caused a misreading
Ice Drop 20	in the ultrasound; First reflection might have been from another surface then the top.
Ice Drop 20	For 0 deg: Drop went from small to large diameter, so drop height is lower than measured
Ice Drop 50	Echo signal for ice is present, but it's not clear which one is the signal from the peak.

Table B.4: Comments that arose while performing the experiments on the alternative drops.

C

Vacuumchamber experiments

This appendix entails results from all vacuumchamber experiments performed in the small vacuumchamber.

C.1. 03/07: H_2O Deposition experiment

This experiment was done to test the setup and the acquisition of the data obtained from sensors. In this experiment, only the ultrasonic data could be used.

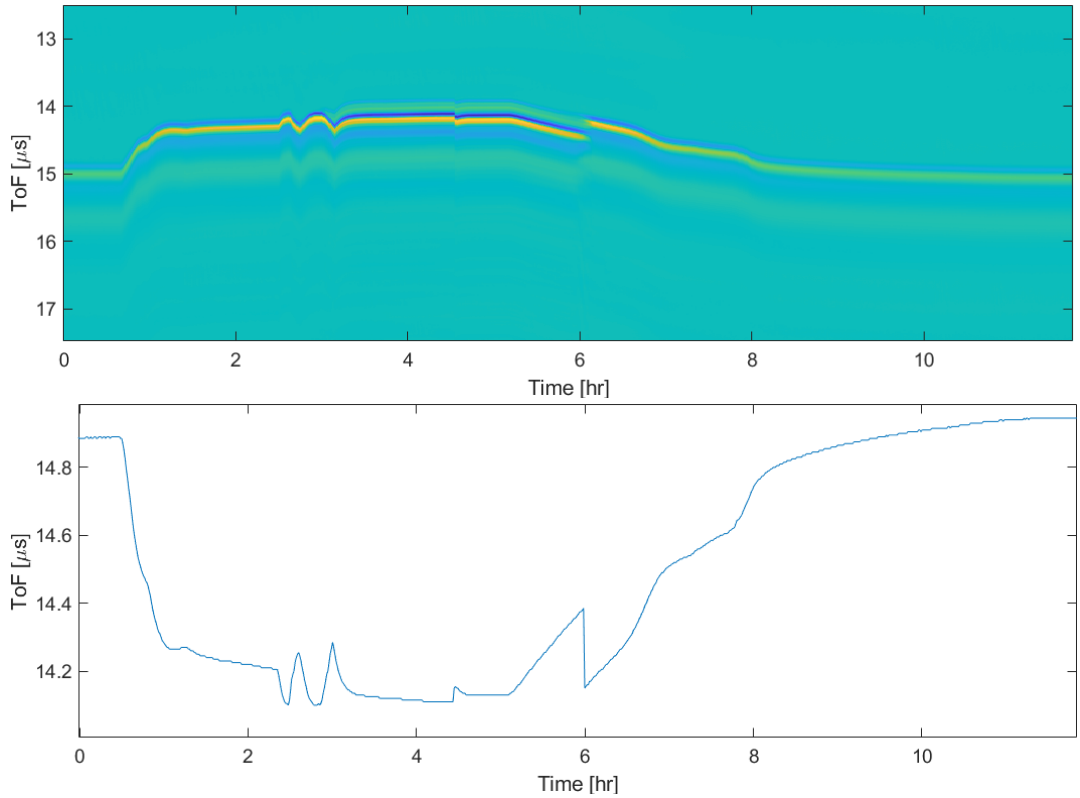


Figure C.1: Useful results of the vacuumchamber experiment on 03/07. Top: Ultrasonic B-scan of the experiment. Bottom: ToF of the peak with the highest intensity.

C.2. 09/07: H_2O Deposition experiment

This experiment aimed to demonstrate ice-deposition with temperature measurements.

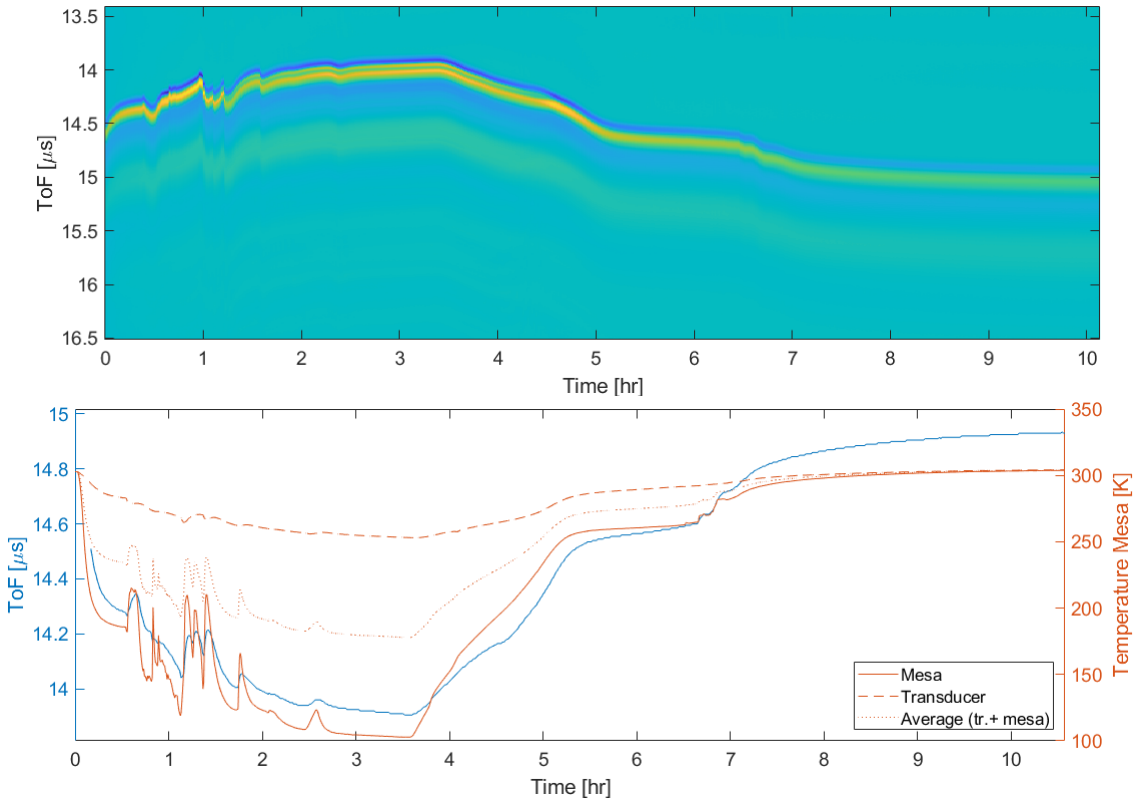


Figure C.2: Useful results of the vacuumchamber experiment on 09/07. Top: Ultrasonic B-scan of the experiment. Bottom: Blue: ToF of the peak with the highest intensity throughout the experiment. Orange: Temperature measured at the "Mesa" on which the ice is deposited and on the methacrylate substrate at the transcucer end. The middle orange line represents the average of them which is considered the average temperature of the methacrylate.

C.3. 15/07: No Deposition experiment

This experiment focuses on the contraction of the methacrylate substrate during an experiment. In this experiment, the measured pressure is saved and plotted in the figure.

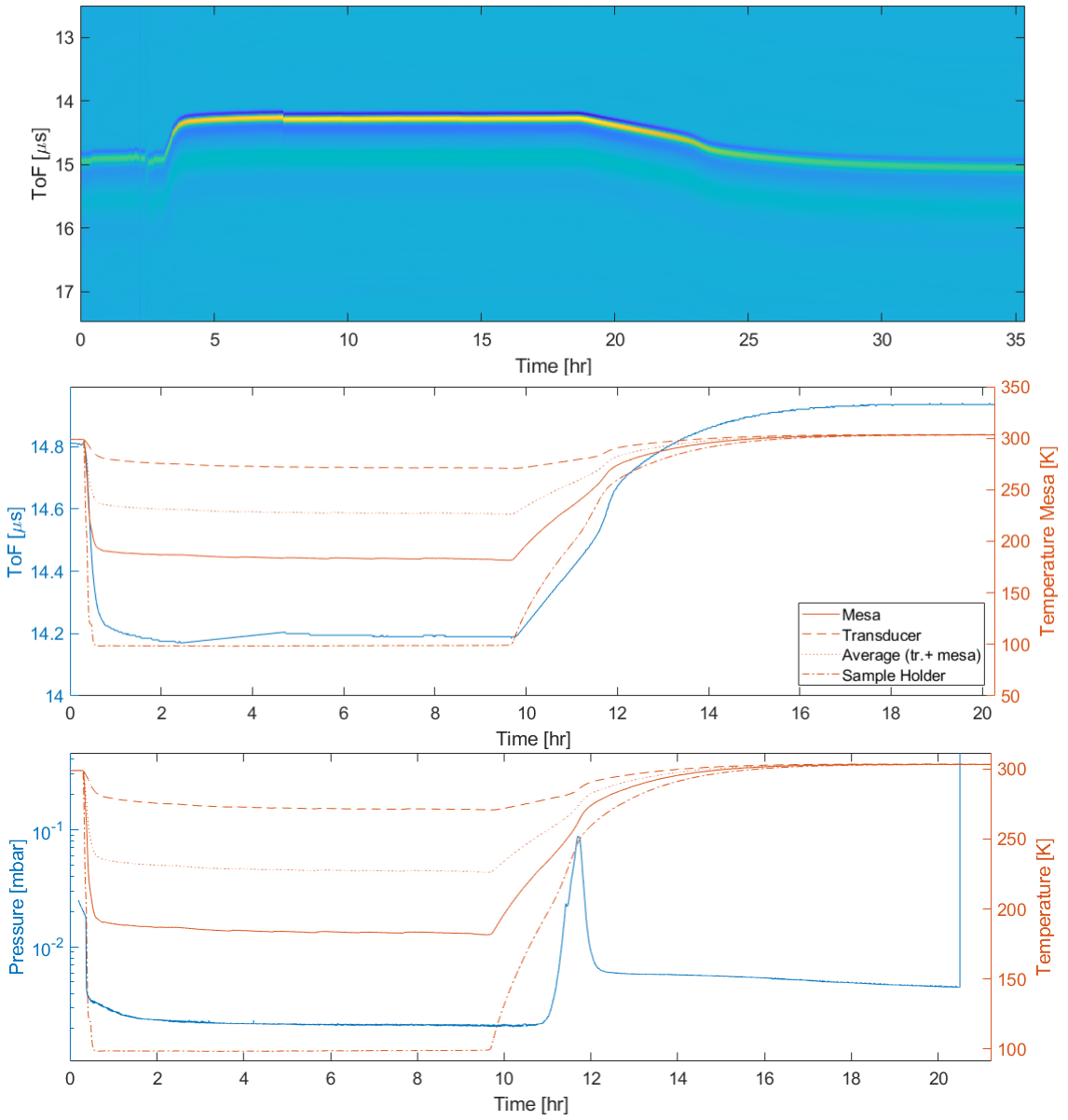


Figure C.3: Useful results of the vacuumchamber experiment on 15/07. Top figure: Ultrasonic B-scan of the experiment. Second figure: Orange: Temperature measured at the "Mesa" on which the ice is deposited and on the methacrylate substrate at the transcucer end. The middle orange line represents the average of them which is considered the average temperature of the methacrylate. The bottom orange line is the measured temperature of the transducer. Blue: ToF of the peak with the highest intensity throughout the experiment. Bottom figure: Blue: Pressure expressed in mbar.

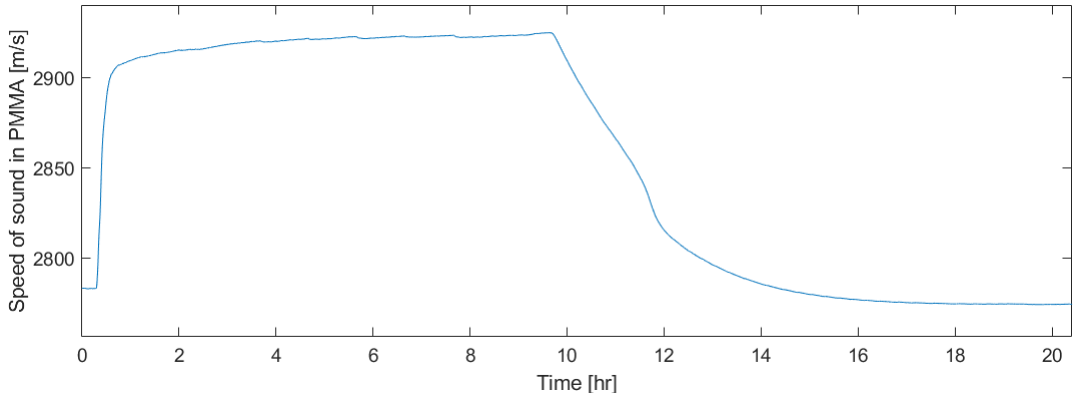


Figure C.4: Calculated speed of sound in methacrylate throughout the experiment from temperature average and literature values.

C.4. 20/07: No Deposition experiment

This experiment focuses on the contraction of the methacrylate substrate during an experiment.

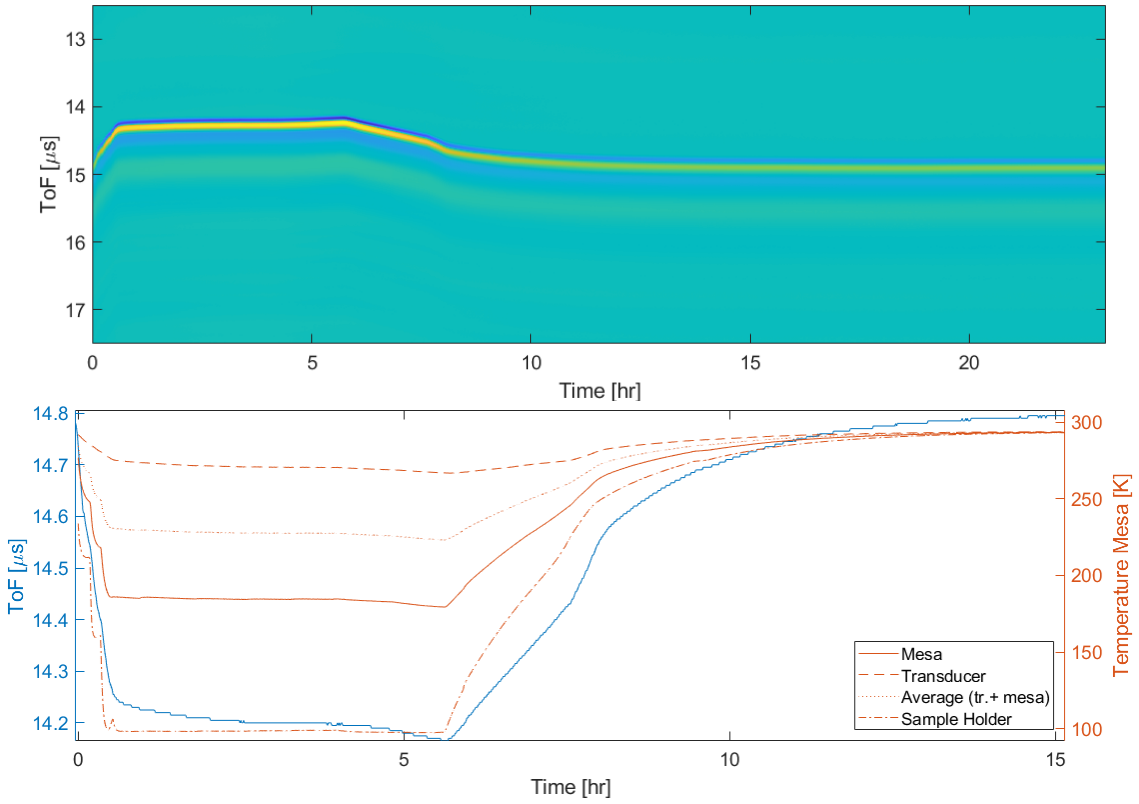


Figure C.5: Useful results of the vacuumchamber experiment on 20/07. Top figure: Ultrasonic B-scan of the experiment. Second figure: Orange: Temperature measured at the "Mesa" on which the ice is deposited and on the methacrylate substrate at the transcucer end. The middle orange line represents the average of them which is considered the average temperature of the methacrylate. The bottom orange line is the measured temperature of the transducer. Blue: ToF of the peak with the highest intensity throughout the experiment. Bottom figure: Blue: Pressure expressed in mbar.

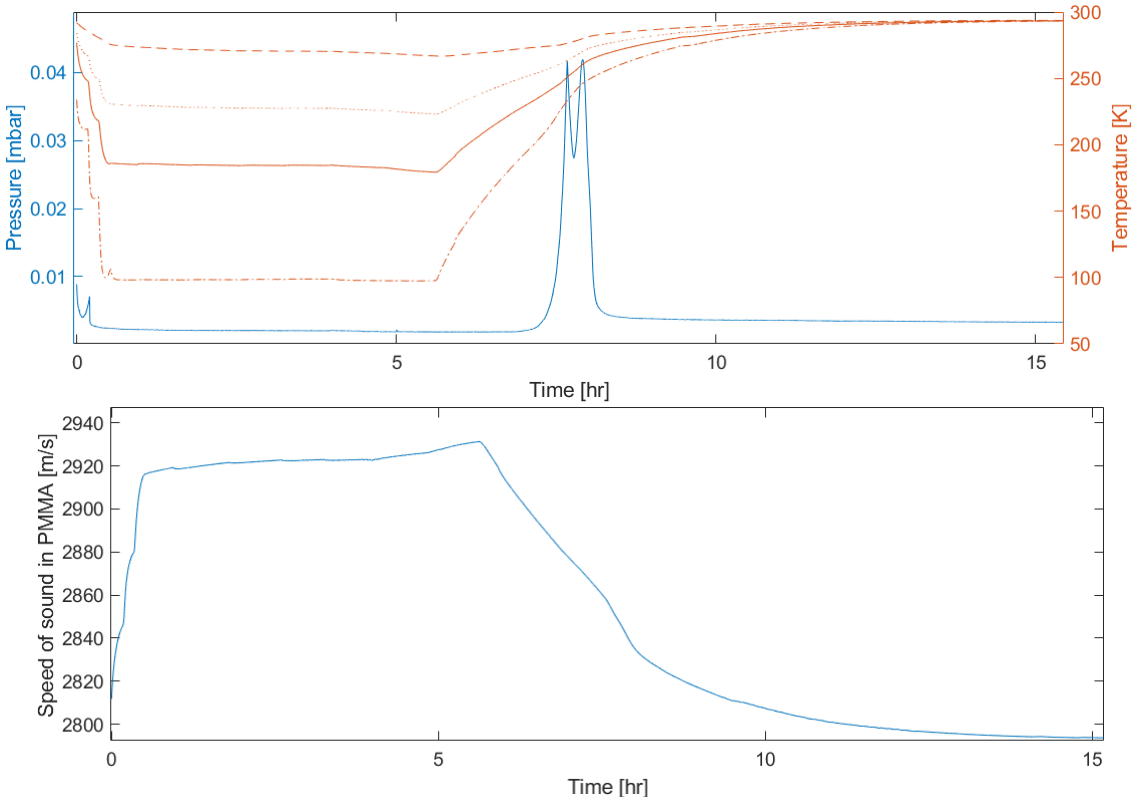


Figure C.6: Top figure: Orange: Temperature measured at the "Mesa" on which the ice is deposited and on the methacrylate substrate at the transcucer end. The middle orange line represents the average of them which is considered the average temperature of the methacrylate. The bottom orange line is the measured temperature of the transducer. Blue: Pressure expressed in mbar. Bottom figure: Calculated speed of sound in methacrylate throughout the experiment from temperature average and literature values.

C.5. 22/07: H_2O Deposition experiment

This experiment had a water deposition of only one deposition tube filled with water. This was done to prove that the methacrylate substrate can reach lower temperatures after depositing water that contributes to the thermal conductivity between the sample holder and the methacrylate "mesa".

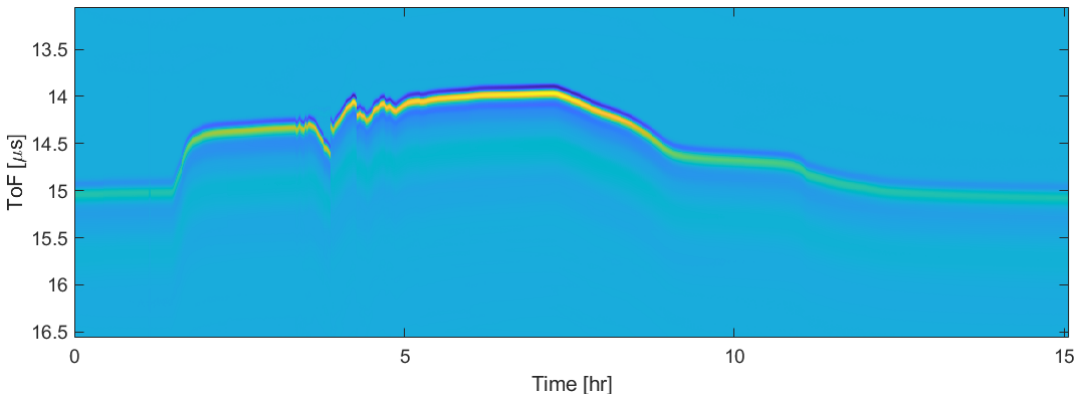


Figure C.7: Ultrasonic B-scan of the experiment on 22/07.

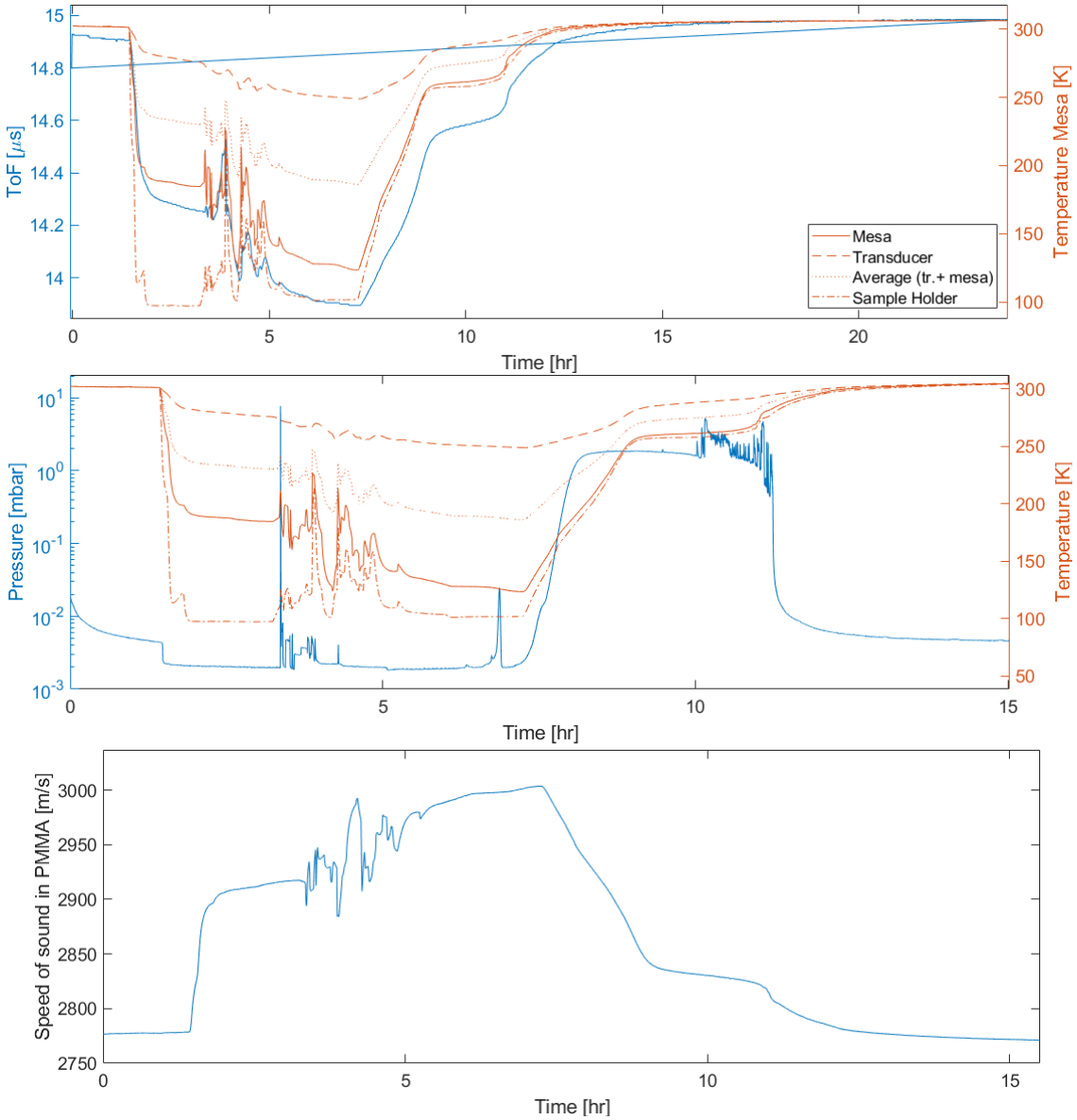


Figure C.8: Useful results of the vacuumchamber experiment on 22/07. Top figure: Orange: Temperature measured at the "Mesa" on which the ice is deposited and on the methacrylate substrate at the transcucer end. The middle orange line represents the average of them which is considered the average temperature of the methacrylate. The bottom orange line is the measured temperature of the transducer. Blue: ToF of the peak with the highest intensity throughout the experiment. Second figure: Blue: Pressure expressed in mbar. Bottom figure: Calculated speed of sound in methacrylate throughout the experiment from temperature average and literature values.

C.6. 24/07: H_2O Deposition experiment

This experiment had several depositions. The aim of the experiment was to create a "thick" enough ice in order for the ultrasonic signature to be distinctive from the peak that resembles the end of the methacrylate.

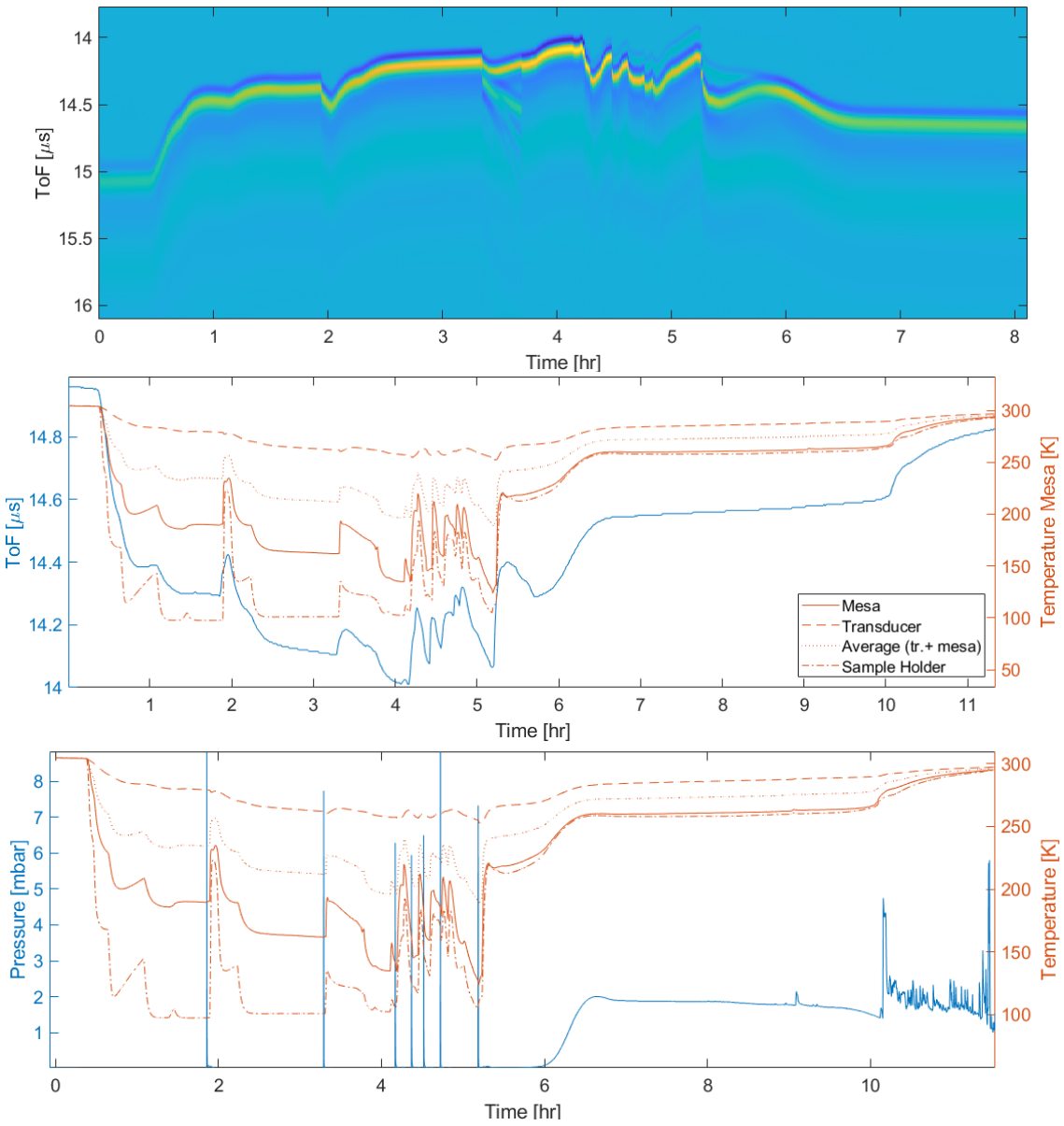


Figure C.9: Useful results of the vacuumchamber experiment on 24/07. Top figure: Ultrasonic B-scan of the experiment. Second figure: Orange: Temperature measured at the "Mesa" on which the ice is deposited and on the methacrylate substrate at the transcucer end. The middle orange line represents the average of them which is considered the average temperature of the methacrylate. The bottom orange line is the measured temperature of the transducer. Blue: ToF of the peak with the highest intensity throughout the experiment. Bottom figure: Blue: Pressure expressed in mbar.

C.7. 28/07: H_2O Deposition experiment

A number of water depositions were done to ensure a thick ice. Measurements from the laser vibrometer are plotted in Figure C.11. The vibrometer measures the relative difference from a reflective object. During the experiments, this signal drifted often. The range of relative displacement was set to $\pm 1mm$. When the signal approaches the boundaries, it was manually reset to zero. After numerous attempts, the laser vibrometer kept on receiving a highly attenuated signal caused by the scattering of the ice grown, which lead to this unwanted drift in its measurements. This is why the use of this laser was eventually discarded.

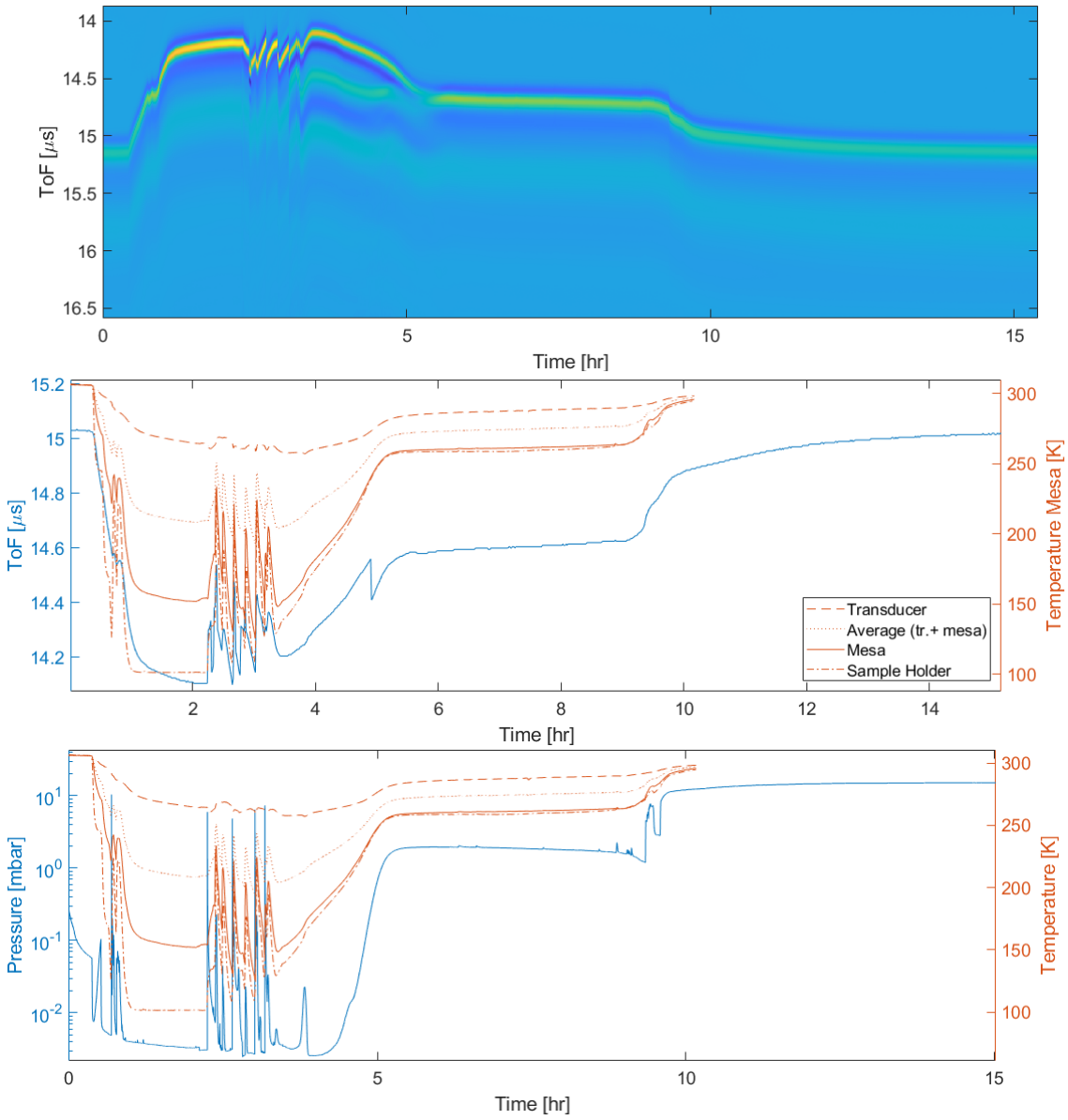


Figure C.10: Useful results of the vacuumchamber experiment on 28/07. Top figure: Ultrasonic B-scan of the experiment. Second figure: Orange: Temperature measured at the "Mesa" on which the ice is deposited and on the methacrylate substrate at the transcucer end. The middle orange line represents the average of them which is considered the average temperature of the methacrylate. The bottom orange line is the measured temperature of the transducer. Blue: ToF of the peak with the highest intensity throughout the experiment. Bottom figure: Blue: Pressure expressed in mbar.

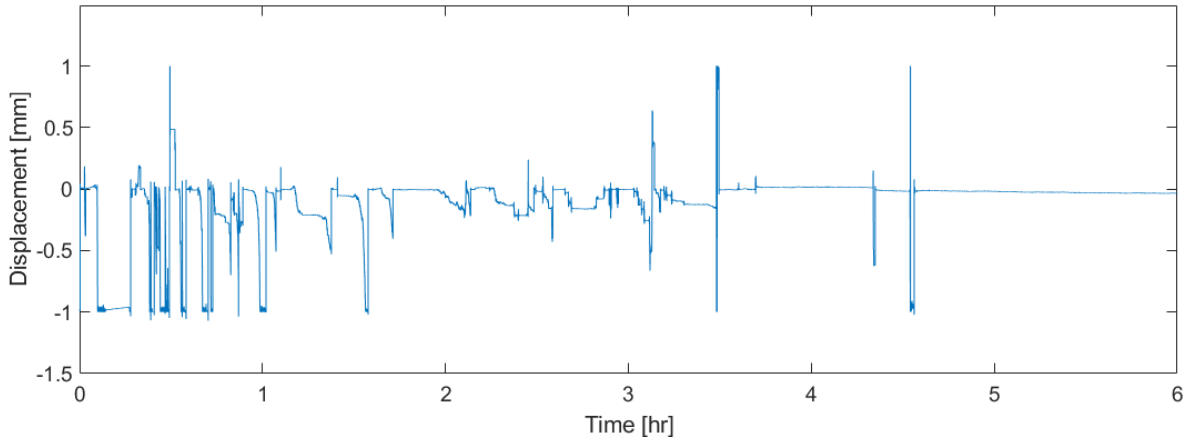


Figure C.11: Relative distance difference as measured from the laser.

C.8. 29/07: CH_3OH Deposition experiment

When the opportunity arose to experiment with different species of astrophysical importance, methanol was used to grow ice. Because the atmospherical conditions in the vacuumchamber are around the triple point of methanol, it allowed for drop to form that evaporate and fill the vacuumchamber with warm vapors that will melt all grown ice. Therefore the methanol deposition experiments have the tendency to initiate a chain reaction after which all grown ice would melt and eventually evaporate out of the vacuumchamber.

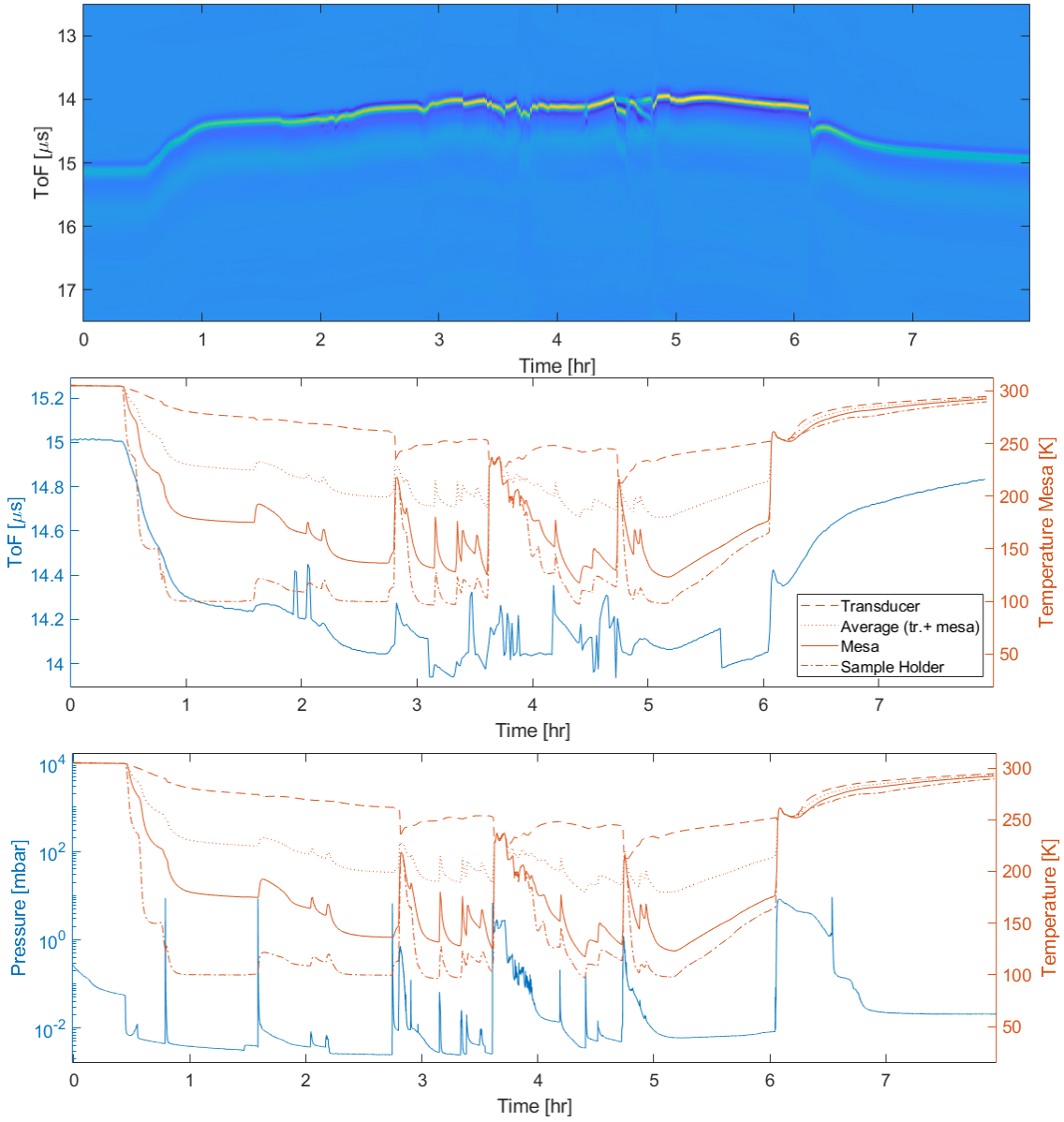


Figure C.12: Useful results of the vacuumchamber experiment on 29/07. Top figure: Ultrasonic B-scan of the experiment. Second figure: Orange: Temperature measured at the "Mesa" on which the ice is deposited and on the methacrylate substrate at the transcucer end. The middle orange line represents the average of them which is considered the average temperature of the methacrylate. The bottom orange line is the measured temperature of the transducer. Blue: ToF of the peak with the highest intensity throughout the experiment. Bottom figure: Blue: Pressure expressed in mbar.

C.9. 30/07: CH_3OH Deposition experiment

A second experiment with methanol showed similar behavior with respect to the chain reaction. Once a drop melts, all ice will melt and will be lost.

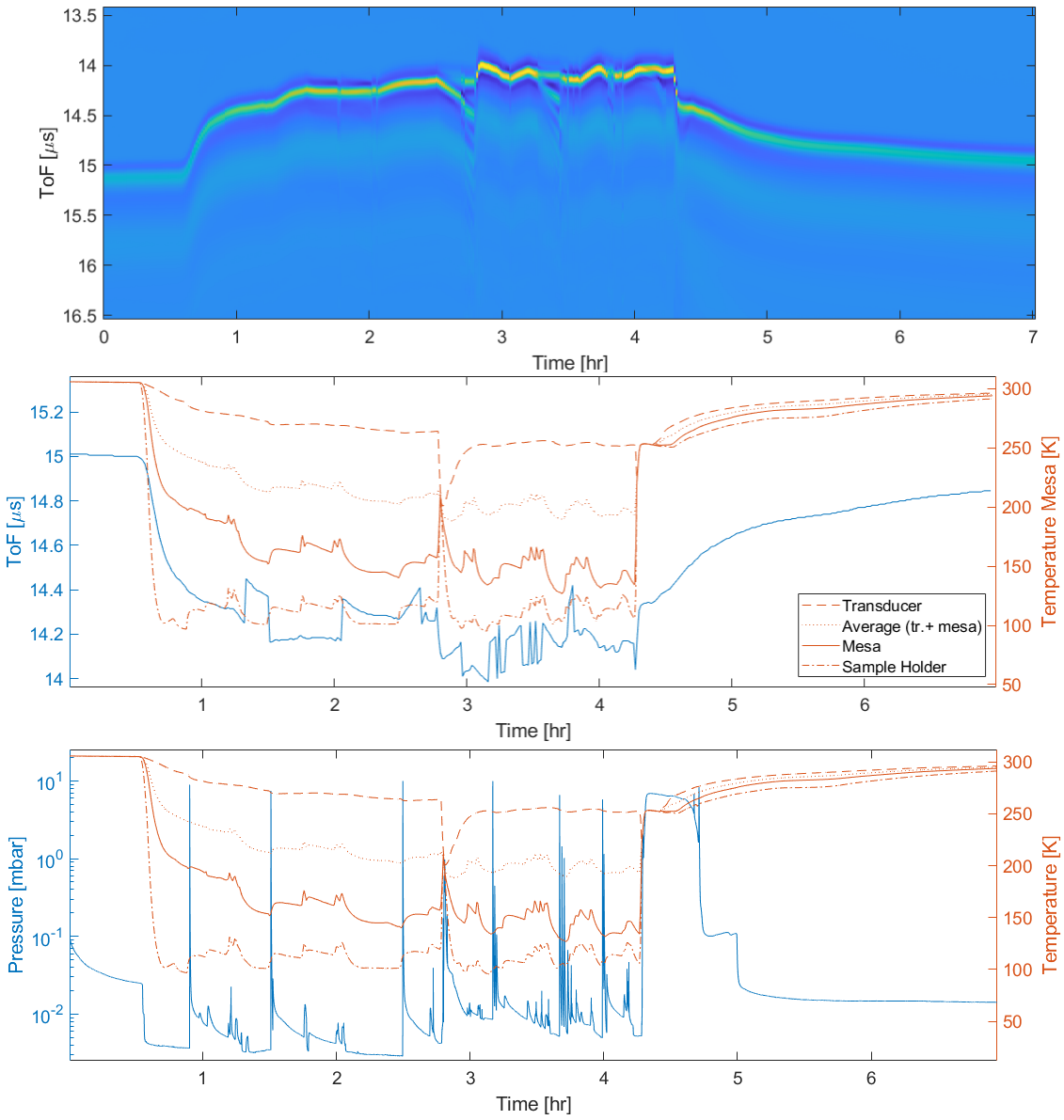


Figure C.13: Useful results of the vacuumchamber experiment on 29/07. Top figure: Ultrasonic B-scan of the experiment. Second figure: Orange: Temperature measured at the "Mesa" on which the ice is deposited and on the methacrylate substrate at the transcucer end. The middle orange line represents the average of them which is considered the average temperature of the methacrylate. The bottom orange line is the measured temperature of the transducer. Blue: ToF of the peak with the highest intensity throughout the experiment. Bottom figure: Blue: Pressure expressed in mbar.